

AD-A259 271



AEOSR-TR- 93 0001

2



Department of AERONAUTICS and ASTRONAUTICS
STANFORD UNIVERSITY

**DAMAGE MECHANICS OF CROSS-PLY LAMINATES
RESULTING FROM TRANSVERSE CONCENTRATED LOADS**

Final Report

for the period from October 1, 1989, to September 30, 1992

AFOSR Contract Number 89-0554

submitted to

Dr. Walter Jones

Director of Mechanics of Materials

Air Force Office of Scientific Research

Bolling, Washington, DC 20331-6448

by

Sheng Liu* and Fu-Kuo Chang†

Department of Aeronautics and Astronautics

Stanford University

Stanford, CA 94305

DTIC
ELECTE
JAN 13 1993
S B D

DISTRIBUTION STATEMENT A
Approved for public release
Distribution Unlimited

*Graduate Student.

†Associate Professor.

93-00717



| REPORT DOCUMENTATION PAGE | | | Form Approved GSA No. 0704-0168 | |
|---|---|--|---|--|
| <small>Public reporting burden for this collection of information is estimated to average 1 hour per response, including the time for reviewing instructions, searching existing data sources, gathering and maintaining the data needed, and completing and reviewing the collection of information. Send comments regarding this burden estimate or any other aspect of this collection of information, including suggestions for reducing this burden, to Washington Headquarters Services, Directorate for Information Operations and Reports, 1215 Jefferson Davis Highway, Suite 1204, Arlington, VA 22202-4302, and to the Office of Management and Budget, Paperwork Reduction Project (0704-0168), Washington, DC 20503.</small> | | | | |
| 1. AGENCY USE ONLY (Leave blank) | | 2. REPORT DATE 9/30/92 | | 3. REPORT TYPE AND DATES COVERED Final Report 10/1/89-9/30/92 |
| 4. TITLE AND SUBTITLE Damage Mechanics of Cross-Ply Laminates Resulting from Transverse Concentrated Loads (u) | | | 5. FUNDING NUMBERS AFOSR 89-0554 | |
| 6. AUTHOR(S) Sheng Liu and Fu-Kuo Chang | | | | |
| 7. PERFORMING ORGANIZATION NAME(S) AND ADDRESS(ES) Stanford University Aeronautics & Astronautics Stanford, CA 94305-4035 | | | 8. PERFORMING ORGANIZATION REPORT NUMBER | |
| 9. SPONSORING / MONITORING AGENCY NAME(S) AND ADDRESS(ES) AFOSR / NA Bldg 410 Bolling, Washington DC 20331-6448 | | | 10. SPONSORING / MONITORING AGENCY REPORT NUMBER | |
| 11. SUPPLEMENTARY NOTES | | | | |
| 12a. DISTRIBUTION / AVAILABILITY STATEMENT Approved for public release; distribution unlimited | | | 12b. DISTRIBUTION CODE | |
| 13. ABSTRACT (Maximum 200 words) An investigation was performed to study damage development in fiber-reinforced laminated composites induced by transverse concentrated loads. The major focus of the study was to understand fundamentally the damage mechanics in terms of matrix cracking and delamination growth, and the interaction between them resulting from a transverse concentrated load. The study was focused on cross-ply laminates only, and the load was introduced quasi-statically through a cylindrical or spherical indenter. Accordingly, the research was divided into two stages: 1) damage induced by a cylindrical indenter and 2) damage induced by a spherical indenter. Analytical models consisting of a contact analysis and a failure analysis were developed for analyzing the damage initiation and growth induced by both loading conditions. Experiments were also performed to generate data needed for the models and to verify the proposed analyses. The predictions based on the models agreed very well with the data. | | | | |
| 14. SUBJECT TERMS Laminated Composites, Delamination Growth, Transverse Concentrated Loading | | | 15. NUMBER OF PAGES 183 | |
| | | | 16. PRICE CODE | |
| 17. SECURITY CLASSIFICATION OF REPORT Unclassified | 18. SECURITY CLASSIFICATION OF THIS PAGE Unclassified | 19. SECURITY CLASSIFICATION OF ABSTRACT Unclassified | 20. LIMITATION OF ABSTRACT UL | |

Table of Contents

| | |
|---|-----------|
| Abstract | i |
| Table of Contents | ii |
| 1 Introduction | 1 |
| 2 Method of Approach | 6 |
| 2.1 The Objectives | 6 |
| 2.2 The Major Tasks | 8 |
| 2.2.1 Damage Induced by a Cylindrical Indenter | 8 |
| 2.2.2 Damage Induced by a Spherical Indenter | 8 |
| 3 Damage Induced by a Cylindrical Indenter | 10 |
| 3.1 Statement of Problem | 10 |
| 3.2 Analysis | 11 |
| 3.2.1 Stress Analysis | 12 |
| 3.2.2 Contact Analysis | 13 |
| 3.2.3 Failure Analysis | 19 |
| 3.3 Finite Element Modeling | 21 |
| 3.3.1 Variational Formulation of the Discrete Problem | 24 |
| 3.3.2 Finite Element Modeling of Failure | 27 |
| 3.4 Verification | 29 |
| 3.4.1 Comparison with Existing Results | 29 |
| 3.4.2 Comparison with Current Test Data | 40 |
| 3.5 Discussion | 52 |
| 3.6 Concluding Remarks | 58 |

DTIC QUALITY INSPECTED 8

| | |
|--------------------|----------------------|
| Distribution/ | |
| Availability Codes | |
| Dist | Avail and/or Special |
| A-1 | |

| | |
|---|-----------|
| 4 Damage Induced by a Spherical Indenter | 60 |
| 4.1 Statement of Problem | 60 |
| 4.2 Analysis | 62 |
| 4.2.1 Contact Analysis | 62 |
| 4.2.2 Failure Analysis | 67 |
| 4.3 Finite Element Implementation of the Formulation | 68 |
| 4.3.1 Variational Formulation of the Discrete Problem | 69 |
| 4.3.2 Mesh Generation | 72 |
| 4.3.3 Contact Node Search | 78 |
| 4.3.4 Numerical Implementation of the Failure Model | 81 |
| 4.4 Verification with Existing Data | 84 |
| 4.5 Results and Comparison | 92 |
| 4.6 Concluding Remarks | 124 |

Appendices

| | |
|---|------------|
| A A 2-D Finite Element Mesh Remodeling Procedure | 125 |
| B Contact Residual and Stiffness of a 2-D Contact Element | 129 |
| C Symmetry Treatment and Contact Node Search Strategy ... | 135 |
| D Contact Residual and Stiffness of a 3-D Contact Element | 146 |
| E Input Data Files for Computer Codes | 155 |
| References | 172 |

Chapter 1

Introduction

It is well known that fiber-reinforced composites are vulnerable to transverse concentrated loads such as low-velocity impact, which can result in extensive delaminations and multiple matrix cracking [1-34]. Such internal damage can cause significant reduction of the load carrying capacity of structures made of composites.

Because of the significance of the problem, numerous experimental and analytical investigations have been performed to study the damage resulting from transverse loads. The analytical work previously developed has emphasized estimating the overall delamination sizes. Wu and Springer [4, 16] proposed a non-dimensional empirical expression which requires several parameters to be determined from appropriate experiments. Gu and Sun [21] developed a model for estimating the impact damage size in sheet molding compound (SMC) composites. The applicability of their model to long fiber reinforced laminates is questionable. Choi and Chang [8, 32] proposed a semi-empirical model based on failure mechanisms for predicting the delamination size and locations due to low-velocity impact. Although the model provides reasonable estimates of the damage size, the mechanics of damage growth and the material behavior during impact cannot be obtained from the model. Finn and Springer [2] developed an energy criterion for predicting delamination sizes

and locations for laminates due to both low-velocity and quasi-static loading. The model needs a quantity which was correlated to the energy per unit area required to delaminate an interface. None of the above mentioned models considered the detailed fracturing process during the formation of the damage.

Several investigators have indicated based on their experiments that for some ply orientations, surface matrix cracking could be produced without generating delaminations by carefully adjusting the impact velocity or the amount of the applied load. However, whenever there was a delamination, there were matrix cracks accompanied with the delamination. In other words, matrix cracking and delamination were detected co-existing in most test conditions. An energy threshold also exists below which no damage could be generated. Experiments have demonstrated that similar results obtained from low-velocity impact tests could be produced by quasi-static transverse loads [1, 3, 7, 9].

Jones, Joshi and Sun [6, 7, 27] have suggested that matrix cracking is the initial impact damage mode. Recently, Choi *et al.* [8, 32, 33, 34] investigated impact damage using a cylindrical indenter. Because the indenter produced a line load during impact, it simplified the impact damage pattern from three dimensions to two dimensions. As a result, the damage modes could be detected from the side of the specimens by the naked eye without cutting the specimens. Their study showed that the impact energy (velocity) threshold (the minimum energy required to cause damage) is associated with the energy required to initiate matrix cracks. It was concluded that matrix cracking is the initial impact damage mode and delaminations are generated from the matrix cracks.

Basically, the initial matrix cracks have been classified by several investigators [7, 8] into two types: the shear crack and bending crack. The former appears inside the laminate and is located a distance from the impacting area, but the

latter occurs directly beneath the transverse load in the outermost layers of the laminate. Previous studies [8, 32, 33, 34] have shown that the extent of delamination strongly depends upon the location of the initial matrix cracks. Choi *et al.* showed experimentally from their line-loading impact study that the shear crack-induced damage is violent and catastrophic, but bending crack-induced damage is quite progressive. It is apparent that there is a strong interaction between matrix cracking and delamination growth in laminated composites resulting from transverse loads [1-8]. In contrast, this strong interaction does not appear for the panel due to in-plane loads.

In the past, matrix cracking and delamination have been frequently treated in the literature as two separable damage modes, where the former occurred at an early stage of loading and was related to the initial stage of failure, while the latter was associated with the final stage of failure of composites. However, in transverse loading, matrix cracking once developed seems to affect delamination significantly. This phenomenon seems to set apart the major difference in damage growth mechanisms between transverse concentrated loadings and in-plane loadings. It is therefore believed that this interaction must be thoroughly studied in order to fundamentally understand the damage mechanics. Knowledge of the damage mechanics is critically important to material scientists for improving impact resistance of composites and to design engineers for selecting and designing adequate composite structures which may be subjected to transverse loads.

Limited work has been performed in studying the damage mechanics and the interaction between matrix cracking and delamination [38, 39, 46, 47, 48]. The models of Bostaph and Elber [38] and Grady *et al.* [39] provide an estimate of the delamination growth, but require *a priori* knowledge of the number and locations of delaminations. Another assumption in Bostaph and Elber's model is that all

delaminations grow to the same size. Grady's model applies only to relatively large delaminations. However, matrix cracking was not considered in their research. The fracture modes controlling delamination growth of laminated composites subjected to transverse concentrated loads have not yet been adequately identified. Furthermore, the fracture modes contributing to the delamination propagation could be different with or without taking into account the effect of matrix cracking. Identifying these fracture modes will be important for designing composite material and structural systems which are more damage resistant to transverse loads. Sun *et al.* [46] performed a 2-D linear study of initiation of delamination growth induced by a surface bending crack for a cross-ply laminate. They found that Mode I dominates the initiation of delamination growth. The very recent models of Martin *et al.* [47] and Salpekar [48] studied the effect of shear crack on the delamination for a curved panel and a flat panel respectively by fracture mechanics. Their 2-D models were based on a linear analysis and only initiation of the delamination growth was considered. Their research may be thought to be parallel to the 2-D model of this thesis research effort [49–51]. Recently, Liu [55] modeled an embedded circular delamination by a thin soft isotropic layer with a linear finite element method and showed that Mode II and Mode III fractures predominantly control the growth of the embedded delamination due to a point load. No matrix cracking was considered in the analysis.

Accordingly, the objective of this investigation was to study the damage mechanics of laminated composites subjected to transverse concentrated loading and to fundamentally understand the interaction between matrix cracking and delamination growth. Both flat and cylindrical composites were considered. To simplify the problem, only cross-ply laminated composite panels were studied, and the load was applied quasi-statically.

In Chapter 2, the major approach for achieving the objectives of the investigation is briefly outlined. Chapter 3 describes a 2-D simplified study both analytically and experimentally. Simplified damage patterns are presented and damage initiation and growth is discussed. An analytical model, consisting of a stress analysis, a failure analysis, and a contact analysis, is presented in detail and verified both analytically and experimentally. The interaction between matrix cracking and delamination is discussed. In Chapter 4, a 3-D model is presented to study the effect of initial matrix cracks on the propagation of delamination due to a spherical indenter loading. The model also consists of a stress analysis, a contact analysis, and a failure analysis. The contact between the indenter and the plate, as well as between the delaminated interfaces is modelled. The model is verified extensively by comparing the predictions with existing data and experimental data. Numerical examples are also presented for a toughened composite system and moderately thick composites. The modes contributing to the delamination propagation are identified and discussed. The interfaces for the 2-D and 3-D computer codes are presented in Appendices D and E.

Chapter 2

Method of Approach

§2.1 The Objectives

This research was performed to investigate damage development in fiber-reinforced laminated composites induced by a quasi-static transverse concentrated load, as shown in Figure 2.1. The major objectives of the research were as follows:

1. to study damage mechanisms and mechanics of fiber-reinforced laminated composites due to quasi-impact loading;
2. to develop adequate models for predicting quasi-impact damage in the materials;
3. to study the interaction between matrix cracking and delamination growth.

In order to achieve these objectives, this research was carried out in two sequential studies as follows:

1. Damage induced by a cylindrical indenter.
2. Damage induced by a spherical indenter.

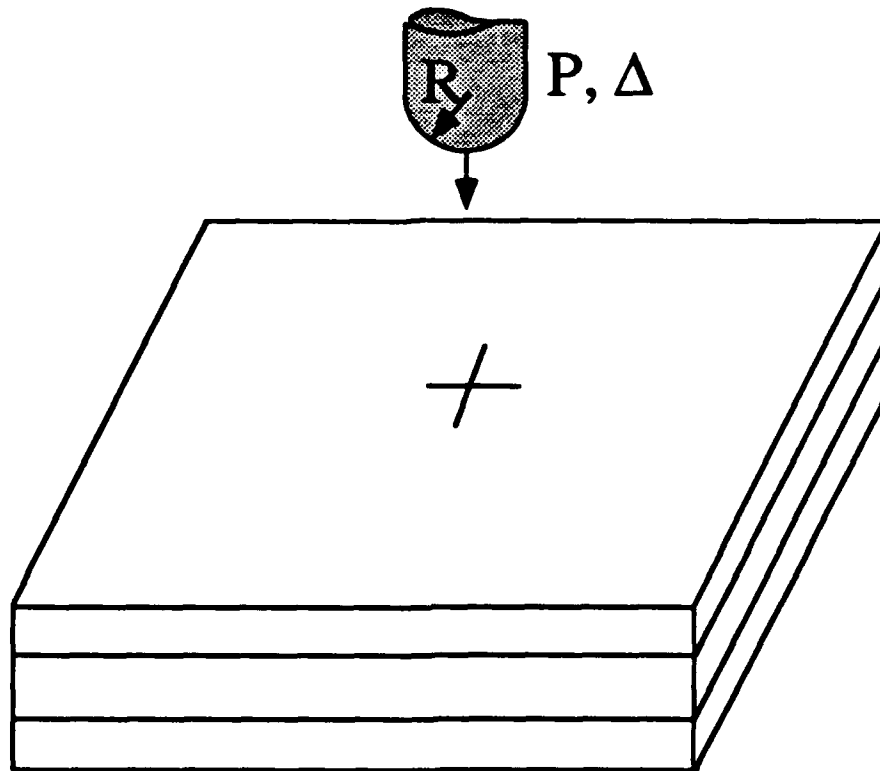


Figure 2.1 Description of the problem. A laminated composite panel subjected to a transverse load applied by a spherically-nosed indenter.

§2.2 The Major Tasks

2.2.1 Damage Induced by a Cylindrical Indenter

A 2-D analytical model was developed for predicting damage in laminated composites resulting from a quasi-static line load applied by a cylindrical indenter. Stresses and strains in composites were calculated from a nonlinear finite element code based on generalized plane strain conditions. A contact model was implemented for the cracked/delaminated systems to handle contact conditions of cracked interfaces. A modified Hashin matrix failure criterion and delamination criterion were used to predict the initial damage. A linear fracture mechanics criterion was adopted for predicting the damage propagation. Extensive comparison between the predictions and experiments was made during the research. This research was expected to be able to characterize the basic failure modes and mechanisms of laminated composites resulting from transverse concentrated loading in two dimensions. The focus was on the type of initial damage mode and how it affected the damage growth. The stable and unstable damage growth resulting from transverse loading depending on the location of the initial damage were emphasized.

2.2.2 Damage Induced by a Spherical Indenter

A 3-D analytical model was also developed for predicting damage in laminated composites resulting from a quasi-static concentrated load applied by a spherical indenter. The focus was on the effect of initial matrix cracking on the delamination propagation. The model consisted of a stress analysis for determining the stress distribution inside the material during the loading, a contact analysis for modeling the contact between the indenter and the laminate as well as contact between the cracked interfaces, and a failure analysis for predicting the direction and extent of

delamination propagation. In the stress analysis, finite deformation was considered and a three-dimensional nonlinear finite element was used to provide stress and strain information. In the contact analysis, a general contact model was proposed based on an augmented Lagrangian method for modeling the indenter-plate contact and cracked interfaces contact, respectively. Comparisons were also made between the experiments and predictions during the investigation.

Chapter 3

Damage Induced by a Cylindrical Indenter

§3.1 Statement of Problem

In this problem, a flat or cylindrical panel made of fiber-reinforced laminated composites which is clamped along two parallel edges and free of support along the others was considered. A transverse concentrated line load was then applied at the center line of the plate parallel to the two clamped edges, as shown in Figure 3.1. The laminate could be either $[0_m/90_n]_s$ or $[90_m/0_n]_s$ layup, where m and n can be arbitrary integers. It was desired to obtain the following:

1. the failure and the response of the structure to the applied load;
2. the initiation of matrix cracking and the corresponding magnitude of the load;
3. delamination initiation and propagation;
4. extent of delamination as a function of the applied load.

§3.2 Analysis

The analytical model proposed for describing the behavior of laminated composite panels with both matrix cracks and delaminations consists of three parts: a stress analysis, a contact analysis, and a failure analysis. The stress analysis was

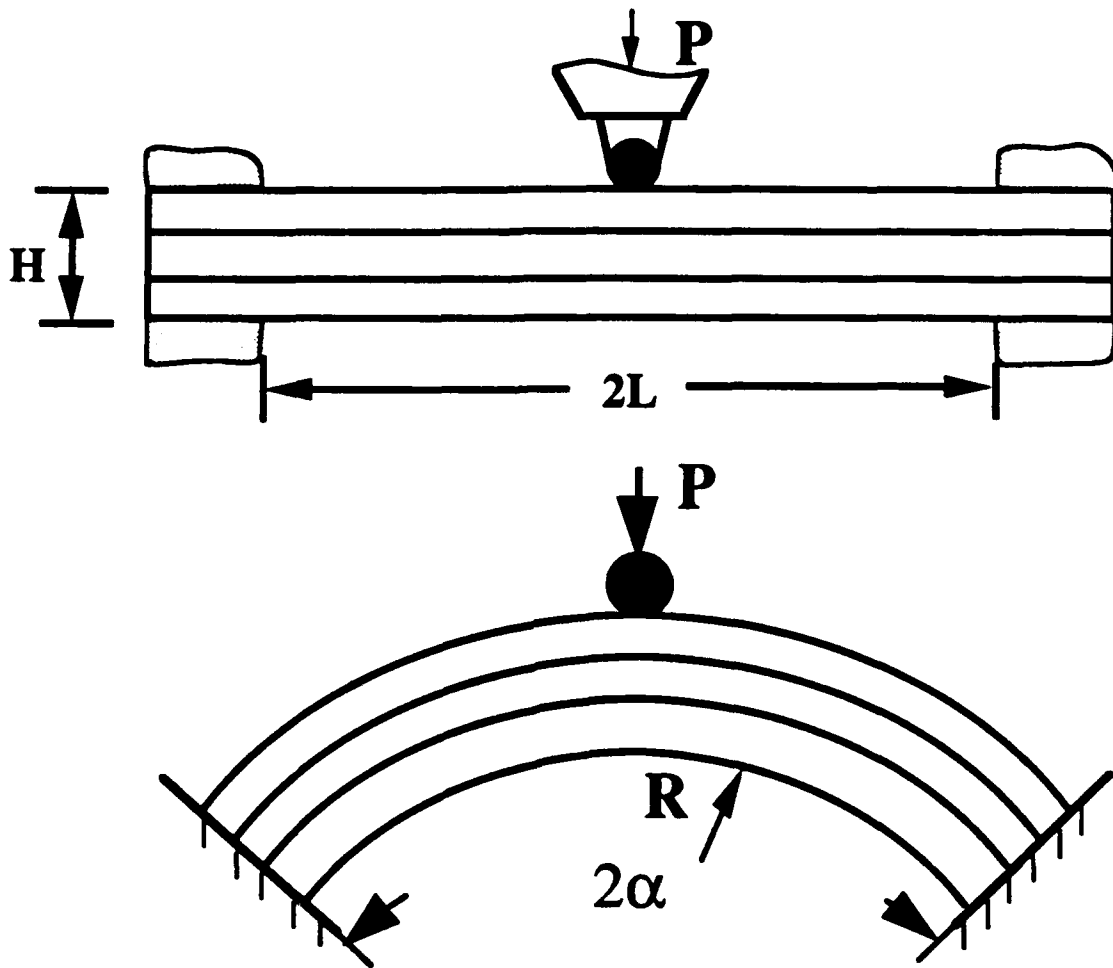


Figure 3.1 Description of the problem: a laminated composite panel (above: flat and below: curved) subjected to a transverse concentrated line load uniform through the width.

developed based on the large deformation theory for analyzing the global and local deformations of the sublaminates. The contact analysis used the Lagrange multiplier method for modeling the matrix crack and delamination interface condition during loading. The failure analysis was proposed for predicting the occurrence of matrix cracking and for modeling delamination initiation and propagation.

3.2.1 Stress Analysis

As the local deformations of the laminate could be substantial due to the concentrated load, finite deformation theory [70-74] was adopted in the analysis. The total potential energy of a laminate without damage under the given load can be described as

$$\Pi = \sum_{m=1}^{n_{ply}} \int_{\Omega^m} W^m(E_{ij}^m) {}^0d\Omega - \int_{\partial S} {}^0\bar{T}_i \cdot u_i {}^0ds \quad (3.1)$$

where n_{ply} is the total number of layers, Ω^m is the cross-sectional area of the m th layer in the reference configuration, and ∂S is the boundary in the reference configuration where the tractions ${}^0\bar{T}_i$ are applied.

The components of the second Piola-Kirchhoff stress in the m th layer can be expressed by the constitutive relation as

$$S_{ij}^m = C_{ijkl}^m E_{kl}^m \quad (3.2)$$

where E_{kl}^m are the components of Green's strain tensor. C_{ijkl}^m are the orthotropic material moduli for the m th layer.

Based on the virtual work principle, the following equation can be obtained from Eq. (3.1) for an uncracked laminate:

$$\delta\Pi = \sum_{m=1}^{n_{ply}} \int_{\Omega^m} S_{ij}^m \delta E_{ij}^m {}^0d\Omega - \int_{\partial S} {}^0\bar{T}_i \cdot \delta u_i {}^0ds = 0 \quad (3.3)$$

The above equation is valid for any uncracked laminated composite undergoing finite deformations in both two and three dimensions.

In the following, the formulation is given for a laminated composite subjected to a line load. It was assumed that the width of the laminate was considerably greater than its thickness, hence the problem was analyzed two-dimensionally. A two-dimensional generalized plane strain condition in the $x_1 - x_3$ plane was adopted. Therefore, as a first approximation, the displacement field of the laminate was assumed in the form [40-42]:

$$\begin{aligned} u_1 &= u_1(x_1, x_3) \\ u_2 &= \alpha x_2 \\ u_3 &= u_3(x_1, x_3) \end{aligned} \tag{3.4}$$

where α is a constant, and u_1, u_2, u_3 are the displacements in the $x_1 - x_2 - x_3$ coordinates, respectively. Consequently, the strain E_{22} is constant, but need not be zero. However, the free edge effect on the response of the panel is neglected.

Substituting the above displacement field of the laminate into Eq. (3.3) provides a nonlinear equilibrium equation for any uncracked laminate subjected to a line load. However, for cracked laminates, Eq. (3.3) cannot be applied directly because of the presence of crack interfaces generated inside the materials. The contact condition of the interfacial contact during loading must be included in the analysis.

3.2.2 Contact Analysis

When a laminated composite is subject to transverse concentrated loading, the presence of matrix cracks and delaminations in the laminate requires that the condition of matrix and delamination surfaces during deformation be specified in the analysis. Because of material mismatch, relative sliding could occur along the interface at which neighboring plies have different ply orientation. A rigorous contact

treatment was essential for accurate modeling of the interface contact conditions.

In order to prevent the contact surfaces from overlapping, an impenetrability condition must be specified and satisfied at all times along the contact interfaces. This condition requires that the shortest distance (defined as a gap g) between two contact surfaces must be greater than or equal to zero. Mathematically, the impenetrability constraint can be stated as $g \geq 0$. Upon contact, the contact force must also be less than or equal to zero ($\lambda_N \leq 0$). Accordingly, the contact constraints for normal contact can be specified as

$$\left. \begin{array}{l} \lambda_N \leq 0 \\ g(u_i) \geq 0 \\ \lambda_N g(u_i) = 0 \end{array} \right\} \quad (3.5)$$

This is the well-known Kuhn-Tucker conditions for normal contact. The three equations in Eq. (3.5) reflect, respectively, the compressive normal traction constraint, the impenetrability constraint, and the requirement that the pressure is nonzero only when $g = 0$.

Accordingly, Eq. (3.5) must be considered together with Eq. (3.3) in order to analyze composites containing internal cracks and delaminations. Several methods exist for implementing the contact constraints [62-63]. One of the most popular choices is the Lagrange multiplier method [63]. The Lagrange multiplier method enforces the exact constraints, and it was adopted in the present two-dimensional study.

By imposing the constraint conditions into the total potential energy using the Lagrange multiplier technique, the total potential energy given in Eq. (3.1) can be modified as

$$\bar{\Pi}(u_i, \lambda_N) = \sum_{m=1}^{n_{plg}} \int_{\Omega^m} W^m(E_{ij}) d\Omega - \int_S {}^o\bar{T}_i \cdot u_i dS + \int_{\Gamma} \lambda_N g(u_i) d\Gamma \quad (3.6)$$

where λ_N is the Lagrange multiplier and Γ is the sum of matrix crack and delaminated surfaces in contact.

The variational equations, corresponding to the Lagrange multiplier formulation, result in

$$\left. \begin{aligned} \sum_{m=1}^{n_{pt}} \int_{\Omega^m} S_{ij}^m \delta E_{ij}^m d\Omega - \int_S {}^o\bar{T}_i \cdot \delta u_i ds + \int_{\Gamma} \lambda_N \delta g d\Gamma = 0, \\ \int_{\Gamma} \delta \lambda_N g d\Gamma = 0 \end{aligned} \right\} \quad (3.7)$$

Or in a more concise form, the above equations may be rewritten as

$$\left. \begin{aligned} \delta \Pi + \int_{\Gamma} \lambda_N \delta g d\Gamma = 0, \\ \int_{\Gamma} \delta \lambda_N g d\Gamma = 0 \end{aligned} \right\} \quad (3.8)$$

where $\delta \Pi$ is the virtual work for an unconstrained system, and $\delta \lambda_N$ and δg are the variation of λ_N and g , respectively.

In order to solve the above equations, the gap function g needs to be defined specifically for any contact interface. For the purpose of generalization, any one of the contact bodies can be defined as “contactor” and the other can be referred to as “target”. Any points belonging to the contact region of the contactor will be called “slave points” and those on the surface of the target will be referred to as “master points”. In the following, m and s indicate points on the master surface and the slave surface, respectively.

Therefore, for a given pair of potential contact points along the contact surfaces, \mathbf{x}_s on the contactor's surface and \mathbf{x}_c on the target's surface, the gap function is defined as

$$|g(u_i)| = \|\mathbf{x}_s - \mathbf{x}_c\| = \min \|\mathbf{x}_s - \mathbf{x}_m\| \quad (3.9)$$

where \mathbf{x}_m can be any point on the target surface. Expressed in words, \mathbf{x}_c (contact

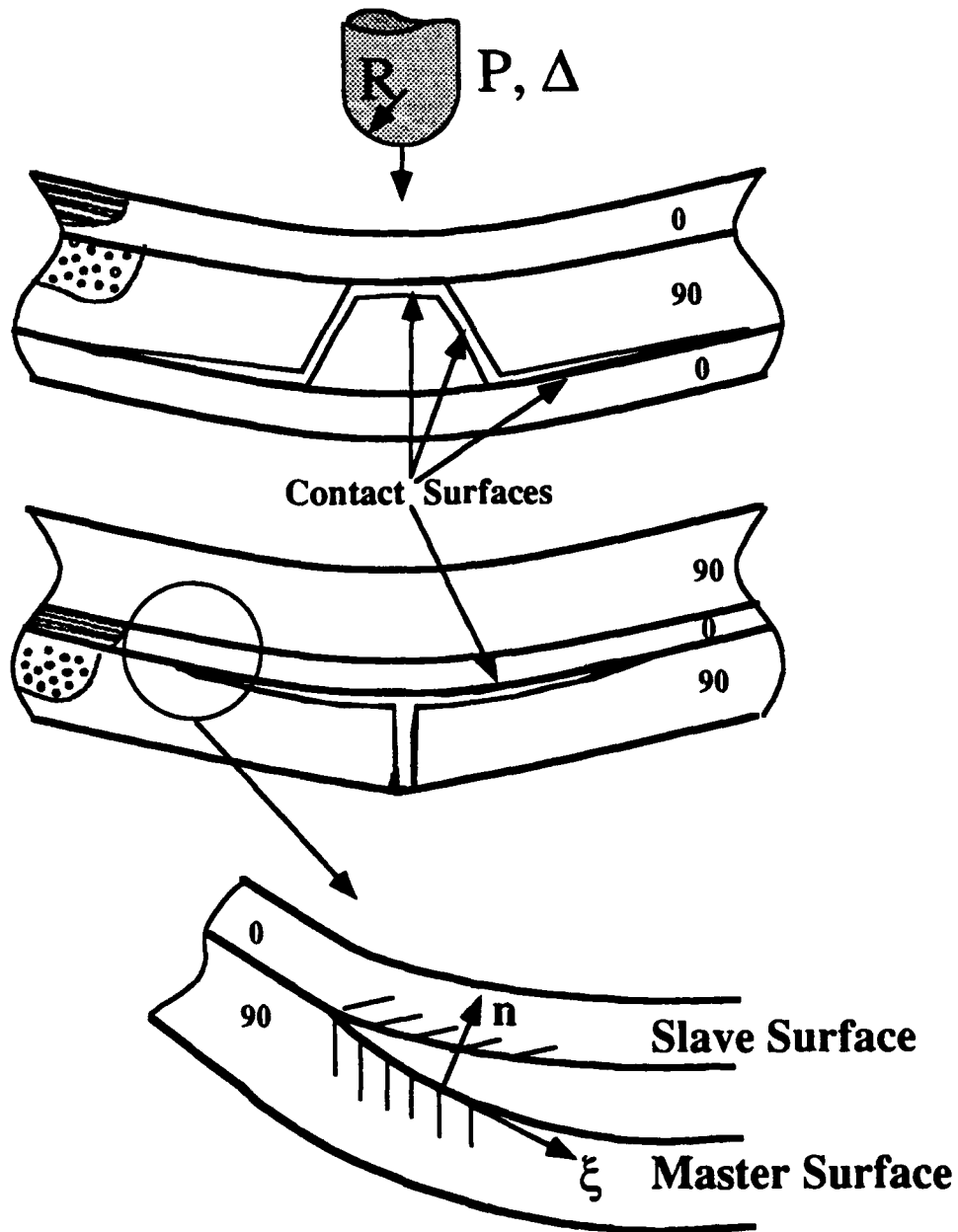


Figure 3.2 Local coordinate systems of contact surfaces in the two-dimensional study.

point) is the closest point projection of \mathbf{x}_s onto the target surface, as shown in Figure 3.3.

It is necessary to give an accurate description of the local geometry on the contact surfaces during the deformation. Here, a local coordinate system needs to be defined such that it is suitable for a definition of the contact constraints. This local coordinate system is fixed along the target surface, as shown in Figure 3.3. Before the local coordinate system can be established, it is necessary to parametrize the contact surface locally. In terms of local surface parameters ξ , the following basis for any master point on the target surface is defined:

$$\left. \begin{aligned} \mathbf{e}_1(\xi) &= \frac{\partial \mathbf{x}_m(\xi)}{\partial \xi} \quad (\text{or } \mathbf{x}_{m,\xi}(\xi)) \\ \mathbf{e}_2(\xi) &= (0, 1, 0)^T \text{ or } (0, -1, 0)^T \\ \mathbf{e}_3(\xi) &= \mathbf{n}(\xi) = \frac{\mathbf{e}_1(\xi) \times \mathbf{e}_2(\xi)}{\|\mathbf{e}_1(\xi) \times \mathbf{e}_2(\xi)\|} \end{aligned} \right\} \quad (3.10)$$

where \mathbf{e}_1 , \mathbf{e}_2 , and \mathbf{e}_3 are vectors in 3-D Cartesian space. The sign of \mathbf{e}_2 depends on the definition of the target surface such that the normal \mathbf{n} is outward on the target surface (Figure 3.3).

Accordingly, the gap function g can be written as

$$g = \mathbf{n} \cdot \mathbf{d} = \mathbf{n} \cdot (\mathbf{x}_s - \mathbf{x}_c) \quad (3.11)$$

This definition is true for both 3-D and 2-D contact gap definition. In terms of local coordinate system the gap g can be written as follows:

$$g = (\mathbf{x}_s - \mathbf{x}_c) \cdot \mathbf{n}(\xi_c) \quad (3.12)$$

In order to solve Eq. (3.8), a nonlinear finite element method was developed. The numerical formulation will be presented in section 3.3.

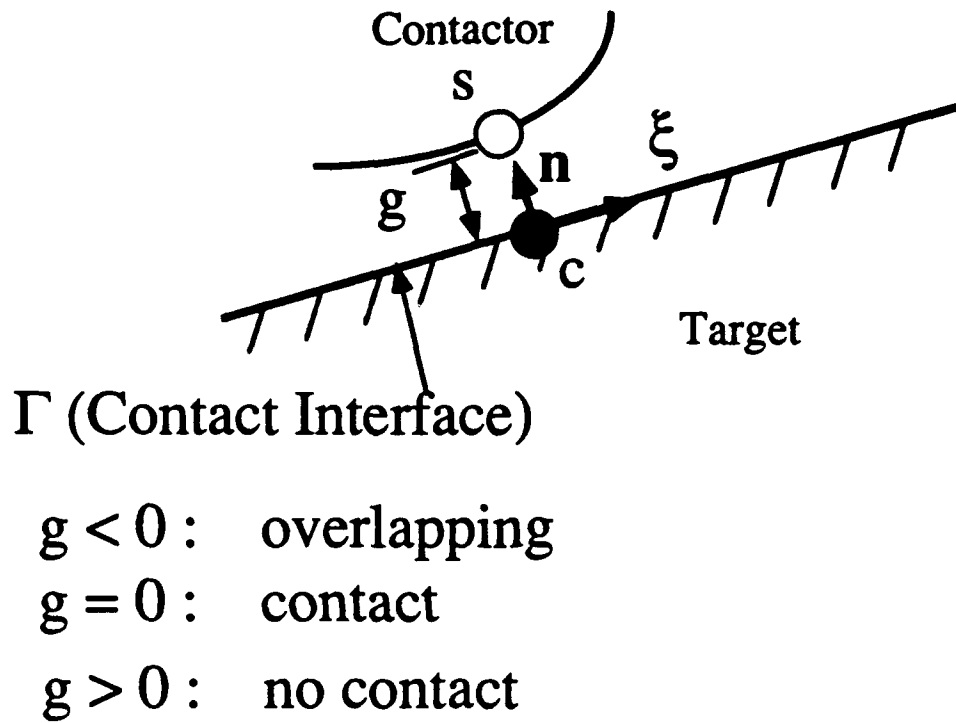


Figure 3.3 The definition of gap function in two-dimensional space.

3.2.3 Failure Analysis

The primary failure modes of interest were matrix cracking and delamination, hence fiber breakage was not considered. Failure criteria were proposed for predicting the occurrence of the initial failure. A fracture analysis based on the linear elastic fracture mechanics theory was also adopted for modeling the crack propagation once the damage initiated.

Prediction of Initial Failure

In order to predict initial damage, a matrix failure criterion and a delamination failure criterion [32, 44] were adopted. The matrix failure criterion can be described as

$$\left(\frac{\sigma_{yz}}{S_i}\right)^2 + \left(\frac{\sigma_{yy}}{Y_t}\right)^2 = e_m^2 \quad (3.13)$$

The occurrence of matrix cracking is predicted when the value of e_m is equal to or greater than unity.

The delamination failure criterion can be expressed as

$$\left(\frac{\sigma_{zz}}{Y_t}\right)^2 + \left(\frac{\sigma_{yz}^2 + \sigma_{xx}^2}{S_i^2}\right) = e_d^2 \quad (3.14)$$

The occurrence of delamination at the interface was predicted when the value of e_d was equal to or greater than unity. In Eq. (3.13) and Eq. (3.14), S_i is the *in-situ* interlaminar shear strength within the laminate under consideration, and Y_t is the *in-situ* ply transverse tensile strength [32]. σ_{yz} and σ_{xx} are the interlaminar shear stresses, and σ_{zz} and σ_{yy} are the out-of-plane normal stress and in-plane transverse normal stress respectively within the laminate under consideration.

Whenever the combined state of stresses satisfied either one of the criteria, initial failure was predicted. The corresponding failure criterion indicated the initial mode of failure. Once the initial failure was predicted, fracture analysis was applied

to simulate the growth of the local damage as the applied load continued to increase.

Modeling of Crack Propagation

In order to simulate crack propagation, a small initial crack was introduced immediately after the occurrence of the initial failure, depending upon the type of the failure mode. For matrix cracking, a vertical crack was immediately generated in the failed ply at the location where matrix cracking was predicted. The size of the crack was assumed to be equal to the thickness of the cracked ply group and fully extended to the interfaces of the neighboring plies, which have different ply orientations. However, if delamination was predicted as the initial failure mode, an initial delamination length about one ply thickness would be introduced at the predicted interface. The stresses and deformations of the laminate would then be recalculated at the same load, and fracture analysis would be applied to determine the growth of the initial failure and to model the propagation of the damage.

The mixed mode fracture criterion that was adopted to predict the initiation of crack propagation can be expressed as [42, 54, 53]:

$$\left(\frac{G_I}{G_{IC}} \right)^\alpha + \left(\frac{G_{II}}{G_{IIC}} \right)^\beta = E_d \quad (3.15)$$

where G_{IC} and G_{IIC} are the critical strain energy release rates corresponding to Mode I and Mode II fracture, respectively. It was assumed that the values of G_{IC} and G_{IIC} did not change with delamination length. $\alpha = 1$ and $\beta = 1$ were selected for this study because they were found to provide the best fit to the previous experiments [42].

The onset of crack growth was predicted when the value of E_d was equal to or greater than unity ($E_d \geq 1$). The strain energy release rates G_I and G_{II} for Mode I and Mode II fractures, respectively, could be expressed based on the linear elastic

fracture mechanics as

$$G_I = \lim_{\Delta a \rightarrow 0} \left\{ \frac{1}{2\Delta a} \int_0^{\Delta a} [u_n^+(a + \Delta a) - u_n^-(a + \Delta a)] \sigma_{nn} ds \right\} \quad (3.16.a)$$

$$G_{II} = \lim_{\Delta a \rightarrow 0} \left\{ \frac{1}{2\Delta a} \int_0^{\Delta a} [u_s^+(a + \Delta a) - u_s^-(a + \Delta a)] \sigma_{sn} ds \right\} \quad (3.16.b)$$

where Δa is the crack extension, n and s denote normal and sliding direction, σ_{nn} and σ_{sn} are the stresses at the crack tip associated with a delamination length of a , and u_n^+ , u_s^+ , and u_n^- , u_s^- are the displacements of the upper and lower surfaces of the delamination associated with a delamination length of $a + \Delta a$ respectively.

§3.3 FINITE ELEMENT MODELING

A nonlinear finite element code was developed for implementing the proposed model. The laminate was discretized by 4-node bilinear elements into n_{el} element domains with n_{np} nodal points using isoparametric 4-node bilinear rectangular elements as shown.

The displacement field is assumed to be in the form

$$u = \sum_{a=1}^{n_{en}} N_a u_a \quad (3.17)$$

where n_{en} is the number of nodes for one element, N_a is the displacement shape (interpolation) function associated with the local node number a , and u_a is the nodal displacement vector at the local node number a . The displacement shape functions in the parent domain with coordinates p and q are expressed as

$$N_a(p, q) = \frac{1}{4} (1 + pp_a) (1 + qq_a) \quad (3.18)$$

where $a = 1 - 4$ and there is no summation on a .

Now that both contact bodies are discretized by finite elements, any one of the contact bodies can be assigned as the contactor and the other will be treated

as the target. The nodal points on the contact region of the contactor are called "slave nodes," and those on the surface of the target are called "master nodes". The elements containing the master nodes are called "master elements," and the those containing the slave nodes are called "slave elements". The master-slave definition is shown in Figure. 3.4.

In the current formulation, the Lagrange multiplier distribution is assumed to be constant for a slave node associated with a master element along a crack or delamination interface. Thus, the extra term in the total potential energy due to the presence of Lagrange multipliers can be expressed as

$$\int_{\Gamma} \lambda_N g d\Gamma = \sum_{i=1}^{n_s} \int_{\Gamma_i} (\lambda_N)_i g_i d\Gamma_i \quad (3.19)$$

where n_s is the total number of slave nodes and therefore, the number of contact elements on the contact surfaces. Because of the constant contact pressure assumption for each contact element and the unique g for each contact element, the above equation can be written as

$$\int_{\Gamma} \lambda_N g d\Gamma = \sum_{i=1}^{n_s} (\lambda_N)_i g_i l_i \quad (3.20)$$

where l_i is the length of the i -th contact element. In the discrete space, the sum of the contact pressure $(\lambda_N l)_i$ must be carried by slave node s , which could be imagined as a nodal force with a magnitude of $(\lambda_N l)_i$. Thus, the extra term in the total potential energy due to the presence of Lagrange multipliers can be expressed as

$$\int_{\Gamma} \lambda_N g d\Gamma = \sum_{i=1}^{n_s} \lambda_i g_i \quad (3.21)$$

where the $\lambda_i (= (\lambda_N l)_i)$ at LHS of Eq. (3.21) is interpreted as the Lagrange multiplier for a slave node along some matrix crack or delamination interface.

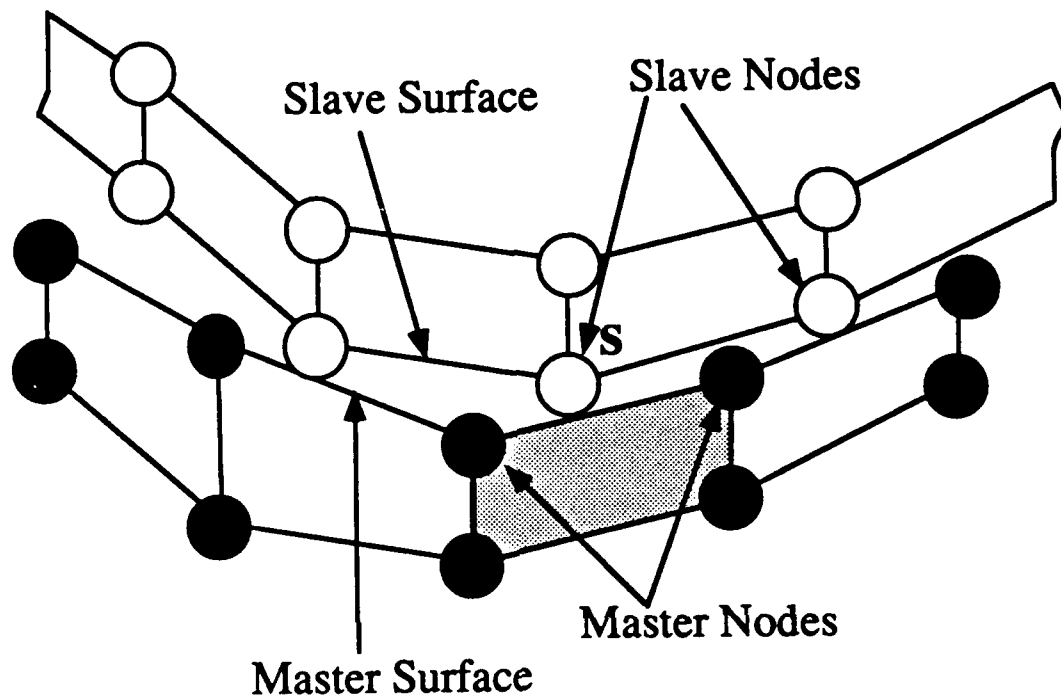


Figure 3.4 Description of master and slave surfaces for the contact problem in two-dimensional space.

3.3.1 Variational Formulation of the Discrete Problem

Accordingly, Eq. (3.6) can be written in its discrete form as

$$\bar{\Pi}(\mathbf{u}, \lambda) = \Pi(\mathbf{u}) + \lambda^T \mathbf{g} \quad (3.22)$$

where \mathbf{u} is the vector of nodal point displacements in discrete space, \mathbf{g} the vector of nodal gaps, and λ the vector of nodal contact forces. For simplicity, the subscript N is omitted for λ . In addition, $\Pi(\mathbf{u})$ designates the total potential energy associated with the bodies in contact. The discrete form of the virtual work principle results in

$$\frac{\partial \bar{\Pi}}{\partial \mathbf{u}} = \frac{\partial \bar{\Pi}}{\partial \lambda} \delta \mathbf{u} + \frac{\partial \bar{\Pi}}{\partial \lambda} \delta \lambda = \left(\frac{\partial \Pi}{\partial \mathbf{u}} + \lambda^T \frac{\partial \mathbf{g}}{\partial \mathbf{u}} \right) \delta \mathbf{u} + \mathbf{g}^T \delta \lambda = 0 \quad (3.23)$$

Therefore, the nonlinear equilibrium equations for the discrete system are obtained as

$$\left. \begin{aligned} \frac{\partial \Pi}{\partial \mathbf{u}} + \lambda^T \frac{\partial \mathbf{g}}{\partial \mathbf{u}} &= 0, \\ \mathbf{g} &= 0 \end{aligned} \right\} \quad (3.24)$$

In the framework of the finite element method, the term $\frac{\partial \Pi}{\partial \mathbf{u}}$ can be replaced by

$$\frac{\partial \Pi}{\partial \mathbf{u}} = \mathbf{P}_{\text{int}} - \mathbf{R}_{\text{ext}} \quad (3.25)$$

where \mathbf{P}_{int} is the vector of internal nodal forces resulting from the element stresses (corresponding to the strain energy part in the total potential energy Π), and \mathbf{R}_{ext} is the vector of nodal forces due to external loading. Term $\lambda^T \frac{\partial \mathbf{g}}{\partial \mathbf{u}}$ can be replaced by

$$\lambda^T \frac{\partial \mathbf{g}}{\partial \mathbf{u}} = \mathbf{F}_c \quad (3.26)$$

where the \mathbf{F}_c is the vector of contact nodal forces due to the contribution of contact nodes.

Combining Eq. (3.24), Eq. (3.25), and Eq. (3.26) results in

$$\left. \begin{aligned} \mathbf{P}_{\text{int}} + \mathbf{F}_c &= \mathbf{R}_{\text{ext}}, \\ \mathbf{g} &= 0 \end{aligned} \right\} \quad (3.27)$$

The first equation represents a weak form of equilibrium equation. The second indicates that the constraints are exactly enforced here. It is shown that λ represents the vector of contact forces, which are distributed according to the matrix $\frac{\partial \mathbf{g}}{\partial \mathbf{u}}$ in the associated nodes.

In general, due to the finite deformation and the contact constraints, the system of equations is nonlinear. Numerical techniques such as the Newton-Raphson method have been widely used to solve these nonlinear equations [70–74].

By applying the Newton-Raphson technique, the following linearized equations are obtained:

$$\left. \begin{aligned} \frac{\partial}{\partial \mathbf{u}} [\mathbf{P}_{\text{int}} + \mathbf{F}_c] d\mathbf{u} + \frac{\partial}{\partial \lambda} [\mathbf{P}_{\text{int}} + \mathbf{F}_c] d\lambda &= \mathbf{R}_{\text{ext}} - (\mathbf{P}_{\text{int}} + \mathbf{F}_c), \\ \frac{\partial \mathbf{g}}{\partial \mathbf{u}} d\mathbf{u} &= -\mathbf{g} \end{aligned} \right\} \quad (3.28)$$

Recalling that \mathbf{P}_{int} is the function of \mathbf{u} only and \mathbf{F}_c is the function of \mathbf{u} and λ , the above equation can be written as

$$\left. \begin{aligned} \left[\frac{\partial}{\partial \mathbf{u}} (\mathbf{P}_{\text{int}}) + \frac{\partial}{\partial \mathbf{u}} (\mathbf{F}_c) \right] d\mathbf{u} + \left[\frac{\partial}{\partial \lambda} (\mathbf{F}_c) \right] d\lambda &= \mathbf{R}_{\text{ext}} - (\mathbf{P}_{\text{int}} + \mathbf{F}_c), \\ \frac{\partial \mathbf{g}}{\partial \mathbf{u}} d\mathbf{u} &= -\mathbf{g} \end{aligned} \right\} \quad (3.29)$$

The above equations can be written in matrix form:

$$\left. \begin{aligned} (\mathbf{K} + \mathbf{K}_c) d\mathbf{u} + \mathbf{H} d\lambda &= \mathbf{R}_{\text{ext}} - (\mathbf{P}_{\text{int}} + \mathbf{F}_c), \\ \mathbf{H}^T d\mathbf{u} &= -\mathbf{g} \end{aligned} \right\} \quad (3.30)$$

where \mathbf{H}^T is the transpose of \mathbf{H} .

In this matrix formulation, \mathbf{K} is the classical tangent stiffness matrix which is obtained without considering the contact between crack interfaces, and is the standard practice in finite element formulation [70–74] and therefore omitted here.

\mathbf{F}_c is the contact residual force vector and defined as

$$\mathbf{F}_c = \lambda \frac{\partial \mathbf{g}}{\partial \mathbf{u}} \quad (3.31)$$

\mathbf{K}_c is the contribution of the contact conditions to the tangent stiffness matrix, which guarantees the best approximation to the actual response. It is defined as

$$\mathbf{K}_c = \frac{\partial \mathbf{F}_c}{\partial \mathbf{u}} \quad (3.32)$$

\mathbf{H} is a vector that sets up the distribution of contact forces due to the contact and is defined as

$$\mathbf{H} = \frac{\partial \mathbf{g}}{\partial \mathbf{u}} \quad (3.33)$$

In the following section, it is convenient to refer the equations to an element coming in contact with one node on the other body, forming one contact element. Such an element provides one gap g and one Lagrange multiplier λ and has N nodal points. Subsequently, capital letter indices are used here to identify quantities which are related to the element nodal points. Moreover, for repeated indices the summation convention of tensor calculus holds. The corresponding form of Eq. (3.30) for one contact element is

$$\left. \begin{aligned} \left\{ \frac{\partial \mathbf{P}_{\text{int}}^{\mathbf{M}}}{\partial \mathbf{u}^N} + \lambda \frac{\partial}{\partial \mathbf{u}^N} \left(\frac{\partial g}{\partial \mathbf{u}^M} \right) \right\} d\mathbf{u}^N + \frac{\partial g}{\partial \mathbf{u}^N} d\lambda &= \mathbf{R}_{\text{ext}}^{\mathbf{M}} - (\mathbf{P}_{\text{int}}^{\mathbf{M}} + \mathbf{F}_c^{\mathbf{M}}), \\ \frac{\partial g}{\partial \mathbf{u}^N} d\mathbf{u}^N &= -g \end{aligned} \right\} \quad (3.34)$$

where the contact residual force of the element is

$$\mathbf{f}_c = \lambda \frac{\partial g}{\partial \mathbf{u}^M} \quad (3.35)$$

The two terms in parentheses form the tangent stiffness matrix of the element. The first term is the classical tangent stiffness matrix for undamaged composites. The derivation of the matrix is available in the literature related to finite element methods [70–74]. The second term adding to the contribution due to contact has the following form:

$$\mathbf{k}_c = \frac{\partial \mathbf{f}_c}{\partial \mathbf{u}^N} = \lambda \frac{\partial}{\partial \mathbf{u}^N} \left(\frac{\partial \mathbf{g}}{\partial \mathbf{u}^M} \right) \quad (3.36)$$

The correct derivation of contact element stiffness matrix \mathbf{k}_c is important, as it renders the quadratic convergence of Newton's method. The coefficient matrix before the $d\lambda$ forms the contact force distribution of the associated nodes of the contact element. The derivations of the contact stiffness matrix \mathbf{k}_c and the residual force \mathbf{f}_c are described in Appendix B.

3.3.2 Finite Element Modeling of Failure

Once the strain and stress distributions in the laminate at each load increment were calculated, failure criteria were applied to determine the locations of the initial damage and the applied load corresponding to the initial failure. When intraply or interply cracking was predicted, it was necessary to insert a crack in remodeling the finite element grids within and near the cracked area. However, because the location of the crack was unknown prior to failure and also strongly dependent upon the ply orientation, it became very difficult to efficiently insert an intraply or interface crack in the existing mesh and effectively remesh the finite element grids while the ply orientation and the geometry of the laminate were considered as variables.

Therefore, an efficient and effective technique was developed and implemented in the finite element mesh generator. The technique used the original finite element grid system, and preserved the sparseness of the tangent stiffness matrix after failure occurred. Hence the computational time did not increase substantially. When a

crack was predicted, it was assumed that the location of the crack could be assigned as an approximation to the nearest element boundary. Accordingly, a matrix crack with a length of a ply group thickness would be generated along the existing element interfaces of the failed ply group. Similarly, for a delamination crack, the interfacial crack would be introduced at the boundary of the elements along the predetermined ply interface.

Based on this approach, each node was systematically assigned four node numbers (rather than one) in the global nodal numbering system. If no damage occurred, the four nodes were assigned the same equation numbers. Once a crack was generated, depending upon the type of crack and the location of the node, each node along the cracked surfaces could be generated with its own nodal number, up to four individual nodes. Accordingly, additional crack surfaces could be generated by splitting the nodes at the desired locations. Hence, no changes in the mesh were required for the post-failure analysis. Details of the mesh remodeling procedure are given in Appendix A.

Once a crack was introduced into the composite, the surface condition of the crack during the subsequent loading had to be modeled properly to prevent overlapping of the crack surfaces. It was assumed that once matrix cracking occurred, the crack would fully extend to the neighboring interfaces of plies with ply orientations differing from the cracked ply group and would branch into a delamination crack along each interface. In order to apply fracture mechanics for determining the growth of the matrix cracking-induced delamination, an initial delamination crack along the interface perpendicular to the matrix crack was generated at the tips of the existing matrix crack. Thus, the strain energy release rates at the delamination tips along the interface could be determined based on the crack closure technique

(Eqs. 3.16) [48] as follows:

$$\begin{aligned} G_I &\approx \lim_{\Delta a \rightarrow 0} \left\{ \frac{1}{2\Delta a} F_{nM}(u_{nD} - u_{nM}) \right\} \\ G_{II} &\approx \lim_{\Delta a \rightarrow 0} \left\{ \frac{1}{2\Delta a} F_{sM}(u_{sD} - u_{sM}) \right\} \end{aligned} \quad (3.37)$$

where M and N are the nodes at the crack tip before the crack advances an amount of Δa , F_{nM} and F_{sM} are the nodal forces that keep the nodes M and N together, and Δa is chosen to be the length of the element ahead of the crack tip along the delamination interface.

It was assumed that the matrix cracking-induced delamination crack would propagate if the calculated strain energy release rates G_I and G_{II} satisfied the crack growth criterion of Eq. (3.15). Subsequently, the delamination crack would advance by one element size, and the mesh with additional crack surfaces would require remodeling following the procedures given in Appendix A. Accordingly, Eq. (3.27) needed to be resolved with additional crack surfaces. The above numerical procedures would need to be continued until either the composite could not sustain any additional load or the calculated results would be beyond the scope of the present interest.

§3.4 Verification

In order to verify the model, numerical calculations based on the model were compared with the available analytical and experimental results. Experiments were also performed during the investigation to further validate the model.

3.4.1 Comparison with Existing Results

A DCB Specimen under a Line Load

Numerical calculations were performed to determine the strain energy release

rates of a double cantilever beam subjected to a constant tip displacement under three different loading conditions. The results of the calculations are presented in Figure 3.5.

Figure 3.5 shows the strain energy release rate calculations for Mode I, Mode II, and mixed mode fracture, as a function of the crack length under a constant applied displacement at the crack tip. The solid lines represent the results of the beam theory and the symbols are the predictions based on the present analysis. The predictions agreed very well with the classical beam theory [45]. For mixed mode fracture, G_I and G_{II} were calculated for the model and are presented in Figure 3.5, in addition to the total strain energy release rate $G = G_I + G_{II}$.

A Unidirectional Composite under Three-Point Bending

Calculations were made to compare the prediction with the test data (Figure 3.6) measured from experiments in which a unidirectional composite beam containing a central delamination was tested under three-point bending (by Maikuma et al. [43]). The Strain energy release rates with respect to the crack length were measured. The open symbols represent the test data, and the solid line represents the predictions from the model. The predictions agreed with the test data reasonably well.

[90_m/0_n/90_m] Specimens with a Surface Crack

Comparisons were also made between the predictions based on the model and the test data measured by Sun et al. [46] on a simply supported [90₅/0₅/90₅] composite beam containing an interface delamination induced by a surface matrix crack (bending crack) located at the center of the bottom ply. The test was performed to evaluate the effect of a bending crack on the strain energy release rates at the tip of a delamination. Figure 3.7 presents the comparison of strain energy release rates between the calculated rates based on the model and those given in [46]. A

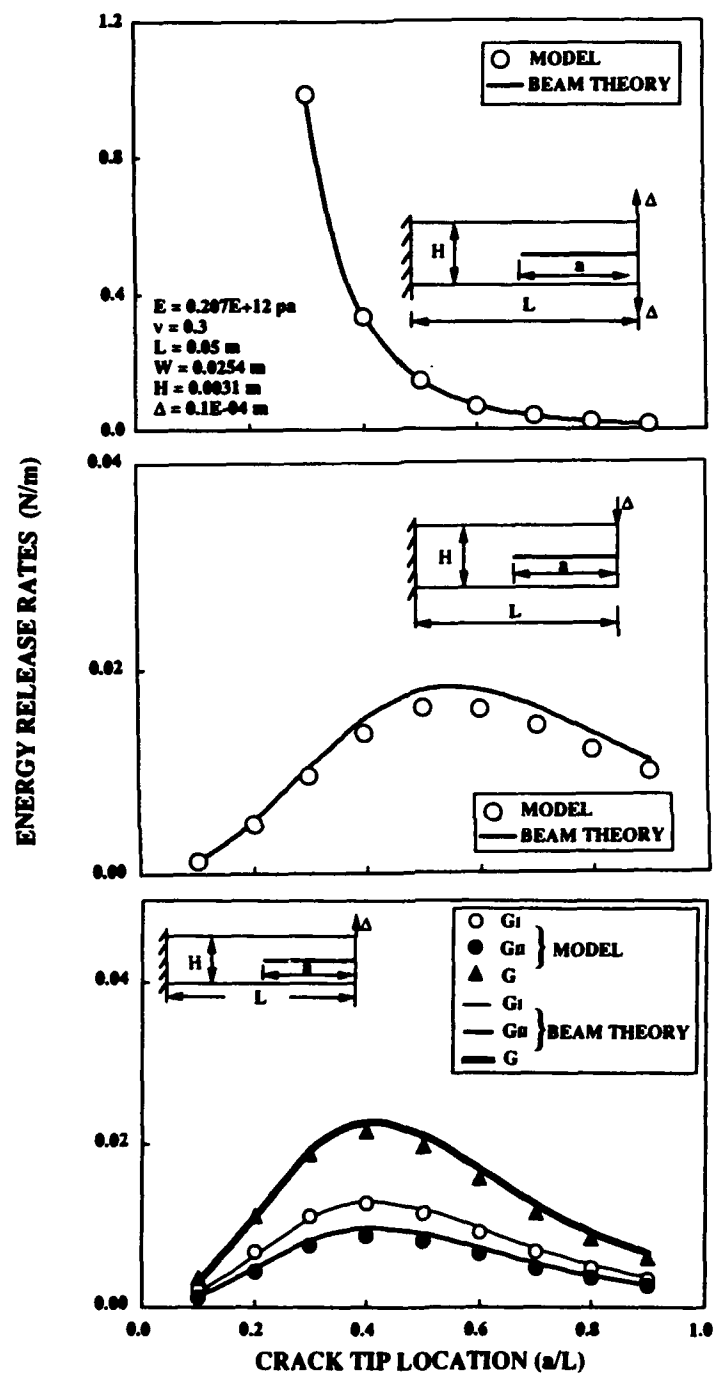


Figure 3.5 Strain energy release rates of an isotropic beam as a function of the crack length. Comparison is between the predictions based on the present model and the calculations based on the classical beam theory [45]. a) Mode I; b) Mode II; and c) Mixed Mode.

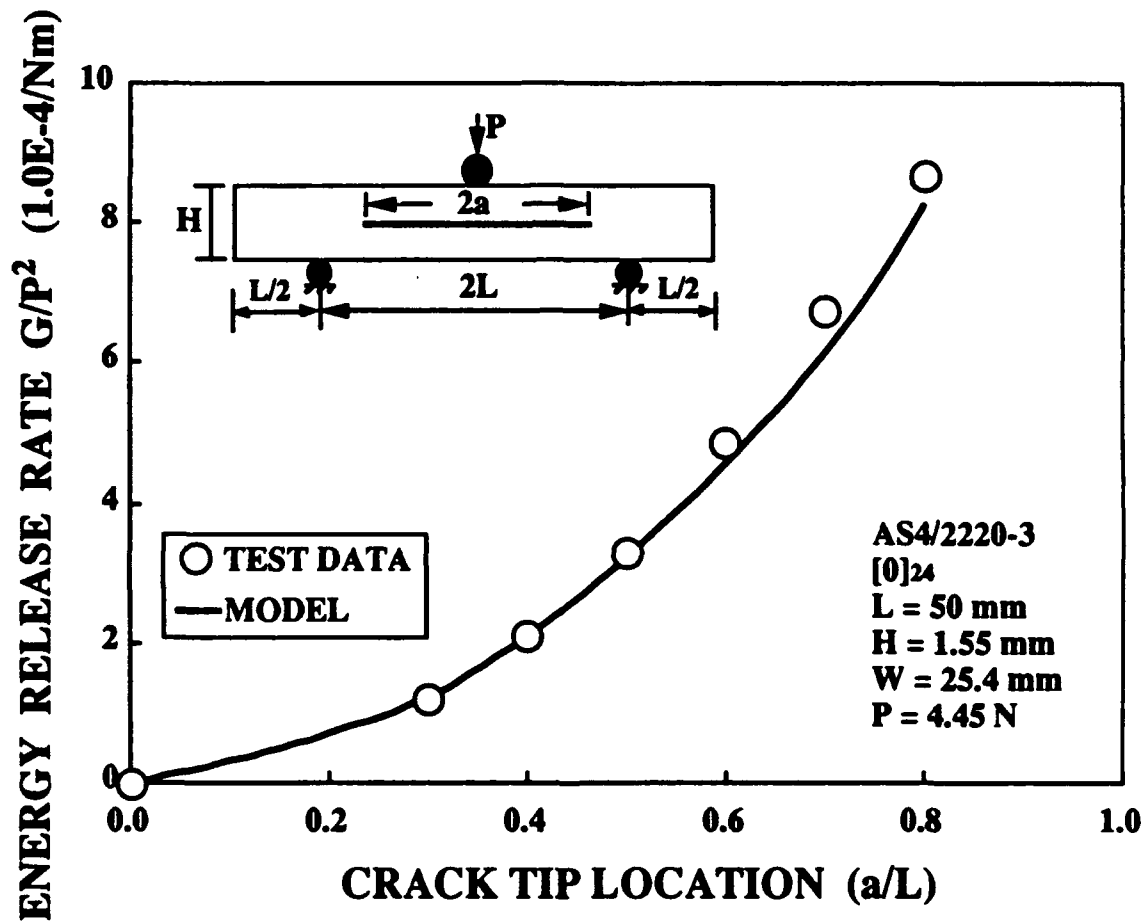


Figure 3.6 Comparison of the strain energy release rate of an AS4/2220-3 $[0]_{24}$ composite beam between the data taken from [43] and the predictions based on the present model.

fairly good agreement was found. It was noticed that Mode I was the dominant mode for the crack growth. Figure 3.8 shows the relationship between the critical load associated with the onset of the delamination growth and the delamination length for the laminate under a three point bending test. The rectangular symbol represents the test data. The solid line is the prediction. The prediction was based on the assumption that the critical strain energy release rates G_{IC} and G_{IIC} were constant for the given material and independent of the delamination length. Again, the predictions agreed with the data very well.

The numerical simulations of the deformed configurations of a $[90_8/0_4]_s$ composite specimen with a bending crack as a function of the applied load are presented in Figure 3.9. The calculated load and the interface delamination versus the displacement of the load head were also calculated and are presented in Figure 3.10. Clearly, the interfacial delamination induced by the bending crack grew gradually with the increasing applied load or displacement, indicating a very stable crack growth. The strain energy release rates were calculated and are presented in Figure 3.11, which shows again that Mode I was the dominant mode during delamination growth.

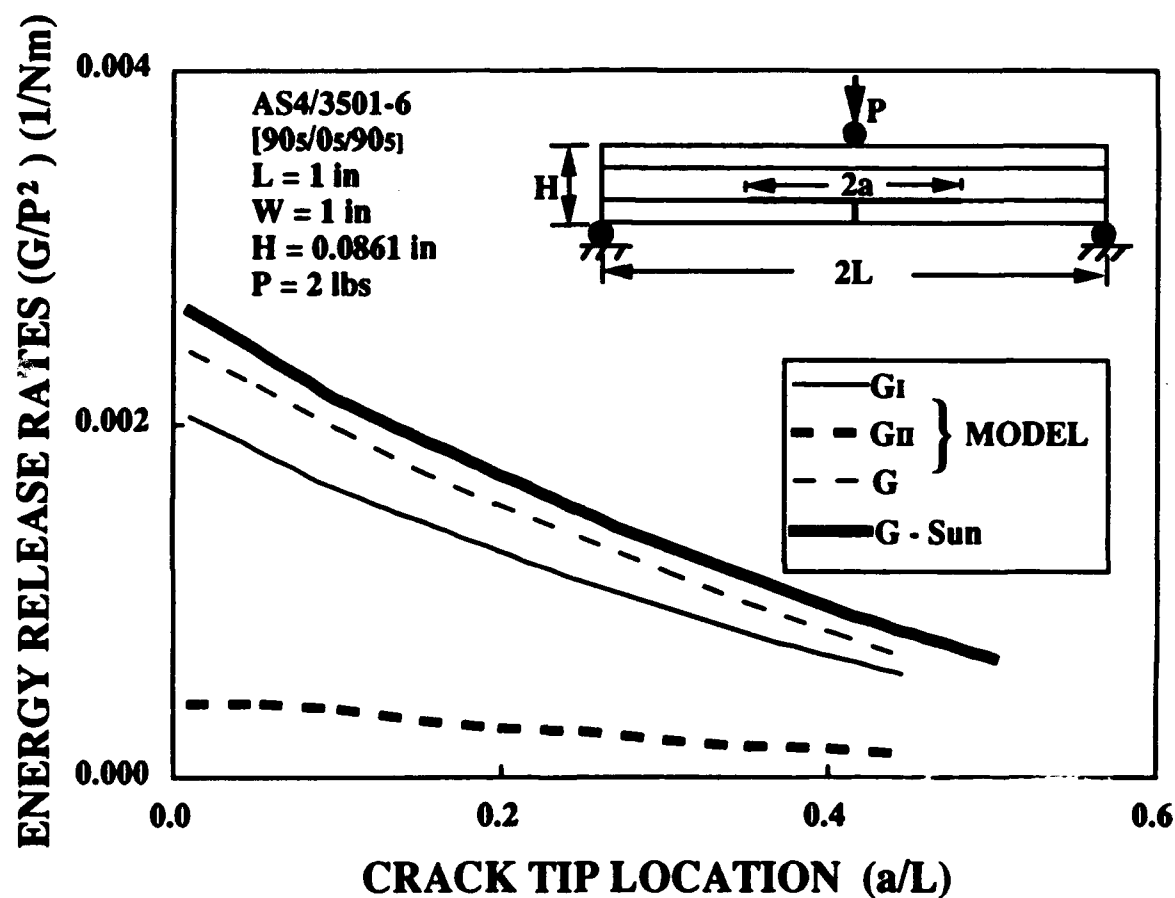


Figure 3.7 Strain energy release rate of an AS4/3401-6 [90_s/0_s/90_s] composite beam as a function of the delamination length induced by a surface matrix crack. Comparison is between the predictions based on the present model and the calculations given in [46].

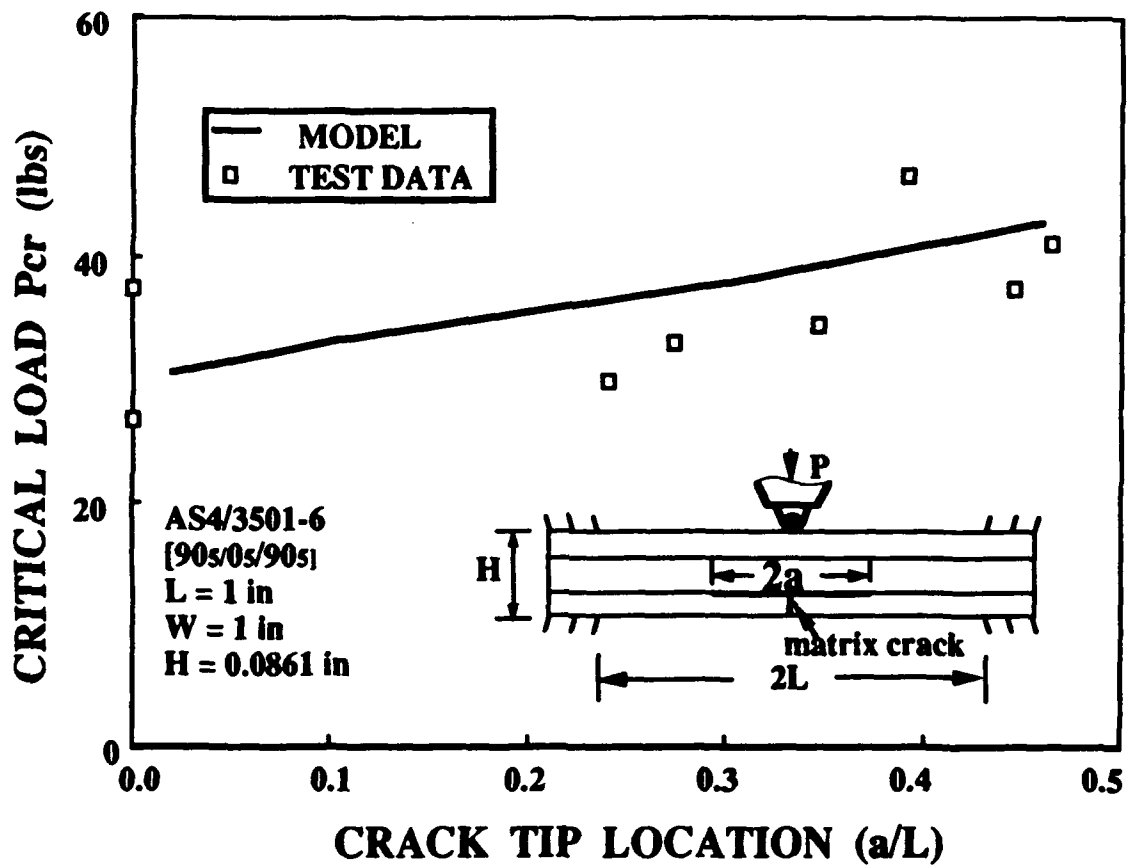


Figure 3.8 Comparison between the measured [46] and the predicted critical loads of an AS4/3401-6 [90_s/0_s/90_s] composite beam as a function of the delamination length induced by a surface matrix crack.

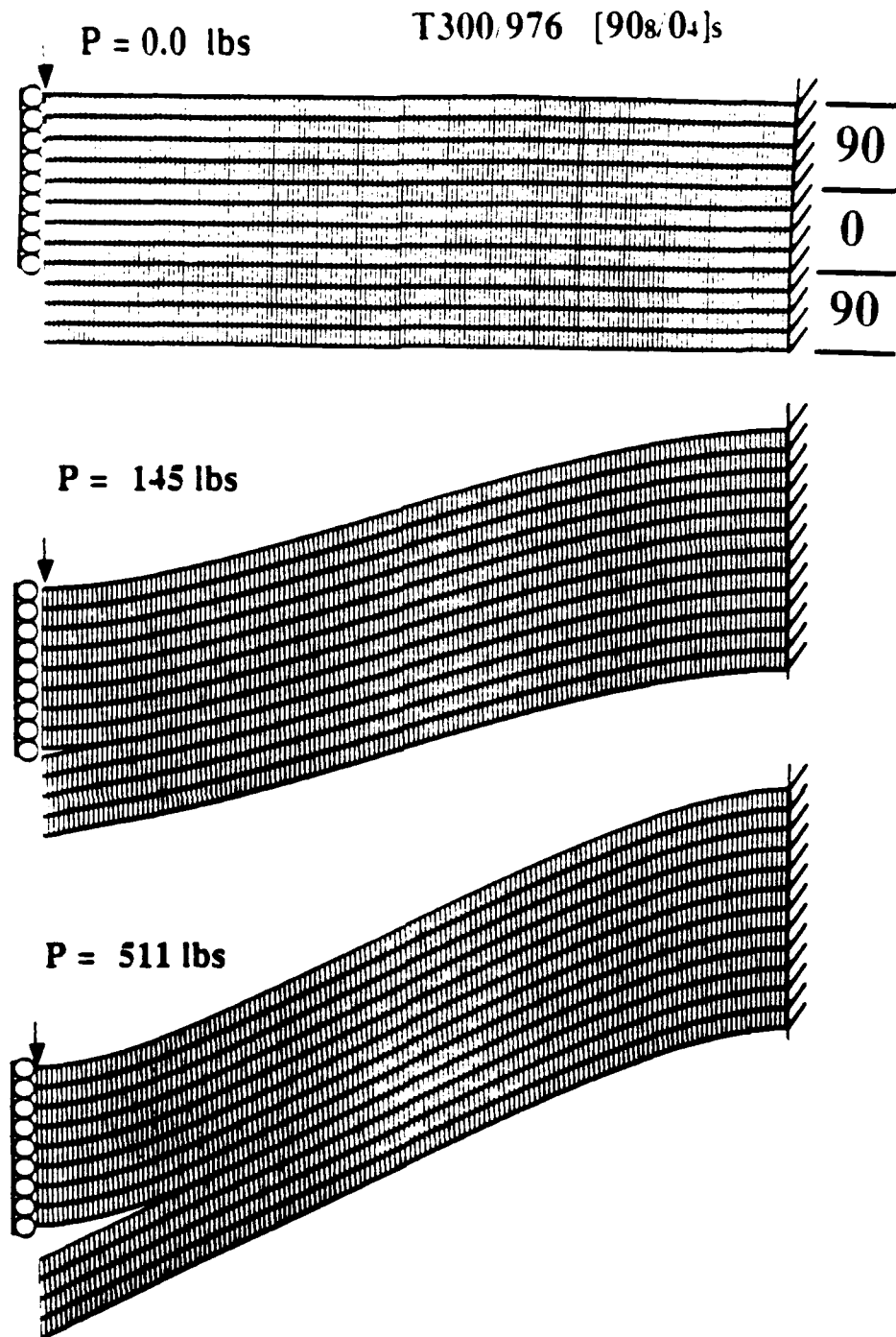


Figure 3.9 Numerical simulations of the deformed configurations of a T300/976 $[90_8/0_4]_s$ composite beam containing an existing matrix crack and subjected to a transverse concentrated line load at various loading stages.

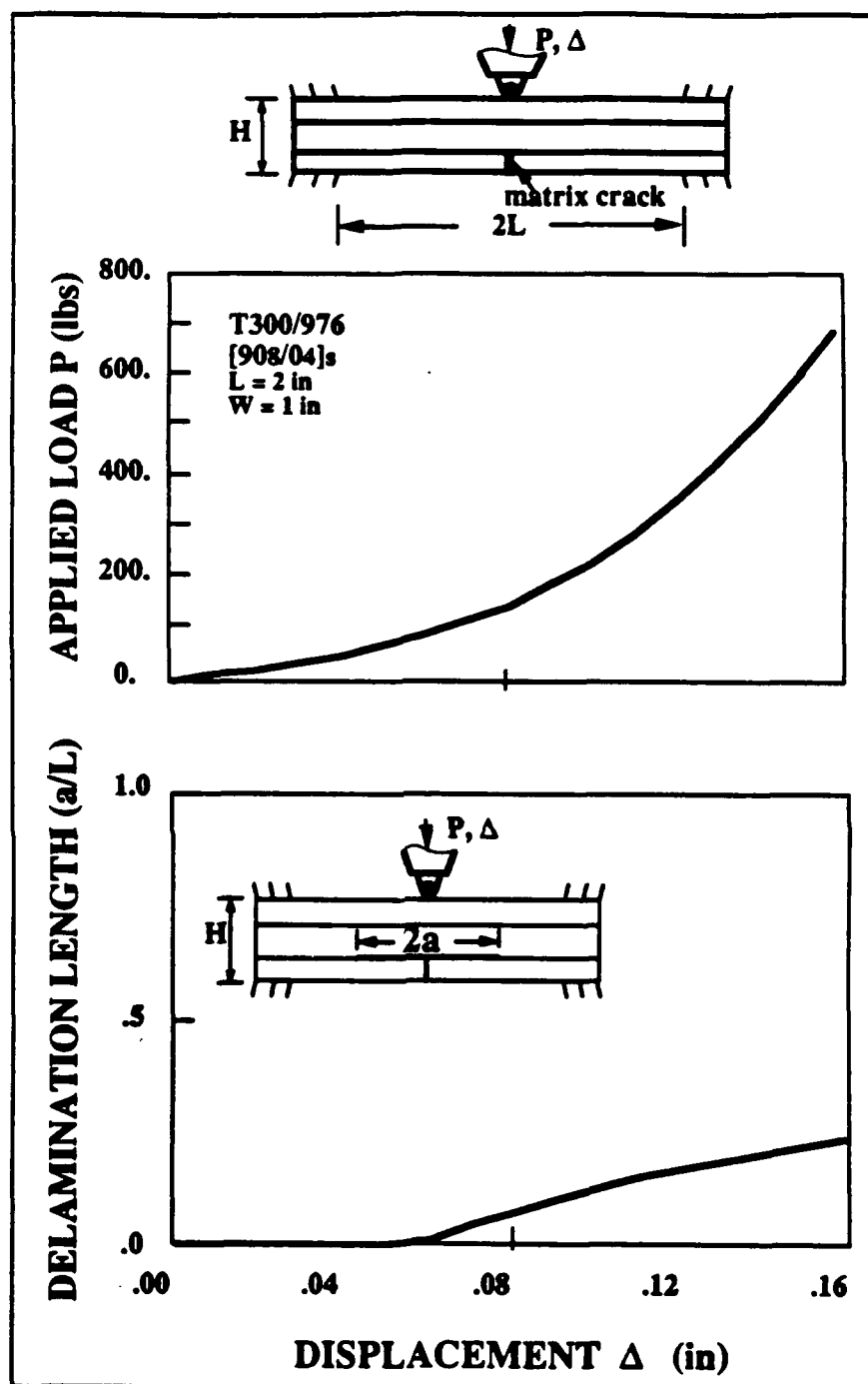


Figure 3.10 The calculated response of a T300/976 [90₈/0₄]_s composite beam containing a bending crack and subjected to a transverse concentrated line load. (Above): The calculated applied load as a function of the load head displacement. (Below): The extent of the delamination induced by the matrix crack as a function of the load head displacement.

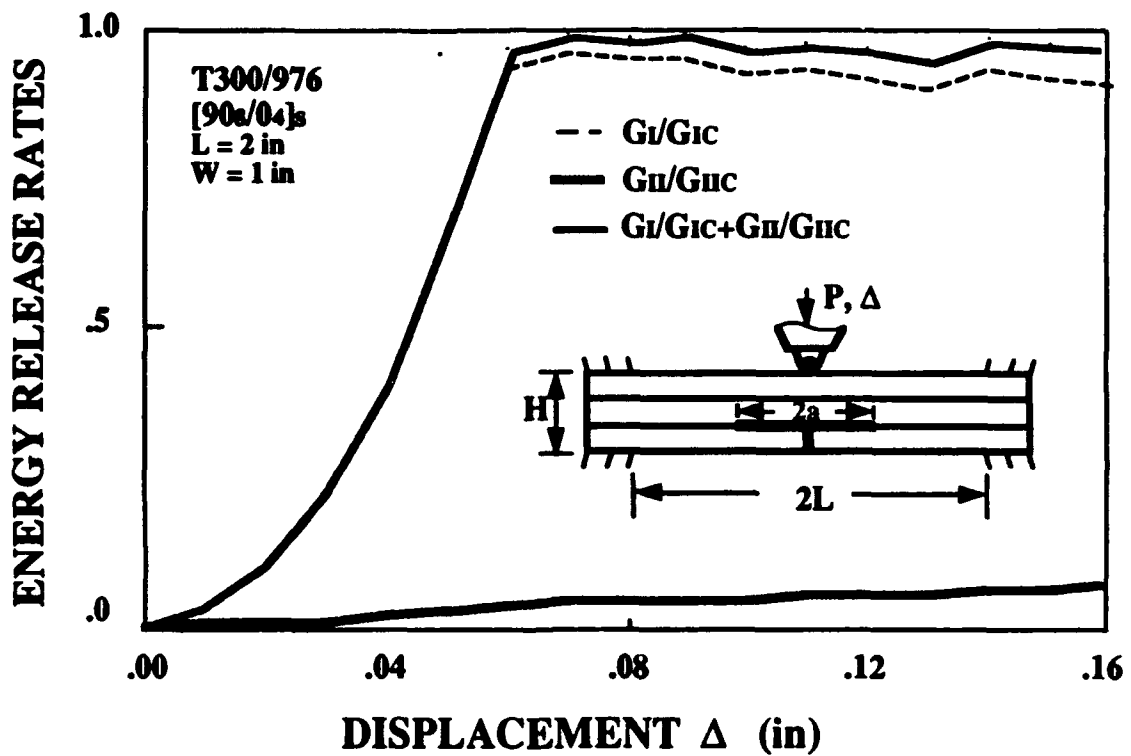


Figure 3.11 The ratios of the calculated strain energy release rates corresponding to the delamination growth as a function of the load head displacement.

Table 3-1
Material properties used in the calculations for comparisons.

| | Aluminum | T300/976 | AS4/3501-6 | AS4/2220-3 |
|----------------------|----------|----------|------------|------------|
| E_x , (msi) | 10.0 | 17.6 | 17.4 | 17.84 |
| E_y , (msi) | 10.0 | 1.41 | 1.43 | 1.61 |
| E_z , (msi) | 10.0 | 1.41 | 1.43 | 1.61 |
| ν_{xy} | 0.3 | 0.29 | 0.30 | 0.29 |
| ν_{xz} | 0.3 | 0.29 | 0.30 | 0.29 |
| ν_{yz} | 0.3 | 0.40 | 0.30 | 0.40 |
| G_{xy} , (msi) | 3.846 | 0.81 | 0.76 | 0.908 |
| G_{xz} , (msi) | 3.846 | 0.81 | 0.76 | 0.908 |
| G_{yz} , (msi) | 3.846 | 0.50 | 0.76 | 0.623 |
| G_{IC} , (lbf/in) | n/a | 0.50 | 0.47 | n/a |
| G_{IIc} , (lbf/in) | n/a | 1.80 | 1.88 | 2.80 |

For the materials T300/976, AS4/3501-6 and AS4/2220-3, it is necessary to specify the direction in which the fibers of each lamina are aligned. The subscript x denotes the fiber or 0 deg direction. The subscript y denotes the direction perpendicular to the 0 deg direction (transverse or 90 deg direction). The subscript z denotes the out-of-plane direction.

3.4.2 Comparison with the Current Test Data

Tests were also performed during the investigation, and the results of the test data were utilized to substantiate the model. The major focus of the tests was concentrated on damage in the cross-ply laminates $[0_m/90_n]_s$ containing inner 90° plies and outer 0° plies. For $[90_m/0_n]_s$ composites, tests have been conducted by Sun et al. [46] and the model was verified in the previous section.

T300/976 Graphite/Epoxy prepreps were selected for fabricating both flat and cylindrical test panels, which were cured under a standard cure cycle given in [32]. The panels were then sliced into specimens. The dimensions and the ply orientations of the specimens are listed in Table 3-2. The material properties for Fiberite T300/976 are shown in Table 3-3. Each specimen was X-rayed to examine any internal damage resulting from manufacturing or cutting. No apparent sign of damage was found in the X-radiographs of the test specimens.

Each specimen was clamped firmly at both ends during the test. The fixtures fabricated specifically for testing of flat and curved specimens are shown in Figure 3.12. A line-nosed cylindrical load head was applied downward at the centerline of the specimen. The configuration of the test setup is also given in Figure 3.12. An MTS machine was utilized for all the tests. The load head speed was 0.0006 in/min based on displacement-controlled loading. A strain gage was mounted at the center of each specimen. The strain gage reading or the displacement reading as a function of the applied load was recorded during the entire test until the applied load dropped substantially, as a result of internal damage in the specimens.

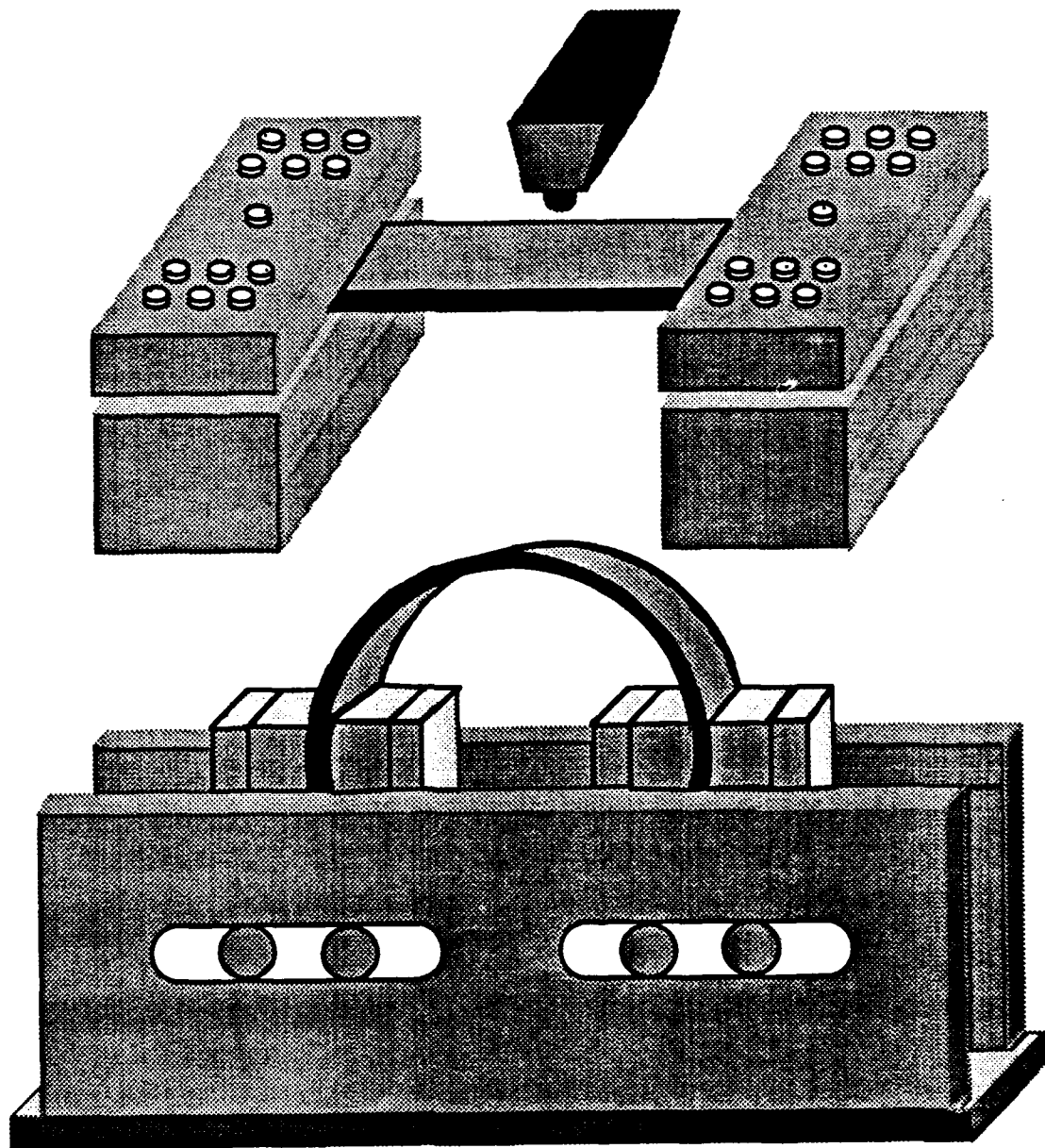


Figure 3.12 Schematics of the testing fixtures. (Above): The testing fixture for flat panels. (Below): The testing fixture for cylindrical panels.

Table 3-2

Ply orientations and geometry of test specimens.

| Flat Panels | L (in) | W (in) | H (in) | No. of Specimens |
|-----------------------|--------------------|----------|----------|------------------|
| $[0_6/90_3]_s$ | 1.5 | 0.955 | 0.098 | 4 |
| $[0_4/90_4]_s$ | 1.5 | 1.030 | 0.0896 | 4 |
| $[0_4/90_3/0_2]_s$ | 1.5 | 0.920 | 0.098 | 5 |
| $[0_3/90_2/0_3/90]_s$ | 1.5 | 0.930 | 0.098 | 5 |
| Curved Panels | 2α (degree) | W (in) | H (in) | No. of Specimens |
| $[0_6/90_3]_s$ | 81 | 0.970 | 0.098 | 5 |
| $[0_8/90_2]_s$ | 81 | 0.930 | 0.110 | 5 |

L represents the span length. W represents the plate width. H represents the plate thickness. 2α represents the arc angle for curved panels. The radius for the curved panels is 2.86 in.

Table 3-3
Material properties for Fiberite T300/976.

| Material Property | Value | Units |
|--|-------|--|
| Longitudinal Young's modulus, E_x | 17.6 | msi |
| Transverse Young's modulus, E_y | 1.41 | msi |
| Out-of-plane Young's modulus, E_z | 1.41 | msi |
| Poisson's ratio, ν_{xy} | 0.29 | |
| Poisson's ratio, ν_{xz} | 0.29 | |
| Poisson's ratio, ν_{yz} | 0.40 | |
| In-plane shear modulus, G_{xy} | 0.81 | msi |
| Out-of-plane shear modulus, G_{xz} | 0.81 | msi |
| Out-of-plane shear modulus, G_{yz} | 0.50 | msi |
| Longitudinal thermal expansion coefficient, α_{xx} | 0.3 | $\frac{\mu\text{in}}{\text{in}^\circ\text{F}}$ |
| Transverse thermal expansion coefficient, α_{yy} | 16.0 | $\frac{\mu\text{in}}{\text{in}^\circ\text{F}}$ |
| Longitudinal tensile strength, X_t | 220 | ksi |
| Longitudinal compressive strength, X_c | 231 | ksi |
| Transverse tensile strength, Y_t | 6.46 | ksi |
| Transverse compressive strength, Y_c | 36.7 | ksi |
| Longitudinal shear strength (cross ply), S_{cp} | 15.5 | ksi |
| Critical strain energy release rate for Mode I, G_{Ic} | 0.50 | lbf/in |
| Critical strain energy release rate for Mode II, G_{IIc} | 1.80 | lbf/in |

Flat Panels

The test data of flat panels with $[0_6/90_3]_s$ and $[0_4/90_4]_s$ ply orientations are shown in Figure 3.13 and Figure 3.14. The open circles shown in these figures are the test data. As can be seen from the figures, the material responses between the applied load and the measured strains were quite linear until the maximum load was reached, after which the load dropped sharply. Below the maximum load, no visual damage was observed during the test. However, significant damage including multiple matrix cracks and delaminations was found immediately after the load drop, indicating that the damage occurrence and growth were not progressive, but unstable and catastrophic. Apparently, once the damage initiated, it immediately propagated extensively inside the material and resulted in catastrophic failure. A photograph of a close view of the side of a damaged specimen near the center region is presented in Figure 3.15.

Numerical simulations of the test results are also shown in Figure 3.13 and Figure 3.14, represented in the same figures by the solid lines. The calculated load-strain relationships matched with the data very well up to the final failure load. Initial failure due to matrix cracking in the central 90° plies was predicted at the failure load in both cases. The calculated load dropped significantly due to an extensive delamination which occurred at the interface between the bottom ply group and the central 90° plies, resulting from the matrix cracks. Following the calculation, once the matrix cracks initiated, they immediately produced an interface delamination which propagated instantly to the boundaries. The numerical simulations of the deformed configurations of a $[0_4/90_4]_s$ composite specimen as a function of the applied load are presented in sequence in Figure 3.16. It is noted that additional matrix cracking was also predicted at other locations within the central 90° plies during the unstable delamination propagation. The calculated

load and the lower interface delamination versus the displacement of the load head were also calculated and are presented in Figure 3.17. Clearly, the lower interface delamination grew immediately to the boundaries directly after the critical load was reached.

Cylindrical Panels

Figure 3.18 and Figure 3.19 show respectively the load-deflection relationships of $[0_6/90_3]_s$ and $[0_8/90_2]_s$ cylindrical panels subjected to concentrated central line loading. Symbols in both figures represent the test data, and the solid lines are the predictions based on the model. Each symbol corresponds to a single specimen. Both types of specimens resulted in the same type of damage mode: a pair of shear cracks occurring in the 90 degree plies, leading to an upper and lower interface delamination along the 0/90 interfaces. A photograph of a side view of a $[0_6/90_3]_s$ specimen after testing is presented in Figure 3.15. The type of damage was basically similar to that observed in $[0/90]_s$ flat composites. However, the overall extent of the delamination along the bottom 0/90 interface in the cylindrical panels was smaller than that of corresponding flat panels.

The predicted curves shown in Figure 3.18 and Figure 3.19 agreed with the test data very well from the initial loading to final collapse. As predicted, the damage was initiated from matrix cracking in 90 degree plies inside the laminates and the interface delaminations were generated from the matrix cracking. The predicted locations of the initial matrix cracks and the extent of the delamination along the bottom 0/90 interface in the cylindrical panels as compared to test measurements are presented in Table 3-4.

A typical deformed configuration of a segment of a $[0_6/90_3]_s$ cylindrical composite corresponding to the final failure load is presented in Figure 3.20. A significant amount of slip deformation can be seen between the upper and lower surfaces of the

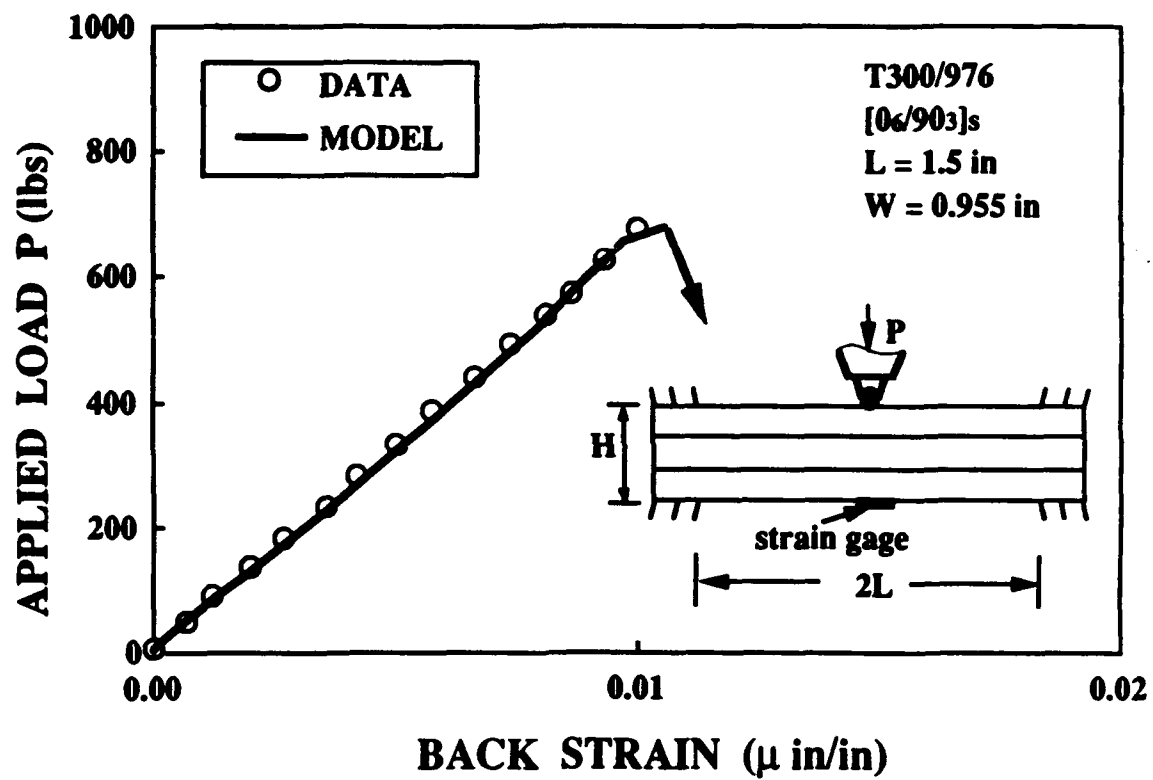


Figure 3.13 Comparison between the measured and the calculated load-strain relationship of a T300/976 [0₆/90₃]_s composite beam subjected to a concentrated line load.

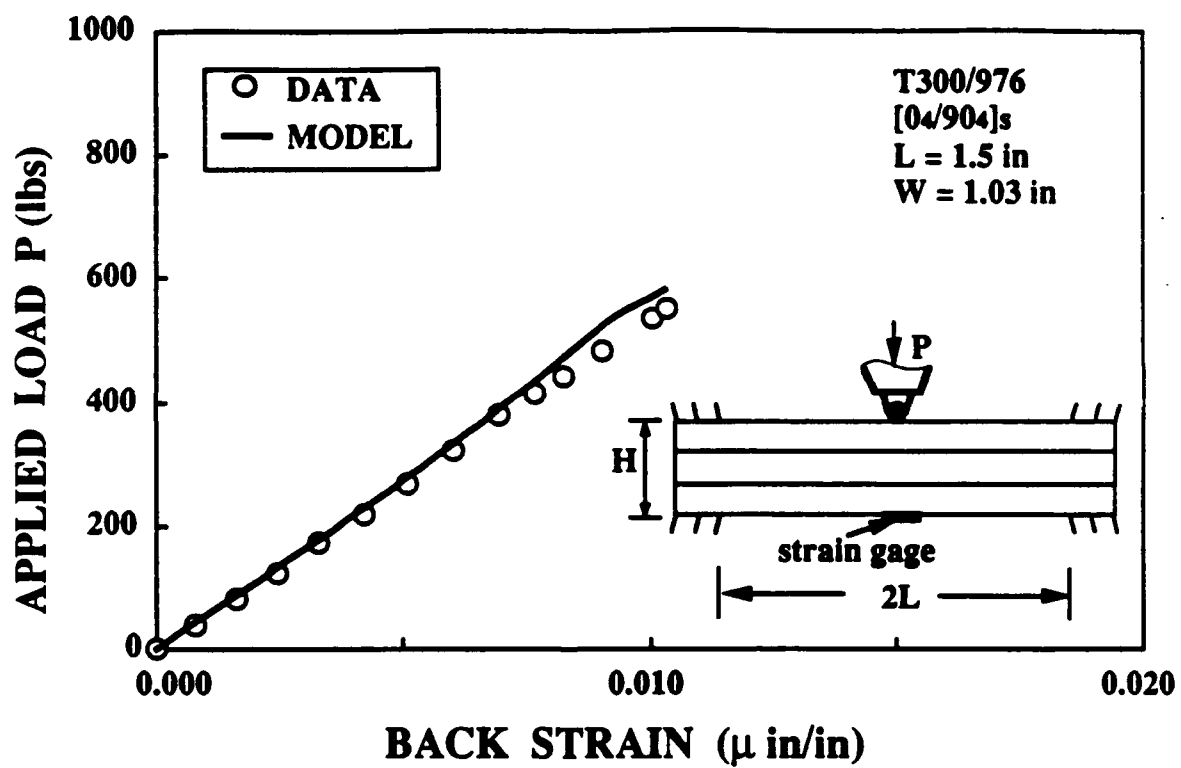


Figure 3.14 Comparison between the measured and the calculated load-strain relationship of a T300/976 [0₄/90₄]_s composite beam subjected to a concentrated line load.

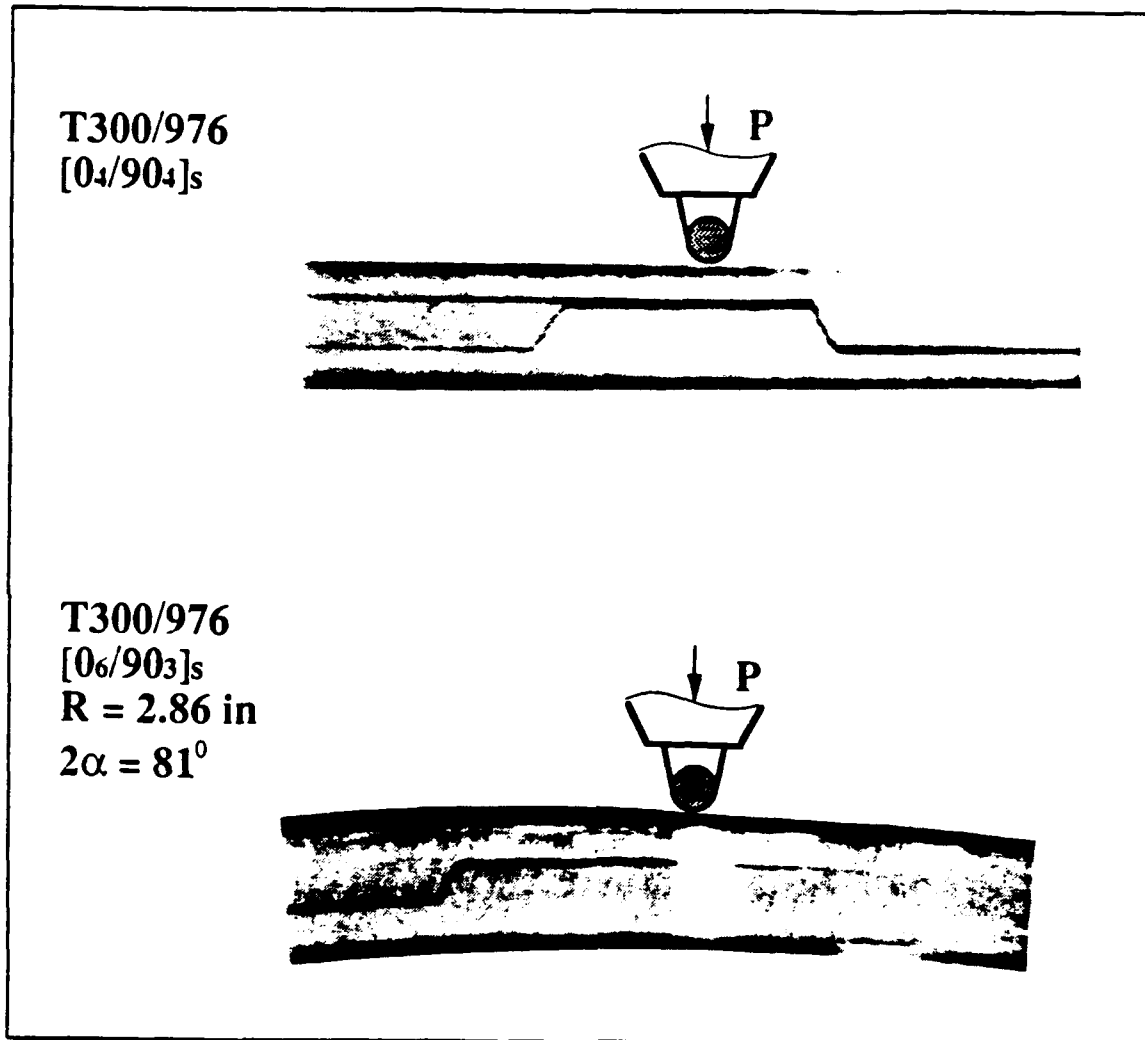


Figure 3.15 Photographs of a sideview of a tested [0₄/90₄]_s flat panel and a [0₆/90₃]_s curved panel near the loading area.

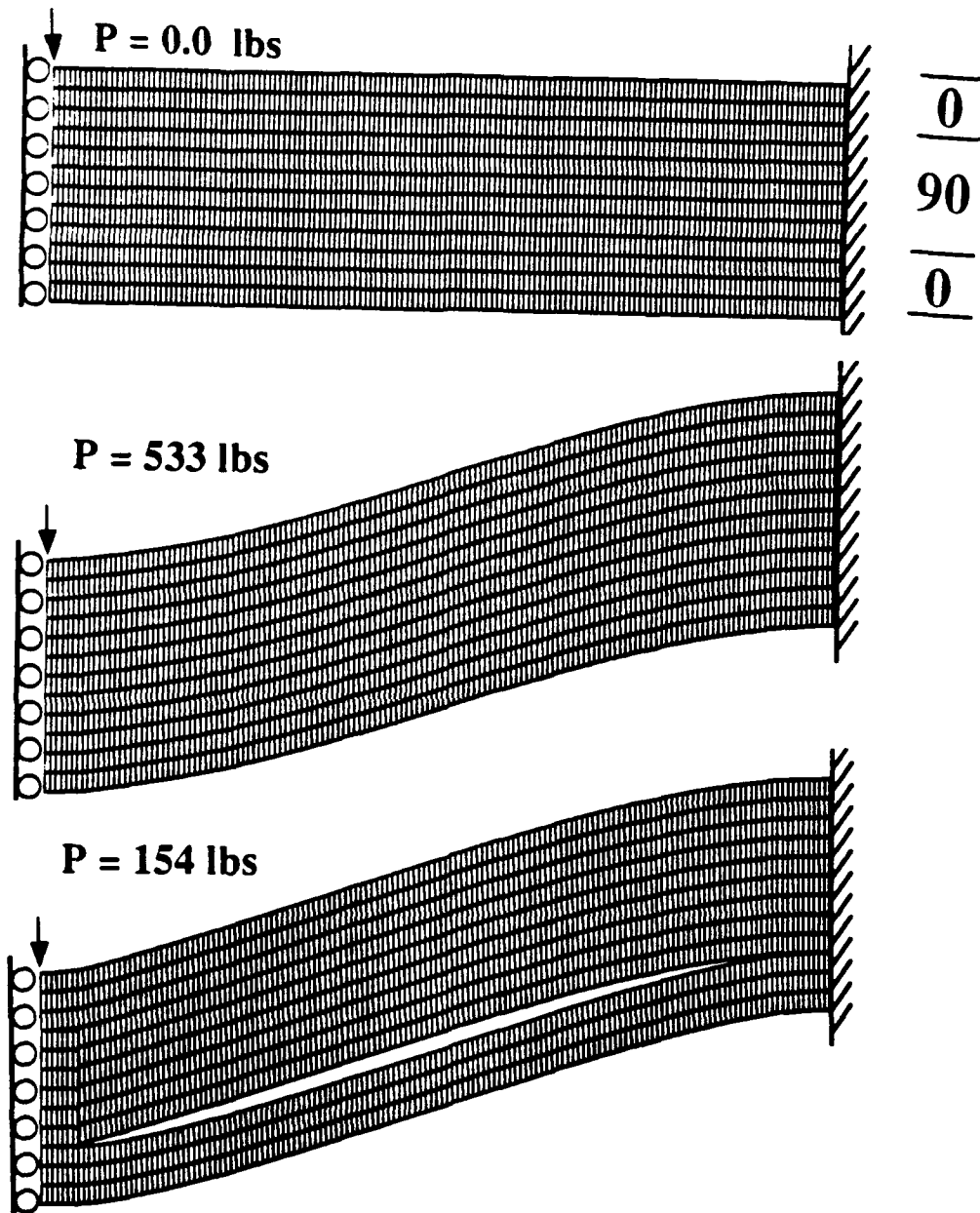
T300 976 $[0_4/90_4]_s$ 

Figure 3.16 Numerical simulations of the deformed configurations of a T300/976 $[0_4/90_4]_s$ composite beam subjected to a transverse concentrated line load at various loading stages.

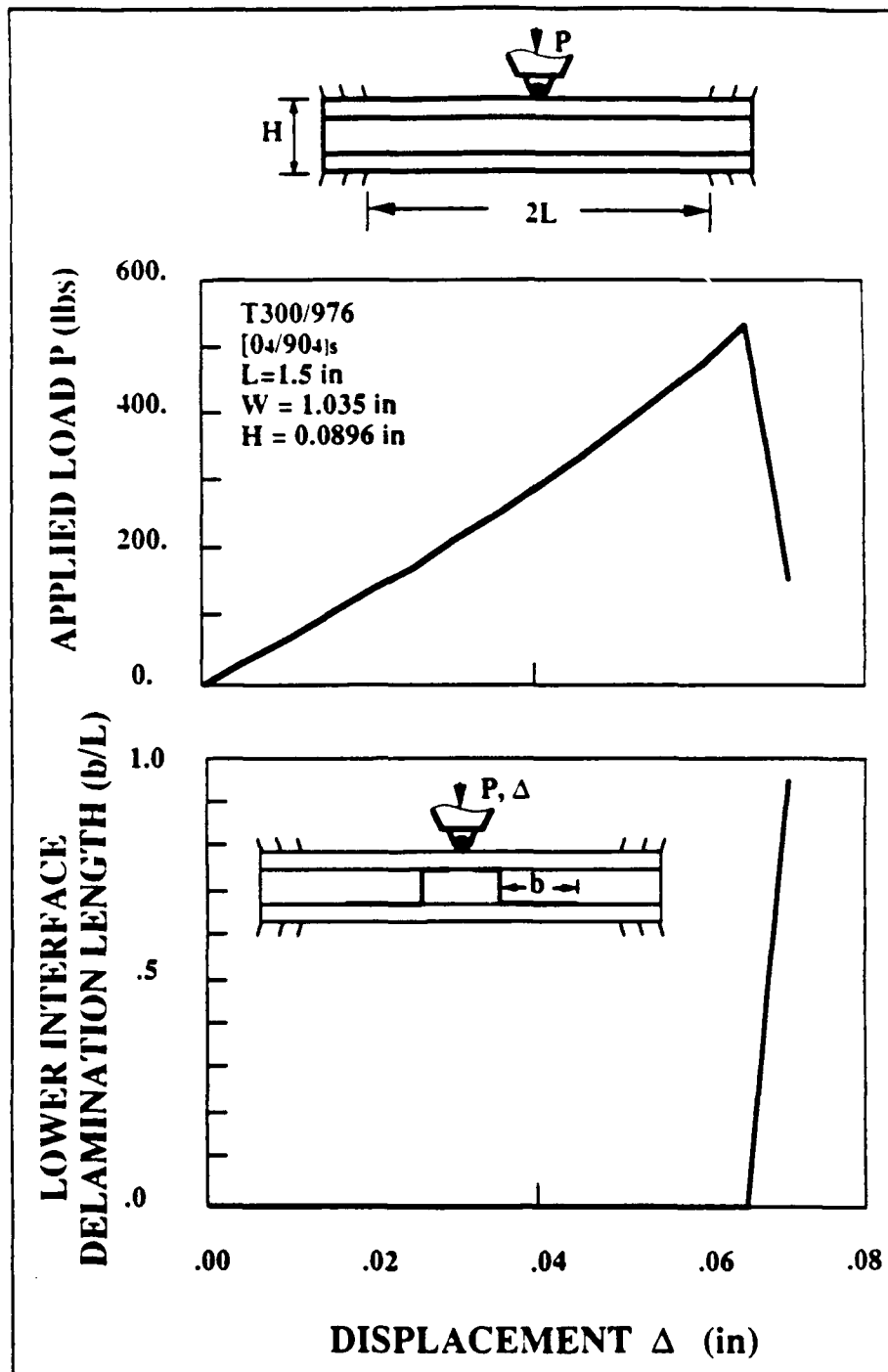


Figure 3.17 The calculated response of a T300/976 $[0_4/90_4]_s$ composite beam subjected to a transverse concentrated line load. (Above): The calculated applied load as a function of the load head displacement. (Below): The extent of the delamination induced by the matrix crack as a function of the load head displacement.

Table 3-4

Matrix crack locations and delamination extensions for curved panels.

 $(R = 2.86 \text{ in, } 2\alpha = 81^\circ)$

| Layups | α_c/α (model) | α_c/α (data) | α_d/α (model) | α_d/α (data) |
|----------------|---------------------------|--------------------------|---------------------------|--------------------------|
| $[0_6/90_3]_s$ | 5.3 | 8.57 | 42 | 50.5 |
| $[0_4/90_4]_s$ | 6 | 6.7 | 46.7 | 53.3 |

All the numbers in the table are in terms of percent. α_c is the half arc angle corresponding to the critical matrix crack location, α_d the half arc angle corresponding to the final delamination extension location, and α the half arc angle for the curved panel.

delamination at the lower interface delamination. Again, the delamination propagation was very unstable. The delamination immediately propagated away from the loading area and led to the collapse of the structure. It was calculated that the Mode II shear fracture dominated the delamination propagation in cylindrical panels. Accordingly, it seems that the strain energy release rate G_{IIC} is more critical in cylindrical panels than in flat panels for governing delamination propagation.

§3.5 Discussion

Based on the extensive analytical and experimental study, matrix cracking is seen to be the initial failure mode for the cross-ply laminates considered. Delamination was induced by these matrix cracks along the interfaces attached to the matrix cracks. For 90° plies on the bottom surface, a matrix crack could be produced due to excessive transverse tensile stresses in the 90° plies. These types of cracks are referred to as bending cracks. For the laminates containing 90° inner plies, matrix failure was due primarily due to transverse interlaminar shear stresses, which reached the maximum at the midplane of the laminate. This type of inner matrix cracking is referred to as a shear crack. The location of the shear cracks is always a distance away from the loading point, whereas the bending crack appears directly beneath the loading point.

Accordingly, depending upon the sequence of the ply orientation and the thickness of the laminate, either bending or shear cracks could occur, earlier than the other. For thick laminates, interlaminar shear stresses could dominate the stress field, leading to shear cracking. However, for thin laminates, bending cracks could appear earlier because of the bending deformation of the plate. The growth of the delamination induced by the shear cracks is apparently very unstable and catastrophic, whereas the bending crack induced delamination grows stably and progres-

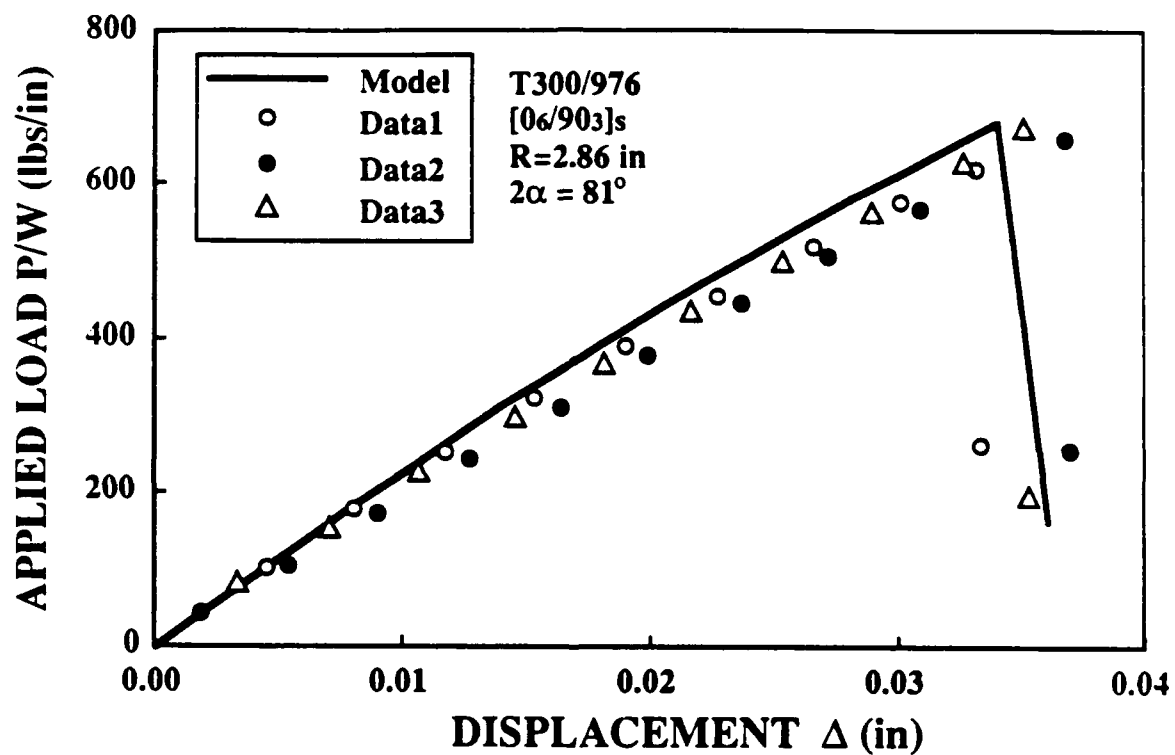


Figure 3.18 Comparison between the measured and the calculated load-strain relationship of a T300/976 [0₆/90₃]_s curved composite beam subjected to a concentrated line load.

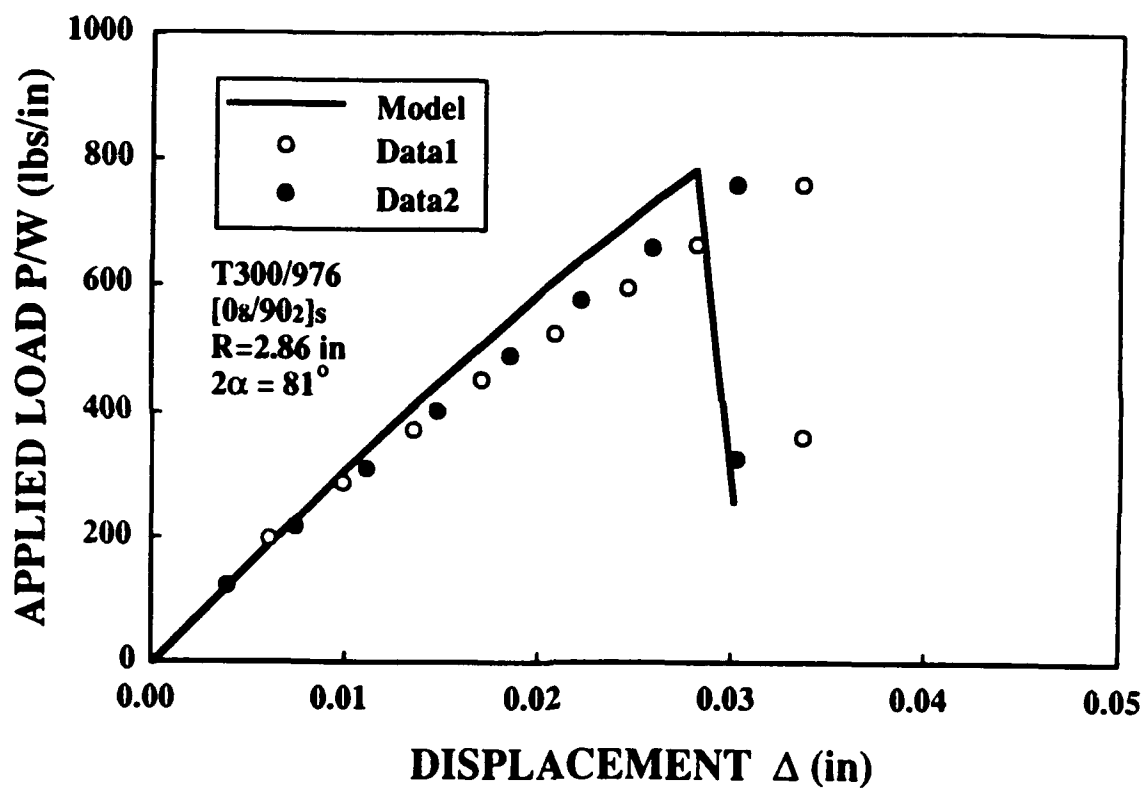


Figure 3.19 Comparison between the measured and the calculated load-strain relationship of a T300/976 [0₈/90₂]_s curved composite beam subjected to a concentrated line load.

T300/976, $[0_6/90_3]_s$, $R = 2.86$ in, $2\alpha = 81^\circ$

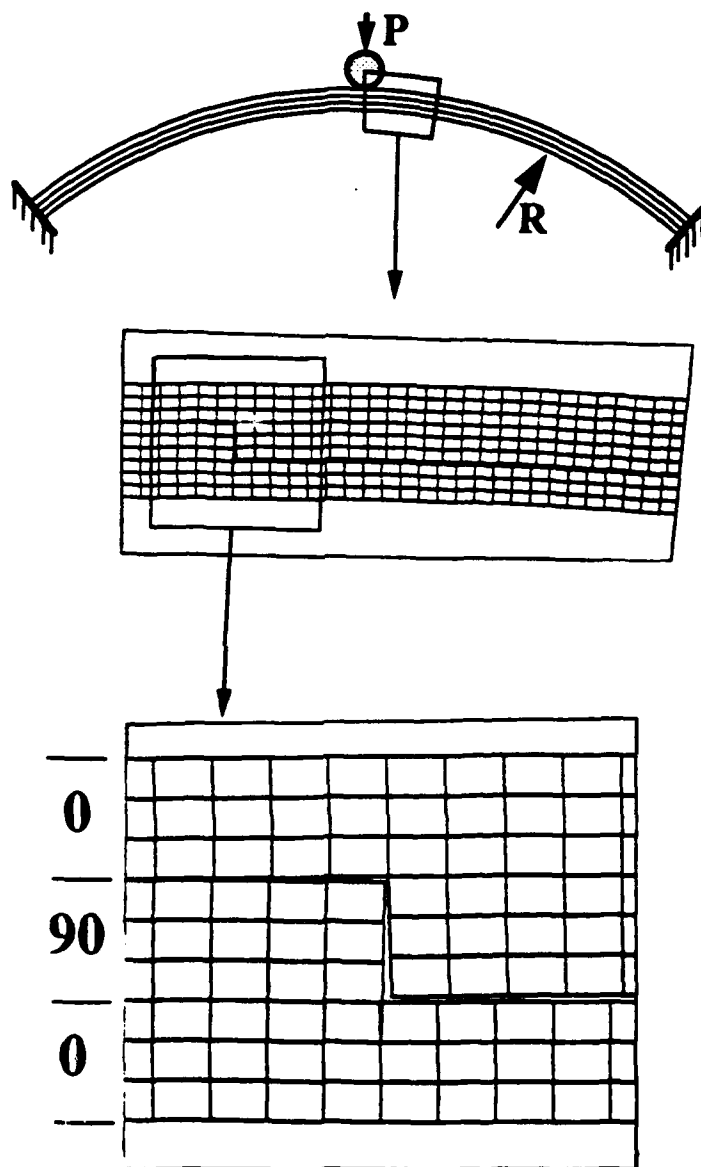


Figure 3.20 The calculated deformed configuration of a T300/976 $[0_6/90_3]_s$ curved composite beam corresponding to final failure load.

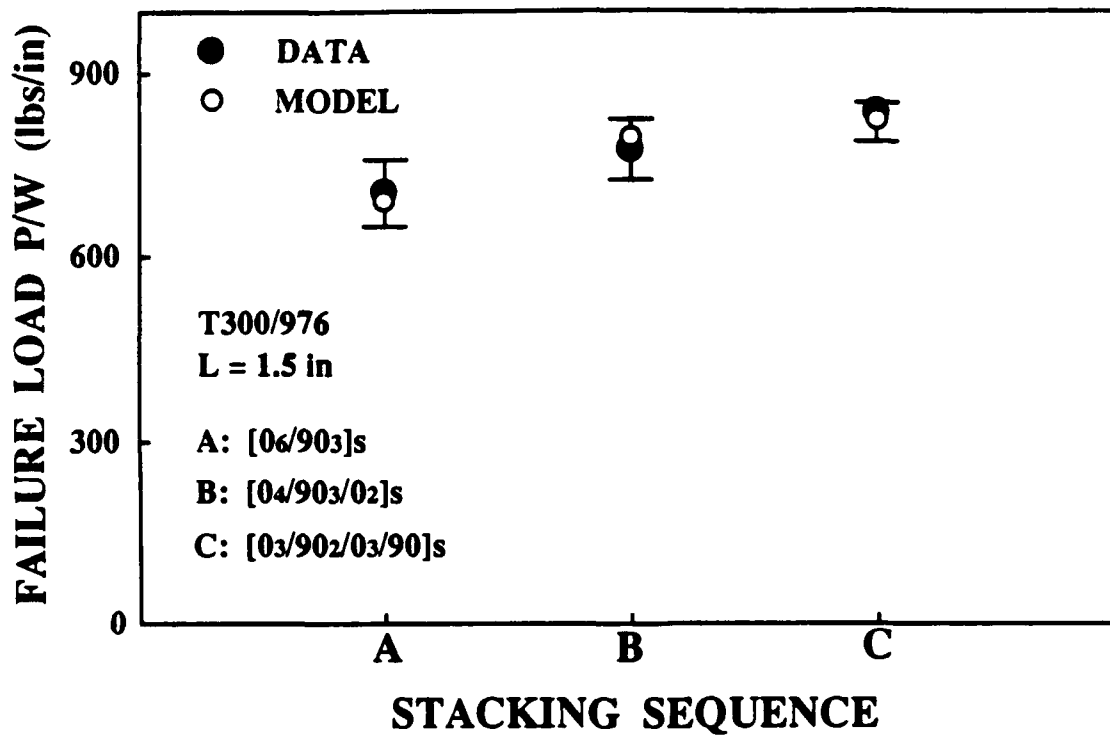


Figure 3.21 The failure load of laminated composite beams as a function of stacking sequence. Comparisons between the measurements and the predictions.

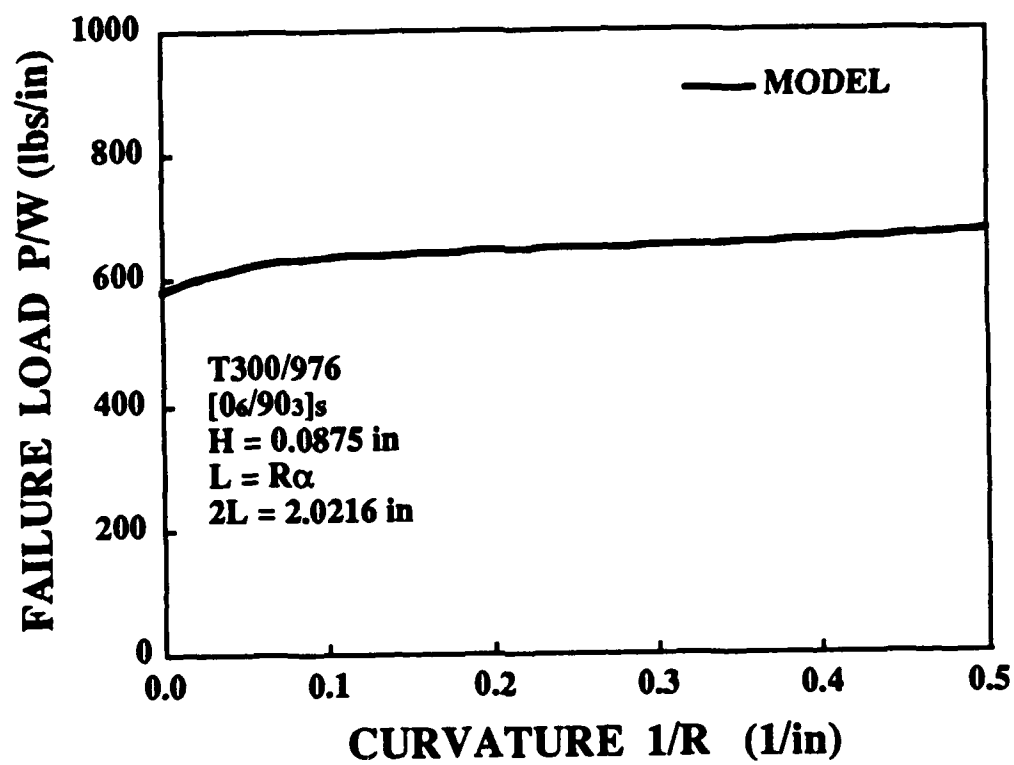


Figure 3.22 The predicted failure load of curved laminated beams as a function of curvature.

sively, and is proportional to the applied load. The calculations show that mixed mode fracture dominates the onset of the shear crack induced delamination growth while Mode I fracture dominates the onset of the bending crack induced delamination. Once the delamination propagates, Mode I fracture continues to control the growth of bending crack-induced delaminations, but Mode II fracture becomes increasingly important for the growth of the shear crack induced delaminations.

Apparently, the damage mode resulting from transverse concentrated line loads strongly depends on the ply orientation, but it is not sensitive to the change of curvature. However, the response and the extent of damage of the composites are sensitive to both ply orientation and geometry of the structures. For instance, Figure 3.21 shows the predicted initial failure load corresponding to the initiation of matrix cracking for different stacking sequences of flat laminates. Figure 3.22 shows the effect of curvature on the initial and final failure loads of cylindrical $[0_6/90_3]_s$ composite panels. Clearly, ply orientation influences the initial and final failure loads of the structures subjected to transversely concentrated loading.

§3.6 Concluding Remarks

In this study, a 2-D analytical model has been developed for simulating the response of laminated composites subjected to quasi-static transverse concentrated line loads. Experiments were also performed to verify the analysis. Based on the study, the following remarks can be made for the damage growth in cross-ply composites resulting from transverse concentrated line loads:

1. Intraply matrix cracking initiates the damage in laminated composites.
2. Intraply matrix cracking triggers delamination.
3. Delamination growth induced by intraply bending cracks is stable and progressive.

4. Delamination growth induced by intraply shear cracks is very unstable and catastrophic.
5. Mixed mode fracture dominates the onset of shear crack induced delamination while Mode I fracture dominates the onset of bending crack induced delamination.
6. The growth of the delamination induced by a bending crack is governed by Mode I fracture.
7. The growth of the delamination induced by shear cracks depends strongly on the G_{IIC} value.
8. Both stacking sequence and curvature affect the response and the extent of the damage in composites.

Chapter 4

Damage Induced by a Spherical Indenter

§4.1 Statement of Problem

The objective of this study was to fundamentally understand delamination propagation behavior and the effect of matrix cracking on its growth in cross-ply composites resulting from a transverse concentrated load. Therefore, only $[0_m/90_n]_s$ composite plates were considered. The rectangular plates could be simply supported or clamped on any one of the edges and subjected to a transverse quasi-static concentrated load by a spherical indenter.

In order to achieve the objective, the plates were assumed to contain a pre-existing small delamination located at the central loading area on the second 90/0 interface directly beneath the indenter. Two types of matrix cracking in conjunction with the delamination were considered in the study: a bending crack and a pair of shear cracks. Accordingly, for a given loading and boundary condition, four types of internal damage modes were studied: 1) delamination with no matrix cracks; 2) delamination induced by a bending crack; 3) delamination induced by shear cracks; and 4) delamination induced by both a bending crack and shear cracks, as shown in Figure 4.1.

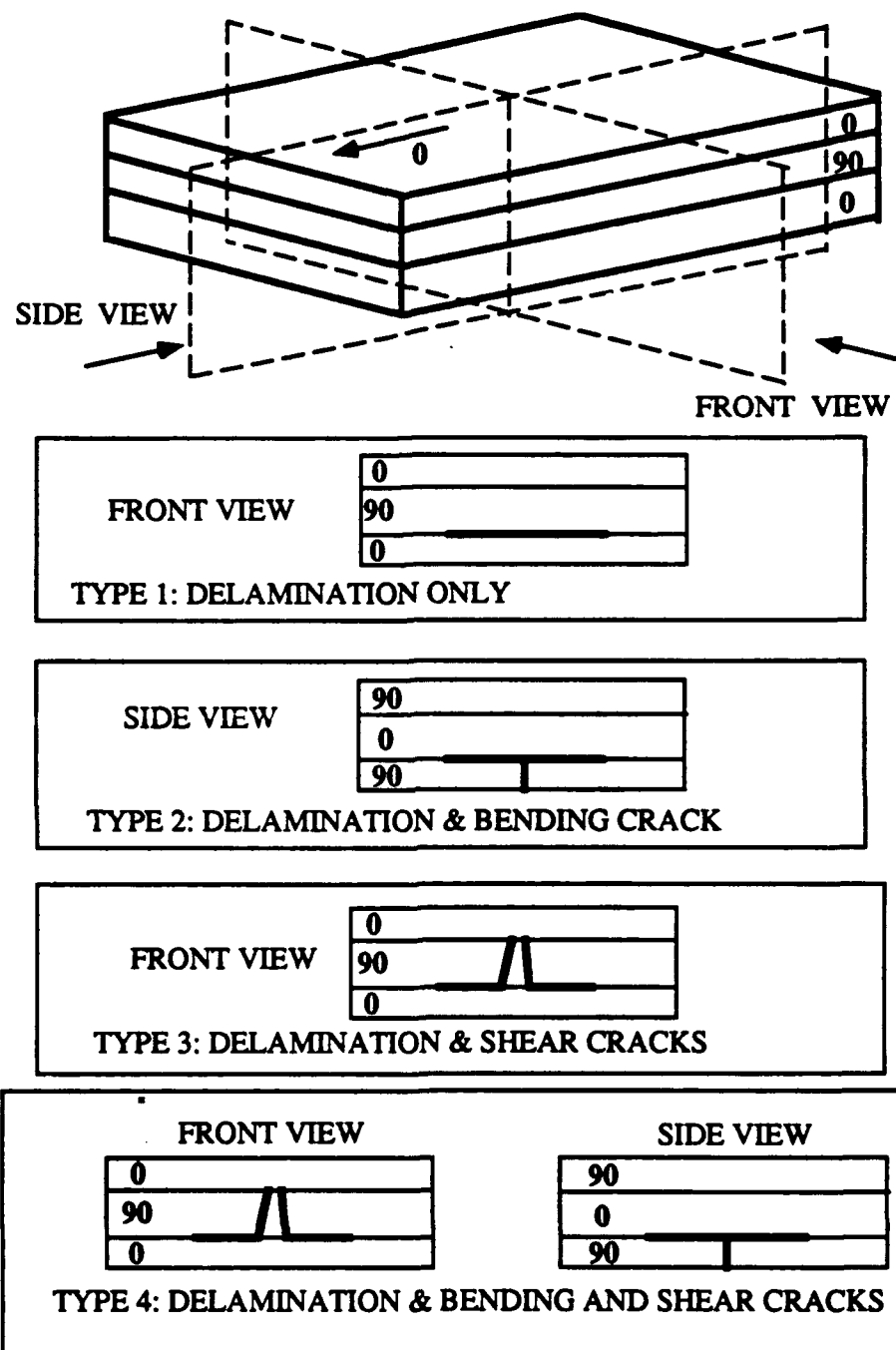


Figure 4.1 Four types of damage modes considered in this analysis: 1) delamination with no matrix cracks; 2) delamination induced by a bending crack; 3) delamination induced by shear cracks; and 4) delamination induced by both a bending crack and shear cracks.

§4.2 Analysis

The analytical model proposed for describing the behavior of laminated composite panels consists of three portions: a stress analysis, a contact analysis, and a failure analysis. The stress analysis is based on the large deformation theory similar to the one presented in Chapter 3, except that the displacement field is now three-dimensional. Therefore, the theory will not be elaborated in this chapter.

4.2.1 Contact Analysis

Two types of contact are involved: the rigid-elastic contact between the indenter and the plate, and the elastic-elastic contact between the cracked/delaminated interfaces, as shown in Figure 4.2. The local indentation resulting from a spherical indenter is very complicated and three-dimensional. The local indentation could significantly affect the delamination growth and its interface deformation, especially when the delamination is small. The actual contact between the spherical indenter and the laminate had to be simulated. For simplicity, only the elastic-elastic contact is presented in this section. The rigid-elastic contact can be treated as a special case of the elastic-elastic contact. The contributions of more than one contact pair can be easily handled as the formulation is general for contact between multiple bodies.

Several methods exist to implement the contact constraints. The most popular choices are the Lagrange multiplier method and the penalty method. The former has the advantage of enforcing the exact constraints, but induces additional parameters which cause an increase of the finite element matrix bandwidth and therefore substantially enlarge the overall size of the equation system to be solved [56]. This method was adopted for the study of damage induced by a cylindrical indenter for analyzing the interaction between matrix cracking and delamination. However, the

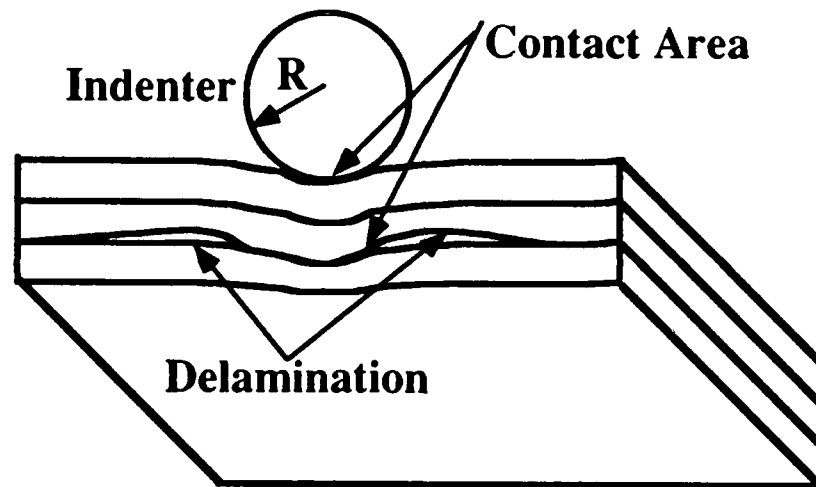


Figure 4.2 Contact problem associated with a delaminated laminate subjected to an indenter.

application of this method to three dimensions becomes extremely costly. Although the penalty method has the advantage of not requiring additional equations, it is very sensitive to the choice of a penalty parameter, which can possibly lead to ill-conditioning when the value of penalty parameter increases [56, 62, 66].

Therefore, in this study, an augmented Lagrangian method was adopted. It was originally proposed by Hestenes [57] and Powell [58] in studying mathematical programming problems subject to equality constraints. It has been shown to provide important advantages over the more traditional Lagrange multiplier and penalty methods. The applicability of this method to mathematical programming problems subject to inequality constraints is also well documented by Rockafellar [59] and others. Detailed mathematical discussions can be found in [56]. More recently, this technique has been successfully applied to various constrained mechanics problems such as incompressible finite deformation elasticity [60], and contact problems in two dimensions [61, 66]. The augmented Lagrangian techniques have been known to provide almost exact enforcement of constraints while using finite penalty parameters, avoiding the ill-conditioning.

Using the Lagrange multiplier technique, the total potential energy with the contact constraint conditions can be described as

$$\bar{\Pi} = \Pi + \int_{\Gamma} \lambda_N g d\Gamma \quad (4.1)$$

The variational equations of the laminate subjected to a spherical indenter, corresponding to the Lagrange multiplier formulation (similar to Eqs. (3.8)), can be described as

$$\left. \begin{aligned} \delta\Pi + \int_{\Gamma} \lambda_N \delta g d\Gamma &= 0, \\ \int_{\Gamma} \delta\lambda_N g d\Gamma &= 0 \end{aligned} \right\} \quad (4.2)$$

where λ_N is unknown, which needs to be solved from the above equation. The

introduction of the Lagrange multiplier λ_N could considerably enlarge the system of equations.

However, the penalty treatment is achieved by the replacement of λ_N in Eqs. (4.2) by $\epsilon_N g$, where ϵ_N is defined as the penalty parameter. It can be observed that as $\epsilon_N \rightarrow \infty$, $g \rightarrow 0$ and λ_N is bounded. However, as $\epsilon_N \rightarrow \infty$, the gap g must be zero, which satisfies the constraint condition.

The variational equation for the penalty method can now be written as

$$\delta\Pi + \int_{\Gamma} \epsilon_N g \delta g \, d\Gamma = 0 \quad (4.3)$$

It is noted that Eq. (4.3) only involves the displacement variables, and no additional contact force constraint is needed. As a result, Eq. (4.3) does not introduce additional equations and is extremely attractive for finite element implementations. However, the constraint condition $g \geq 0$ is only satisfied when ϵ_N approaches infinity, which unfortunately leads to ill-conditioning. In order to solve Eq. (4.3), ϵ_N is chosen as a large finite constant in practice without inducing ill-conditioning. Therefore, some overlapping between contact surfaces may occur. In the present delamination contact problem, the overlapping between the contact surfaces needed to be minimized. These considerations led to the development of the method of augmented Lagrangians.

In the method of augmented Lagrangians, the λ_N is initially chosen to be an arbitrary constant. If this constant is not the correct Lagrange multiplier, the contact constraint is not satisfied and minimization of the total potential energy of Eq. (4.1) does not lead to the equation of equilibrium. Therefore, from a penalty function viewpoint, the total potential energy represented by Eq. (4.1) needs to be further penalized by the following modified functional:

$$\bar{\Pi} = \Pi + \int_{\Gamma} \lambda_N^{(k)} g \, d\Gamma + \int_{\Gamma} \frac{1}{2} \epsilon_N g^2 \, d\Gamma \quad (4.4)$$

where $\lambda_N^{(k)} \leq 0$ denotes the fixed estimate of the correct λ_N . The superscript k indicates that the search for the correct λ_N is an iterative process. The updated formula is

$$\lambda_N^{(k+1)} = (\lambda_N^{(k)} + \epsilon_N g) \quad (4.5)$$

Therefore, the variational equation corresponding to Eq. (4.4) can be derived as

$$\delta\Pi + \int_{\Gamma} (\lambda_N^{(k)} + \epsilon_N g) \delta g \, d\Gamma = 0 \quad (4.6)$$

It is noted that the term $(\lambda_N^{(k)} + \epsilon_N g)$ plays the role of the Lagrange multiplier λ_N . If λ_N is the correct multiplier, then $g = 0$ on Γ . Thus, in the case where the multipliers are correct, Eq. (4.6) achieves exactly the same form as the first of Eqs. (4.2), making it an exact penalization.

It is important to notice that Eq. (4.6) is a nonlinear equation due to the contact conditions and geometric nonlinearity. In general, then, it will be necessary to solve Eq. (4.6) in an iterative manner. In practice, ϵ_N is chosen to be as large as practically possible without inducing ill-conditioning. The advantage of the current treatment over the penalty method is that satisfaction of the constraints can be improved even if ϵ_N is of relatively modest value through repeated application of the augmentation procedure. Since these augmentations only change $\lambda_N^{(k)}$, which is fixed with regard to solution of Eq. (4.6), the ill-conditioning problem usually associated with the penalty method is mediated or eliminated.

4.2.2 Failure Analysis

The initiation of delamination growth (onset of delamination growth) was predicted based on linear elastic fracture mechanics. The well-known virtual crack closure technique [52] served as the basis for the strain-energy release rate calculation. This procedure determines Mode I, Mode II, and Mode III strain energy release rates from the energy required to close the delamination over a small area. The strain energy release rates G_I , G_{II} , and G_{III} for Mode I, Mode II, and Mode III fracture respectively, can be expressed as [75]

$$G_I = \lim_{\Delta A \rightarrow 0} \left\{ \frac{1}{2\Delta A} \int_0^{\Delta A} [u_n^+(A + \Delta A) - u_n^-(A + \Delta A)] \sigma_{nn} dA \right\} \quad (4.7.a)$$

$$G_{II} = \lim_{\Delta A \rightarrow 0} \left\{ \frac{1}{2\Delta A} \int_0^{\Delta A} [u_s^+(A + \Delta A) - u_s^-(A + \Delta A)] \sigma_{sn} dA \right\} \quad (4.7.b)$$

$$G_{III} = \lim_{\Delta A \rightarrow 0} \left\{ \frac{1}{2\Delta A} \int_0^{\Delta A} [u_t^+(A + \Delta A) - u_t^-(A + \Delta A)] \sigma_{tn} dA \right\} \quad (4.7.c)$$

where ΔA is the crack extension area; n, s, t form a local coordinate system which are out-of-plane normal, in-plane normal, and in-plane tangent respectively; σ_{nn} , σ_{sn} , and σ_{tn} are the stresses at the crack front associated with a crack size of A ; and u_n^+ , u_s^+ , u_t^+ and u_n^- , u_s^- , u_t^- are the displacements of the upper and lower surfaces of the crack associated with a crack size of $A + \Delta A$ respectively.

Therefore, at any point on the delamination front, strain energy release rates can be calculated. Since the delamination growth can be attributed to a mixed mode fracture, the criterion for determining the initiation of the delamination growth was selected as [75–78]

$$\left(\frac{G_I}{G_{Ic}} \right)^\alpha + \left(\frac{G_{II}}{G_{IIc}} \right)^\beta + \left(\frac{G_{III}}{G_{IIIc}} \right)^\gamma = E_d \quad (4.8)$$

for any point on the delamination front. Here, G_{Ic} , G_{IIc} , and G_{IIIc} are the critical strain energy release rates corresponding to Mode I, Mode II, and Mode III

fracture, respectively. It was assumed that G_{IC} , G_{IIC} , and G_{IIIC} did not change with delamination size. Based on the two-dimensional study in this thesis and [42], $\alpha = 1$, $\beta = 1$, and $\gamma = 1$ were selected for this study, because they were found to provide the best fit to the experiments in two dimensions. It was assumed that $G_{IIIC} = G_{IIC}$ [67], because the value of G_{III} has not been reported in the literature. Accordingly, delamination would start to propagate when $E_d \geq 1$ at any point on the delamination front.

§4.3 Finite Element Implementation of the Formulation

The laminate was discretized by 8-node isoparametric brick elements into n_{el} element domains with n_{np} nodal points.

The displacement field within an element was assumed to be in the form

$$u = \sum_{a=1}^{n_{en}} N_a u_a \quad (4.9)$$

where N_a is the displacement shape (interpolation) function associated with the local nodal number a , and u_a is the nodal displacement vector at node number A . The displacement shape functions N_a in the local coordinates p , q , and r have the following expression:

$$N_a(p, q, r) = \frac{1}{8} (1 + pp_a) (1 + qq_a) (1 + rr_a) \quad (4.10)$$

where $a = 1 - 8$ and there is no summation on a .

Both the indenter and the laminate were discretized by finite numbers of elements, and the master-slave definition is the same as given in the 2-D study. The indenter was treated as the master surface while the top of the laminate was treated as the slave surface. For delamination surfaces, both upper and lower surfaces may be treated as slave and master surfaces. It was again assumed that the contact pres-

sure on each master element was constant. Therefore, Eq. (3.21) and its associated arguments still applied.

4.3.1 Variational Formulation of the Discrete Problem

The finite element formulation employs the modified total potential energy (Eq. (4.4)) in its discrete form. Therefore, the following functional is obtained

$$\bar{\Pi}(\mathbf{u}) = \Pi(\mathbf{u}) + \lambda^T \mathbf{g} + \frac{1}{2} \epsilon \mathbf{g}^T \mathbf{g} \quad (4.11)$$

where the components of vector λ are assumed to be a fixed estimate of the correct Lagrange multiplier vector and need to be updated following the formula of Eq. (4.5) in a vector form. The focus here is on the contribution of the contact constraints due to cracked/delaminated interfaces. The discrete form of the virtual work principle can be derived from Eq. (4.4) and has the following form:

$$\left(\frac{\partial \Pi}{\partial \mathbf{u}} + \mathbf{t}^T \frac{\partial \mathbf{g}}{\partial \mathbf{u}} \right) \delta \mathbf{u} = 0 \quad (4.12)$$

imagined as the approximate contact force vector. The \mathbf{t} will be the correct contact force vector if the gap vector \mathbf{g} is essentially zero. It is reiterated that λ is a constant vector in the solution of Eq. (4.12). Therefore, the nonlinear equilibrium equations for the discrete system can be obtained as

$$\frac{\partial \Pi}{\partial \mathbf{u}} + \mathbf{t}^T \frac{\partial \mathbf{g}}{\partial \mathbf{u}} = 0 \quad (4.13)$$

In the framework of the finite element method, the term $\frac{\partial \Pi}{\partial \mathbf{u}}$ can be replaced by $\mathbf{P}_{\text{int}} - \mathbf{R}_{\text{ext}}$, defined in the same way as in the 2-D study. The term $\mathbf{t}^T \frac{\partial \mathbf{g}}{\partial \mathbf{u}}$ can be replaced by \mathbf{F}_c , which is a contact force vector. Therefore the following equation is obtained:

$$\mathbf{P}_{\text{int}} + \mathbf{F}_c = \mathbf{R}_{\text{ext}} \quad (4.14)$$

The equation represents a weak form of the equilibrium equation in the framework of Lagrangian augmentation technique. It is shown that \mathbf{t} represents the vector of contact forces, which are distributed according to the matrix $\frac{\partial \mathbf{g}}{\partial \mathbf{u}}$ to the associated nodes of the contact element.

In general, due to the finite deformation and the contact constraints, the system of equations is nonlinear and therefore needs to be solved iteratively by the Newton-Raphson method [70–74]. By applying the Newton-Raphson technique, the following linearized equation is obtained:

$$\frac{\partial}{\partial \mathbf{u}} [\mathbf{P}_{\text{int}} + \mathbf{F}_c] d\mathbf{u} = \mathbf{R}_{\text{ext}} - (\mathbf{P}_{\text{int}} + \mathbf{F}_c) \quad (4.15)$$

Recalling that \mathbf{P}_{int} and \mathbf{F}_c are the function of \mathbf{u} only, the above equation can be written as

$$\left[\frac{\partial}{\partial \mathbf{u}} (\mathbf{P}_{\text{int}}) + \frac{\partial}{\partial \mathbf{u}} (\mathbf{F}_c) \right] d\mathbf{u} = \mathbf{R}_{\text{ext}} - (\mathbf{P}_{\text{int}} + \mathbf{F}_c) \quad (4.16)$$

Or

$$(\mathbf{K} + \mathbf{K}_c) d\mathbf{u} = \mathbf{R}_{\text{ext}} - (\mathbf{P}_{\text{int}} + \mathbf{F}_c) \quad (4.17)$$

where $\mathbf{K} (= \frac{\partial}{\partial \mathbf{u}} (\mathbf{P}_{\text{int}}))$ is the classical tangent stiffness matrix which can be obtained without considering the contact constraint conditions. \mathbf{F}_c is the contact residual force vector and defined as

$$\mathbf{F}_c = \mathbf{t} \frac{\partial \mathbf{g}}{\partial \mathbf{u}} \quad (4.18)$$

and \mathbf{K}_c is the contribution of the contact conditions to the tangent stiffness matrix, which guarantees the best approximation to the actual response. It is defined as

$$\mathbf{K}_c = \frac{\partial \mathbf{F}_c}{\partial \mathbf{u}} \quad (4.19)$$

For convenience, the above matrices will be derived on the basis of an element coming in contact with one node on the other body, forming one contact element. Such an element provides one gap g and one estimated contact force magnitude t , and has N nodal points. Subsequently, capital letter indices (N and M) are used here to identify quantities which are related to the element nodal points. Moreover, for repeated indices the summation convention of tensor calculus holds. The contact residual force of an element is

$$\mathbf{f}_c = t \frac{\partial g}{\partial \mathbf{u}^M} \quad (4.20)$$

where $t = \lambda + \epsilon g$ and λ is a constant Lagrange multiplier in some step. The stiffness contribution due to contact has the following form

$$\mathbf{k}_c = \frac{\partial \mathbf{f}_c}{\partial \mathbf{u}^N} = \frac{\partial}{\partial \mathbf{u}^N} [t \frac{\partial g}{\partial \mathbf{u}^M}] = \frac{\partial}{\partial \mathbf{u}^N} [(\lambda + \epsilon g) \frac{\partial g}{\partial \mathbf{u}^M}] \quad (4.21)$$

or

$$\mathbf{k}_c = \frac{\partial}{\partial \mathbf{u}^N} (\lambda + \epsilon g) \frac{\partial g}{\partial \mathbf{u}^M} + (\lambda + \epsilon g) \frac{\partial}{\partial \mathbf{u}^N} \left(\frac{\partial g}{\partial \mathbf{u}^M} \right) \quad (4.22)$$

or

$$\mathbf{k}_c = \epsilon \frac{\partial g}{\partial \mathbf{u}^N} \frac{\partial g}{\partial \mathbf{u}^M} + t \frac{\partial}{\partial \mathbf{u}^N} \left(\frac{\partial g}{\partial \mathbf{u}^M} \right) \quad (4.23)$$

The corresponding form of Eq. (4.16) for one contact element is

$$\left\{ \frac{\partial \mathbf{P}_{\text{int}}^M}{\partial \mathbf{u}^N} + \epsilon \frac{\partial g}{\partial \mathbf{u}^N} \frac{\partial g}{\partial \mathbf{u}^M} + t \frac{\partial}{\partial \mathbf{u}^N} \left(\frac{\partial g}{\partial \mathbf{u}^M} \right) \right\} d\mathbf{u}^N = \mathbf{R}_{\text{ext}}^M - (\mathbf{P}_{\text{int}}^M + \mathbf{F}_c^M) \quad (4.24)$$

The three terms in parentheses form the tangent stiffness matrix of the element. The first term is the classical tangent stiffness matrix for undamaged composites. The derivation of the matrix is available in the literature related to finite element methods [70-74].

The derivation of the contact element stiffness matrix k_c is important, as it renders the quadratic convergence of Newton's method. The derivation of the contact stiffness matrix k_c and the residual force f_c are described in Appendix D.

4.3.2 Mesh Generation

It has been observed experimentally that delaminations in cross-ply composites due to low-velocity impact or quasi-static indentation loading form ellipsis-like or peanut-like shapes. Therefore, only delaminations with circular or elliptical shapes were considered in the analysis, as shown in Figure 4.3, Figure 4.4, Figure 4.5, and Figure 4.6.

This section describes the technique used for the finite element mesh generation for the proposed problems. The procedure used for generating the meshes was similar to the one given by Whitcomb [68]. The meshes by Whitcomb were used only for modeling a delamination in a square laminate without including matrix cracking. The present meshes work for a rectangular laminate containing a delamination in conjunction with matrix cracks. The procedure of constructing a typical mesh is described as follows.

It was assumed that the length of the plate is greater than or equal to its width. First, a two-dimensional mesh was formed in $Y - Z$ plane, where the delamination is represented by a line of size b . Here, b is the size of the short axis of the elliptical delamination. Secondly, this two-dimensional mesh was swept through the space by a 90° arc around the Z axis to generate a $1/4$ cylindrical 3-D mesh. Here, a circular delamination of radius b was obtained in this cylindrical mesh. The radial lines were normal to the circumferential lines. Third, the outer part (it can be more than one surface) was then transformed to obtain a square boundary. The fourth step was that the inner circle was replaced by a block consisting of brick

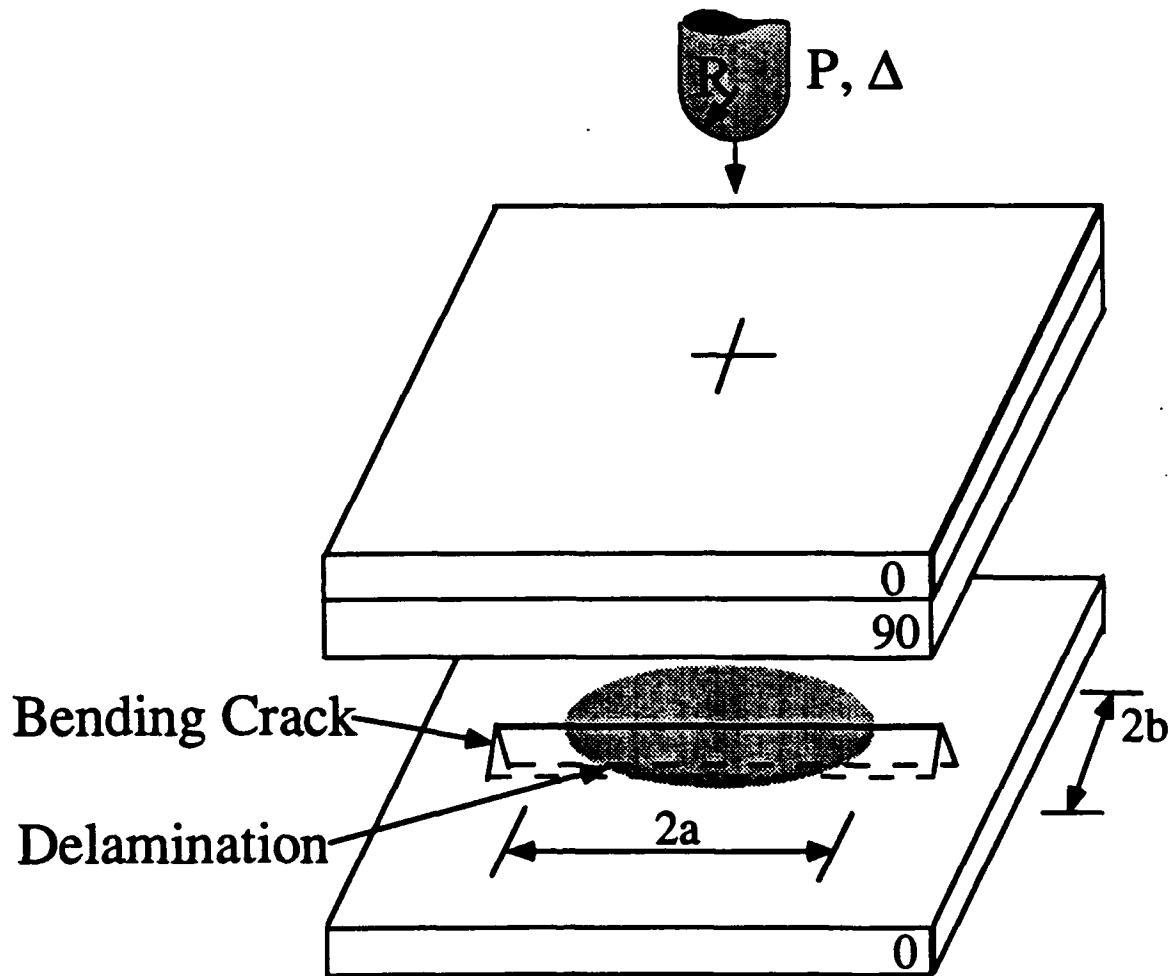


Figure 4.3 A delaminated cross-ply composite with or without a surface matrix crack and subjected to a transverse load from a spherical indenter.

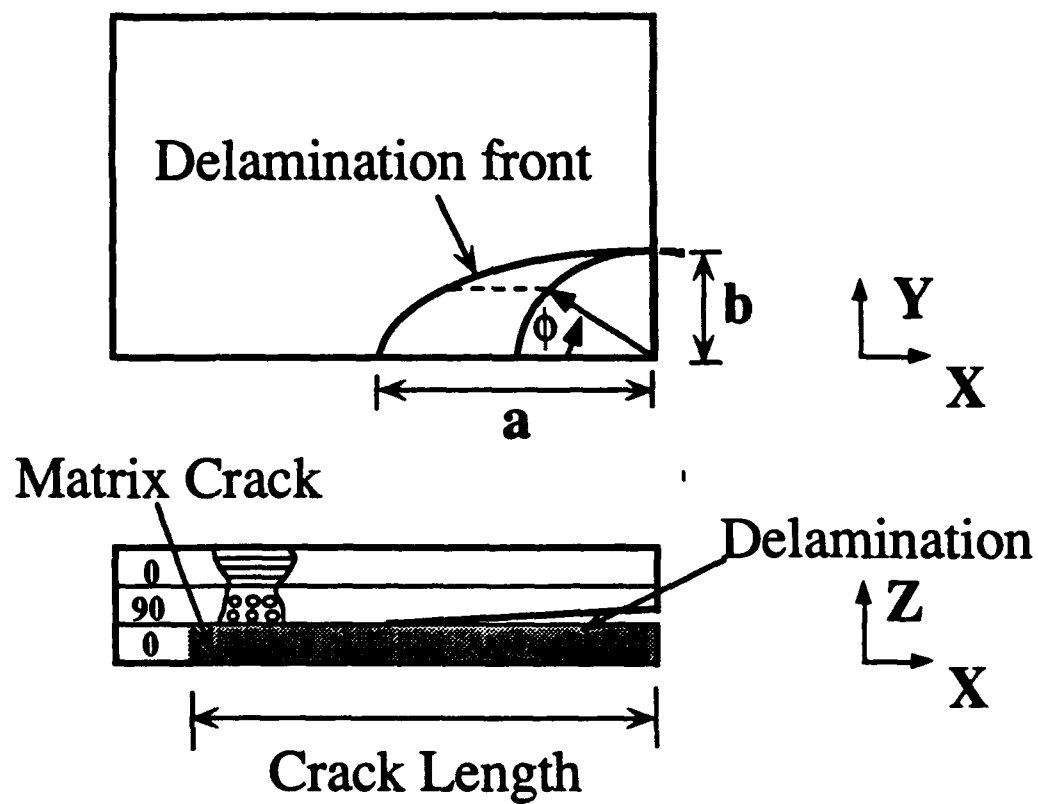


Figure 4.4 The coordinate system used in the finite element analysis for a laminate containing a delamination and a bending crack.

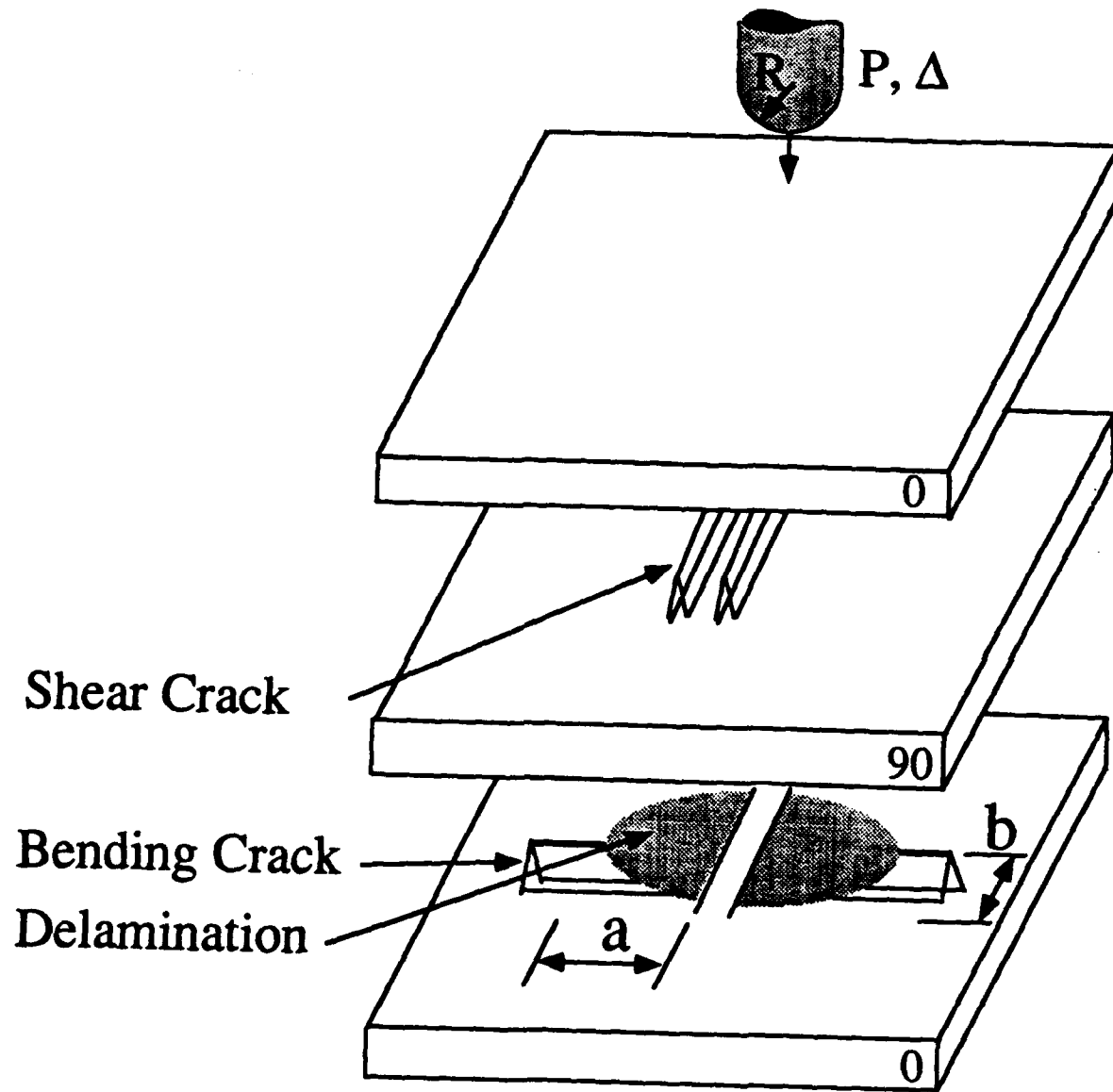


Figure 4.5 A delaminated cross-ply composite containing a pair of internal shear cracks with or without a surface bending crack and subjected to a transverse load from a spherical indenter.

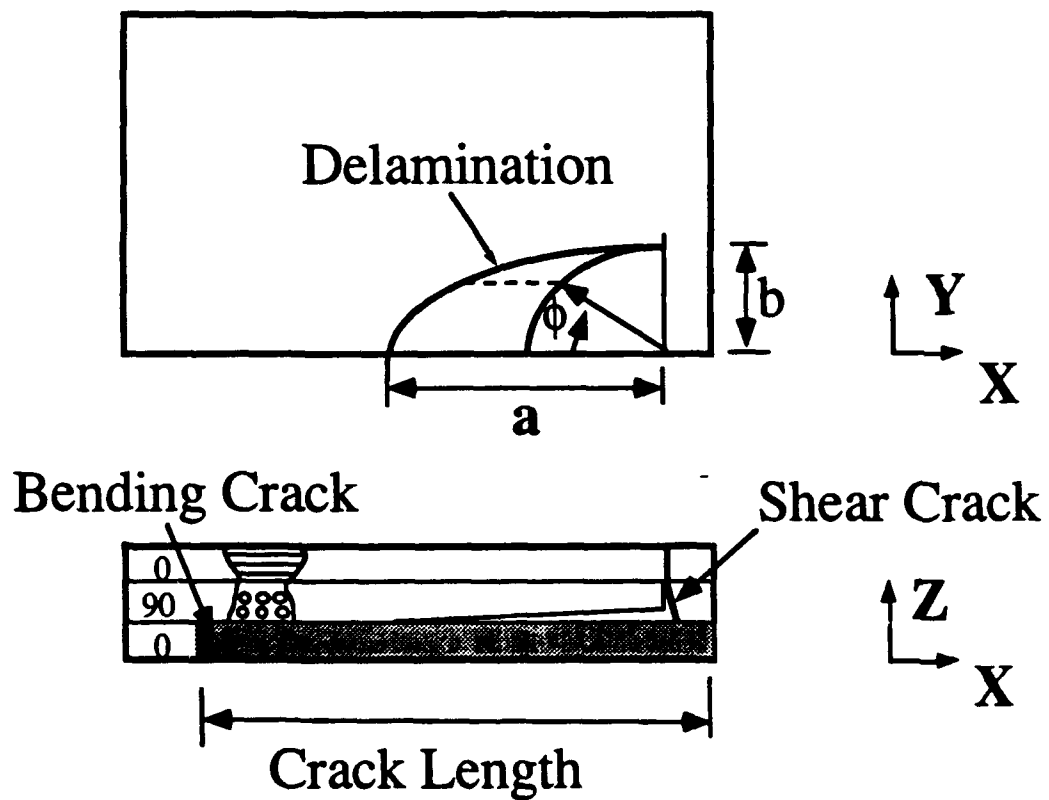


Figure 4.6 The coordinate system used in the finite element analysis for a laminate containing a pair of shear cracks and one delamination having two semi-circular or semi-elliptical shapes offset by the internal cracks.

elements so that only brick elements needed to be used. The fifth step was to apply a modified elliptical transformation to obtain an elliptical delamination front, while keeping good spacing for elements near the center. Based on the standard elliptical transformation, a scale factor was introduced for "stretching" the mesh, for example, in longitudinal or width (X) direction:

$$X' = X \left(\sqrt{1 + \frac{a^2 - b^2}{X^2 + Y^2}} F - F + 1 \right) \quad (4.25)$$

where

$$F = \frac{\sqrt{X^2 + Y^2}}{r}, \text{ for } r \geq \sqrt{X^2 + Y^2} \quad (4.26)$$

and

$$F = 1, \text{ for } r \leq \sqrt{X^2 + Y^2} \quad (4.27)$$

The mesh can be similarly "stretched" in Y direction if $b \geq a$. It is easy to show that when $F = 1$, the transformation is the standard elliptical (conformal) mapping. In the conformal mapping, any two lines which were orthogonal would be kept orthogonal after the mapping. When $F \leq 1$ the mapping is a modified elliptical mapping, which can produce a more evenly distributed mesh for the mesh within a circle of radius of r . By choosing the parameter r a little less than the radius of the delamination front in the cylindrical mesh, the orthogonality was well maintained in the neighborhood of the delamination front in the elliptical transformation. By maintaining orthogonality, the calculation of fracture mechanics quantities such as energy release rates can be greatly simplified.

For modeling the surface crack, it was assumed that the nodes on the crack surface were free to move and had independent degrees of freedom. Due to symmetry, only 1/4 laminate was modeled and therefore only one shear crack needed to be modeled. In meshing the plate with a shear crack, the laminate was divided into

two blocks, the delaminated block and the solid block, separated by the shear crack surfaces. The mesh of the delaminated block away from the indenter was formed first, by the procedure described above. Then, the mesh of the solid block which was below or near the indenter was generated and attached to the mesh of the first block. The nodes on both sides of the shear crack were assumed to move freely. A typical mesh used for the analysis proposed is shown in Figure 4.7.

4.3.3 Contact Node Search

The general approach to contact in the literature is the slave-master method. That is, one side of the contact surface is designated as the master surface while the other is treated as the slave surface. In the finite element method, this practice is referred to as one-pass and obviously lacks symmetry. In the current delamination problem where corners and edges exist, and where complicated curvature also exists during deformation, the lack of symmetry can produce slow convergence or divergence and incorrect solutions. The remedy may be easily achieved by periodically reversing the designation of the master and slave surfaces. A more sophisticated approach is adopted here which makes two passes at every time step with each surface being the master surface on one pass [64]. Taking two passes each load step doubles the cost of the algorithm. However for many practical problems, a symmetric algorithm is much more robust than a conventional unsymmetric algorithm, making it well worth the additional cost.

In the two-dimensional study of this thesis, a structured finite element mesh was used, which required less bookkeeping in terms of the contact search. However, in the current three-dimensional study, an unstructured finite element mesh was used. It was very challenging to find an economical search algorithm.

In a finite element setting, given the slave node, the problem remaining is to

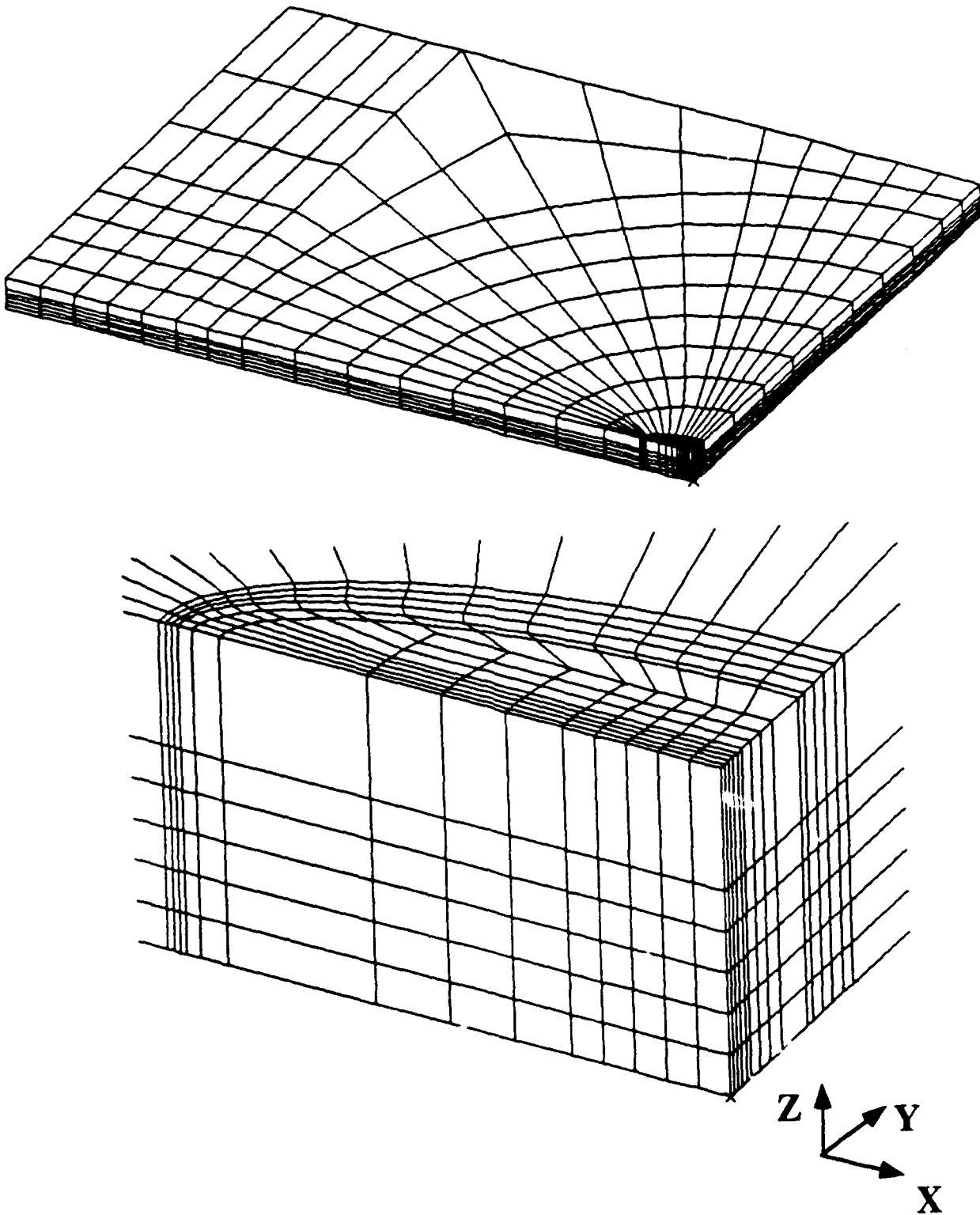


Figure 4.7 Description of a typical finite element mesh used in the analysis.

search for the closest projection onto the master surface. There are three steps to take for the search. The first step is to determine which master node is closest to the slave node. The second step is to determine which of the master segments, having the master node as one of their vertices, is closest to the slave node. The third step is to determine the closest point of the master segment to the slave node in terms of ξ and η in the isoparametric biunit domain. For each slave node, one contact point can be located. Therefore, the gap g can be determined. Due to the complexity of the contact search process, the details of these steps are deferred to Appendix C.

4.3.4 Numerical Implementation of the Failure Model

The delamination growth model was implemented into a finite element analysis. The modified crack closure technique [52] served as the basis for the strain energy release rate calculation. The physical interpretation of the crack closure technique is that the amount of work required to close the crack by a short distance determines the energy release rates G_I , G_{II} , and G_{III} . The crack closure energy involves products of forces and displacements of elements along the delamination front.

The energy release rate calculation is illustrated for an 8-node brick element in Figure 4.8 which shows a schematic of the delamination front region. The nodes of interest for the energy release rate calculations are indicated by the solid circles. In the finite element mesh, it is advantageous to use a more regular mesh near the delamination front so that a single solution method can be used [52].

In calculating the crack closure work, it was necessary to calculate the forces transmitted at the crack tip as well as the crack front relative displacements. The forces were evaluated by summing up all the nodal forces for all the elements which were connected to the nodes on the front and whose centroids lay above the delamination plane.

Energy release rate is a measure of the energy per unit area. Hence, the work must be normalized by the appropriate areas. Unfortunately, there is no simple or exact way to determine the appropriate areas. Certain approximations must be made. It was assumed that, for the linear elements, the work associated with the elements attached to line BE (see Figure 4.8) was proportional to their respective areas. For radial line BE , the area associated with it was estimated as follows:

$$\Delta A = \frac{1}{2}(A_1 + A_2) \quad (4.28)$$

where the physical interpretation was that the weights for the work produced by

each element were proportional to its area.

As the delamination front in general was not parallel to one of the global coordinate axes, a local orthogonal coordinate system was defined in which the forces and relative displacements could be evaluated in terms of the local coordinates (n, s, t , see Figure 4.8). The local coordinate system had one axis tangent to the delamination front, one axis normal to the delamination front, and one axis normal to the delamination plane. The transformed nodal force vector in the local system can be evaluated as

$$\mathbf{F}'_i = \mathbf{T}_{ij} \mathbf{F}_j \quad (4.29)$$

where T is the transformation matrix of rank 3×3 from the global coordinate system to local coordinate system. And the components of T are directional cosines of θ (shown in Figure 4.8).

Therefore, the energy release rates for Modes I, II, and III can be calculated in one step:

$$G_I = \lim_{\Delta A \rightarrow 0} \left\{ \frac{1}{2\Delta A} F'_{nB} (u_{nQ} - u_{nP}) \right\} \quad (4.30.a)$$

$$G_{II} = \lim_{\Delta A \rightarrow 0} \left\{ \frac{1}{2\Delta A} F'_{sB} (u_{sQ} - u_{sP}) \right\} \quad (4.30.b)$$

$$G_{III} = \lim_{\Delta A \rightarrow 0} \left\{ \frac{1}{2\Delta A} F'_{tB} (u_{tQ} - u_{tP}) \right\} \quad (4.30.c)$$

Once the energy release rates were calculated, the delamination growth criterion was applied for each point on the delamination front. In order to predict the delamination growth, the three-dimensional crack growth criterion (Eq. (4.8)) was used. If $E_d \geq 1$, then delamination growth was predicted.

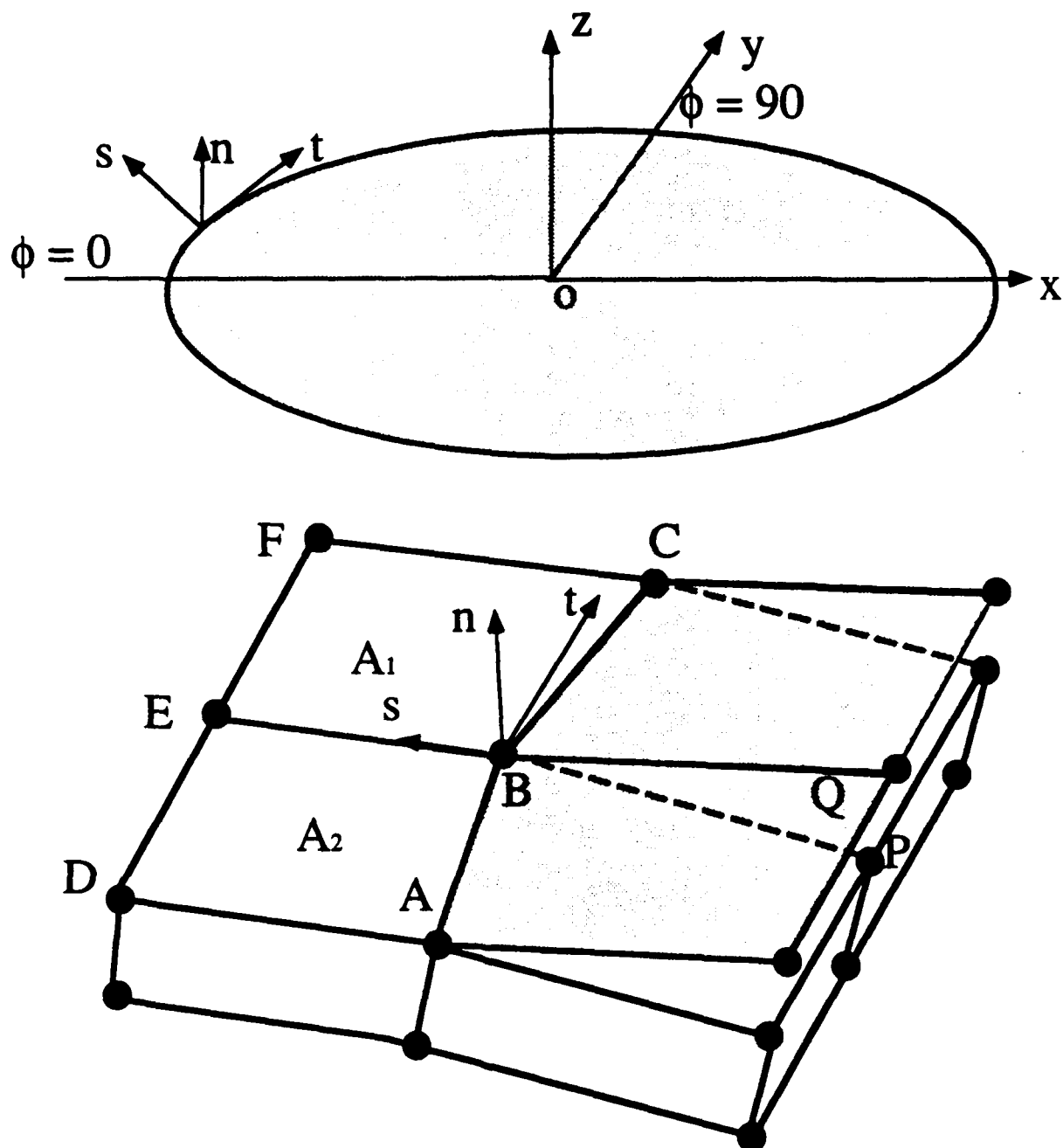


Figure 4.8 Global and local coordinate system used for energy release rates calculation.

§4.4 Verification with Existing Data

The proposed 3-D FEM model was verified by comparing calculations with existing analytical and test results.

A DCB under a Line Load

It was shown by Davidson *et al.* [81-83] that a DCB I specimen with a straight delamination front had the highest value of strain energy release rate G_I at the center and lowest value at its edges. The solutions were obtained in three dimensions, using the commercial finite element code ABAQUS. The material used was Hexcel T300/F155 graphite epoxy. Its properties are shown in Table 4-1. Similar numerical calculations were performed using the current code, and the results were compared with the ones given by Davidson *et al.* [81].

Table 4-1
Material properties for Fiberite T300/F155.

| Material Property | Value | Units |
|--------------------------------------|-------|-------|
| Longitudinal Young's modulus, E_x | 17.9 | msi |
| Transverse Young's modulus, E_y | 1.105 | msi |
| Out-of-plane Young's modulus, E_z | 1.105 | msi |
| Poisson's ratio, ν_{xy} | 0.34 | |
| Poisson's ratio, ν_{xz} | 0.34 | |
| Poisson's ratio, ν_{yz} | 0.34 | |
| In-plane shear modulus, G_{xy} | 0.5 | msi |
| Out-of-plane shear modulus, G_{xz} | 0.5 | msi |
| Out-of-plane shear modulus, G_{yz} | 0.5 | msi |

For DCB in Mode I (see Figure 4.9), the comparison between the solutions from [83] and the current code agreed quite well. The G_I in the middle portion of the laminate for $[0]_{24}$ was fairly flat, but it was very sensitive to the ply orientation. For $[0]_{24}$, the G_I value varies significantly along the width of the specimen. It is believed that this phenomenon occurs because, when the beam is in bending, the upper and lower arms of the beam deform anticlastically and tends to close the crack near the free edge. As a result, the crack surfaces near the free edge may be in contact due to the anticlastic curvature effect for angle ply laminates. For $[45/-45/(-45/45)_2]_{2s}$, it was found that the finite element nodes on upper and lower arms of the DCB specimen penetrated into each other without imposing the contact model, as shown in Figure 4.9. By using the contact model, the overlapping between the edges of the upper and lower arms was prevented, resulting in the zero G_I value at the edge nodes. The observation that a small contact area at the free edge of the crack front actually agreed well with the experimental findings [81, 82].

Therefore, the G_I was the highest in the middle of the laminates, and the middle portion would grow earlier when the DCB specimens were subjected to a line load. Actually, it was observed by Davidson *et al.* [81] that in DCB Mode I testing, the delamination front was somewhat thumbnail shaped.

Numerical simulations were also performed on the DCB specimens due to Mode II loading. The solutions show that the G_{II} values were fairly constant for the $[0]_{24}$ laminate, but varies very drastically along the width of the specimen for angle ply laminate. The G_{II} distribution was very much different from that of the Mode I for the same ply orientation. Surprisingly, it was found from the calculation that only a narrow strip of elements were in contact along the loading edge, while the rest of the crack surfaces was open.

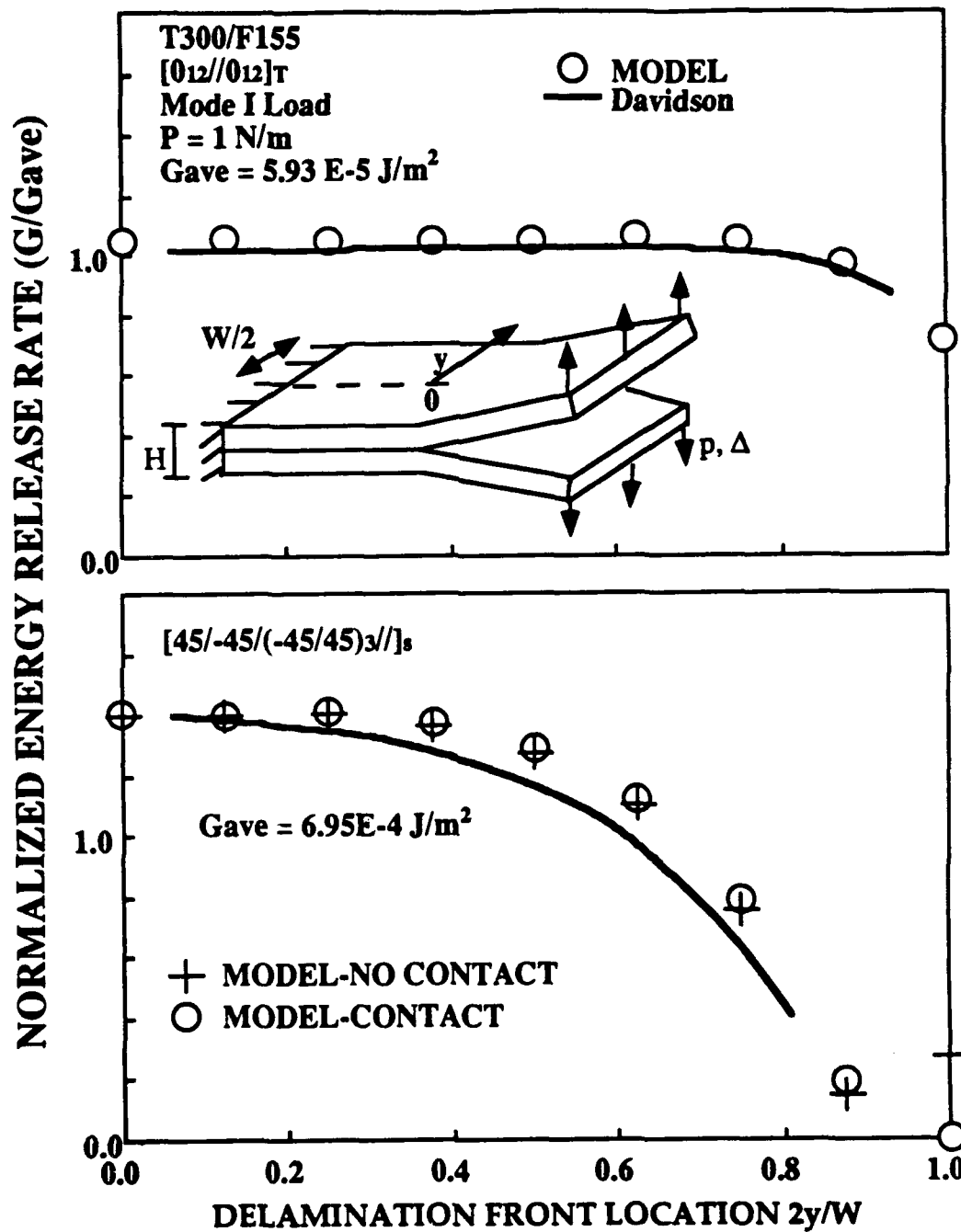


Figure 4.9 Distribution of G_I for angle-ply DCB specimens with straight delamination fronts in Mode I. ($W = 1 \text{ in.}$, $c \approx 1 \text{ in.}$)

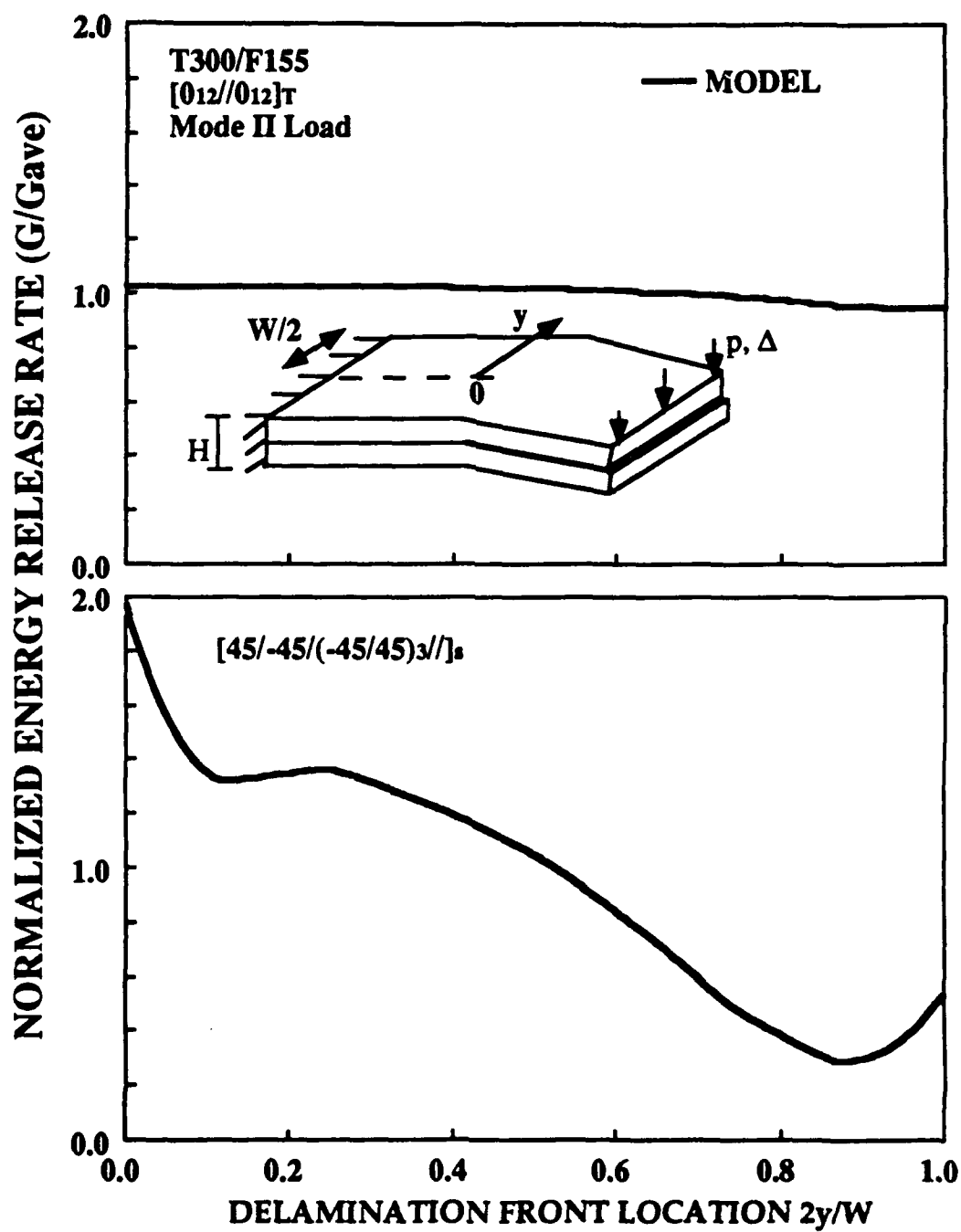


Figure 4.10 Distribution of G_{II} for angle-ply DCB specimens with straight delamination fronts in Mode II. ($W = 1$ in, $c = 1$ in.)

A Circular Plate under the Point Load

A closed form solution (CFS) for a circular isotropic plate due to a central point load is given in [80]. The solution is exact for linear deflections and approximate for large deflections. The transverse deflections at the center of the plate were determined by the current code as a function of the applied load. In Figure 4.11, the present solution is compared to an approximate solution given by Timoshenko [80]

$$0.217 \frac{Pa^2}{Eh^4} = \frac{w_o}{h} + 0.443 \left(\frac{w_o}{h} \right)^3 \quad (4.31)$$

where w_o is the transverse deflection at the center of a thin plate. The thickness and the radius of the plate were 0.1 in and 2 in, respectively. The Young's modulus was 3 msi and the Poisson's ratio was 0.3. It is shown that the present solution and Timoshenko's solution agreed fairly well.

An Aluminium Thick Plate Loaded by a Spherical Indenter

The analytical solution for the contact force f with respect to the indentation α is defined by the elastic contact law [10, 11] given by:

$$f = k\alpha^n \quad (4.32)$$

where the exponent n can be taken as 1.5 for a homogeneous transversely isotropic plate and the contact stiffness k can be given as

$$k = \frac{4}{3} R^{0.5} \frac{E_z}{1 - \nu^2} \quad (4.33)$$

where the indenter is assumed to be rigid. The ν is the poisson ration for the plate and the E_z is the Young's modulus of the plate in the thickness direction. The Young's modulus was 3 msi and the Poisson's ratio was 0.3. The R is the radius of the indenter and its value here was 0.25 in.

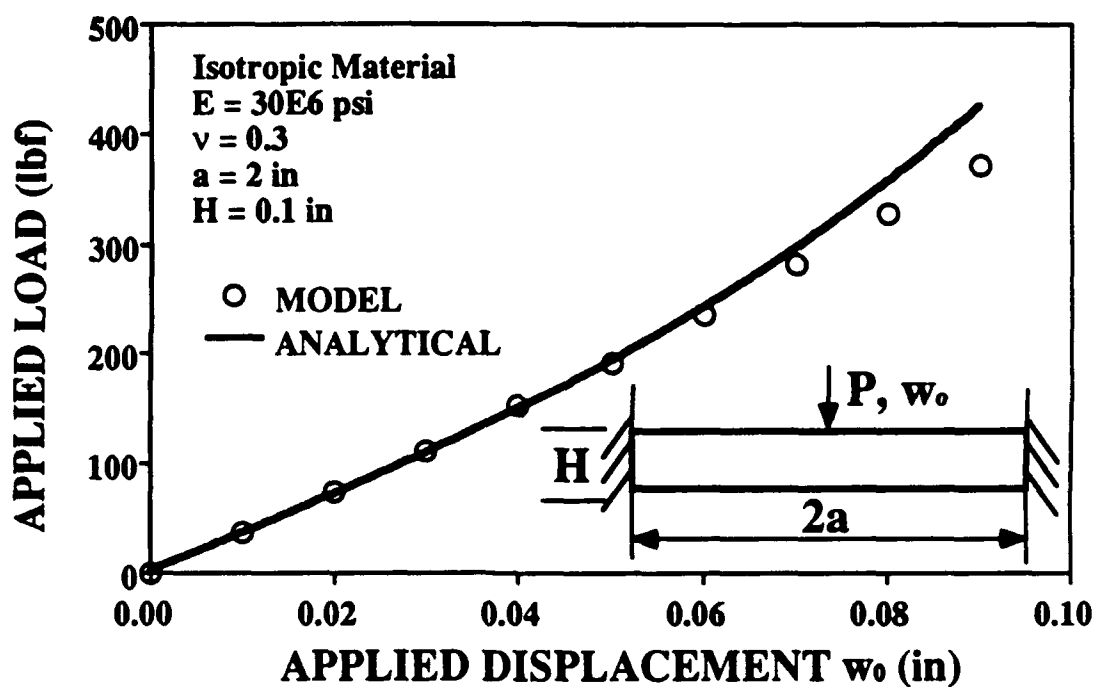


Figure 4.11 A load-displacement curve for a circular plate subjected to a central point load. Comparison between the calculations and elasticity solutions.

The plate had a length of 4 in, a width of 3 in, and a depth of 1.3 in. The bottom of the plate was placed on the rigid support (i.e., $w = 0$ for the bottom surface of the plate). The four edges were simply-supported. The indenter was applied downward at the center of the plate. Only 1/4 plate was modeled. Figure 4.12 gives the comparison between the elasticity solution and the solution obtained by the proposed finite element analysis. It is shown that the present solution and the elasticity solution agreed fairly well.

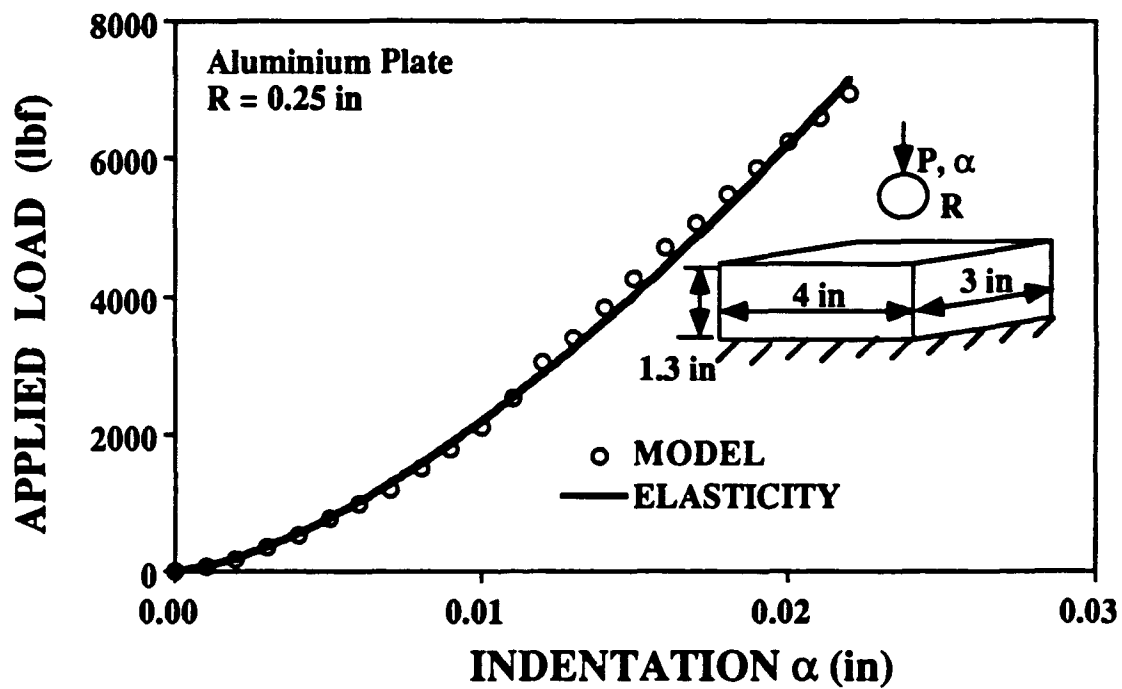


Figure 4.12 The load-indentation curve for an aluminium plate subjected to a spherical indenter with a radius of 0.25 in. Comparison between the predictions and the analytical solution..

§4.5 Results and Comparison

In order to further substantiate the proposed analysis, numerical calculations were performed to compare with the experimental data generated during the investigation or obtained from the literature. Two types of material systems were selected for comparison: T300/976 and T800H/3900-2 graphite/epoxy materials. Both composites contain thermoset resin systems, but T800H/3900-2 composite is toughened on the interfaces with thin polyamide particles [84]. The stiffness and strengths of unidirectional composites of both materials are very similar, except strain energy release rates G_{IC} and G_{IIC} . Due to its toughening interface, T800H/3900-2 composite has much higher fracture toughnesses than T300/976, especially for G_{IIC} values as shown in Table 4-2.

Test data on T300/976 composite were taken from Finn and Springer [1], while experiments on T800H/3900-2 composite were conducted during this investigation. Three different layups were selected: $[0_6/90_2]_s$, $[0_2/90_6]_s$, and $[0_4/90_4]_s$. The experiments on T800H/3900-2 composite followed the same procedures as were used by Finn and Springer for T300/976 composite. All the specimens had the same number of plies (16 plies), width (3in), and length (4in). During the tests, the specimens were clamped on the two parallel edges and free on the others. A transverse concentrated load induced through an indenter of radius 0.25 in was applied by an MTS machine. Displacement control was used throughout all the tests.

All the specimens were X-rayed before and after each test to examine internal damage resulting from the applied load. The applied energy (load) as a function of measured delamination size from X-radiographs was also recorded. Figure 4.13 shows typical damage patterns from X-radiographs for three different layups of T300/976 composite at a given input energy. The straight lines indicated matrix cracks and the area bounded by white contour curve was delamination. It is worth

noting that the shape of the delamination strongly depended upon the ply orientation and was considerably different for each of the three layups.

Table 4-2
Material properties for Fiberite T800H/3900-2.

| Material Property | Value | Units |
|--|----------|--------|
| Longitudinal Young's modulus, E_x | 23.2 | msi |
| Transverse Young's modulus, E_y | 1.33 | msi |
| Out-of-plane Young's modulus, E_z | 1.33 | msi |
| Poisson's ratio, ν_{xy} | 0.28 | |
| Poisson's ratio, ν_{xz} | 0.28 | |
| Poisson's ratio, ν_{yz} | 0.28 | |
| In-plane shear modulus, G_{xy} | 0.90 | msi |
| Out-of-plane shear modulus, G_{xz} | 0.90 | msi |
| Out-of-plane shear modulus, G_{yz} | 0.90 | msi |
| Longitudinal tensile strength, X_t | 413 | ksi |
| Longitudinal compressive strength, X_c | 191 | ksi |
| Transverse tensile strength, Y_t | 6.41 | ksi |
| Transverse compressive strength, Y_c | 24.4 | ksi |
| Longitudinal shear strength (cross ply), S_{cp} | 52.89 | ksi |
| Critical strain energy release rate for mode I, G_{Ic} | 1.50 | lbf/in |
| Critical strain energy release rate for mode II, G_{IIc} | 18.0 | lbf/in |
| Ply thickness h_o | 0.006535 | in |

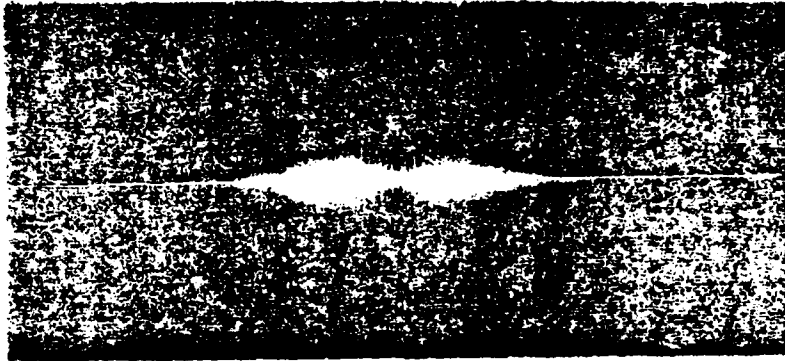
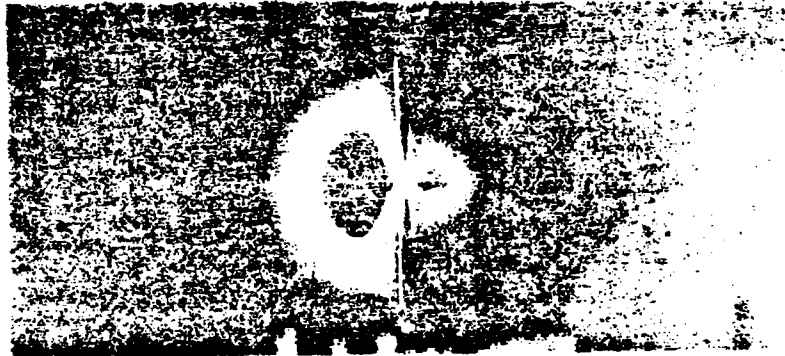
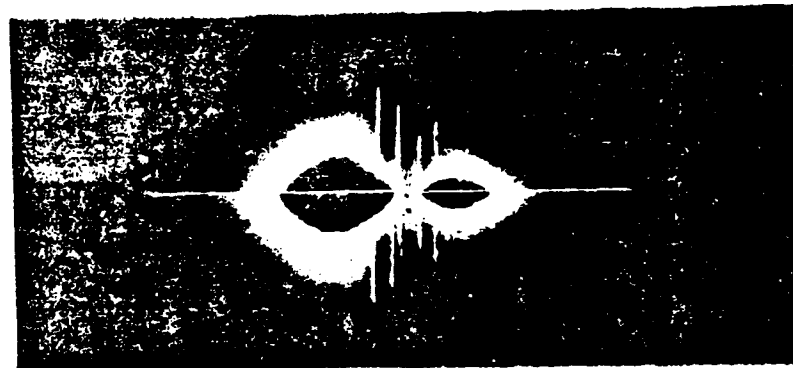
T300/976**[06/902]_s****[02/906]_s****[04/904]_s**

Figure 4.13 X-Radiographs of graphite/epoxy composites resulting from a quasi-static transverse load. a) [0₆/90₂]_s layup; b) [0₂/90₆]_s; and c) [0₄/90₄]_s. Data taken from [1].

For $[0_6/90_2]_s$ layup, a long slender peanut-like shape of a delamination on the interface near the bottom surface was observed. A matrix crack (bending crack) in the bottom 0 degree ply group was also clearly seen from the X-radiograph given in Figure 4.13. The left and right half of the delaminations always grew in a relatively equal size. However, for $[0_2/90_6]_s$ layup, the damage pattern was considerably different from $[0_6/90_2]_s$. Distinct matrix cracks (shear cracks) in the central 90 degree ply group near the loading area could be seen clearly in addition to the bending crack, and the delamination shape was much wider and close to a semi-circular shape on each side which was quite unevenly distributed. Meanwhile, the $[0_4/90_4]_s$ layup seems to produce a damage pattern somewhere in between the $[0_6/90_2]_s$ and the $[0_6/90_2]_s$ layups.

For T800H/3900-2 composite, the damage patterns were very similar to those of T300/976 composite for the same ply orientation, except that the delamination sizes were substantially smaller than those of T300/976. There was no delamination damage below a certain energy level in T800H/3900-2 composite, at which the T300/976 composite was already severely damaged. At a given amount of the applied load, when panels made of both materials had damage, the damage size in $[0_2/90_6]_s$ of T800H/3900-2 was about only one-fifth of the observed from T300/976. A comparison of damage size between T300/976 and T800H/3900-2 for various amounts of input energy is shown in Figure 4.14.

T300/976 $[0_6/90_2]_s$ Panels

In order to evaluate the damage propagation in $[0_6/90_2]_s$ composites due to transverse concentrated loading, both types 1 and 2 damage models were utilized to perform the numerical simulations. The type 1 model considered only a delamination without a bending crack, however, type 2 model considered both the delamination and the bending crack. The typical meshes used in the calculations

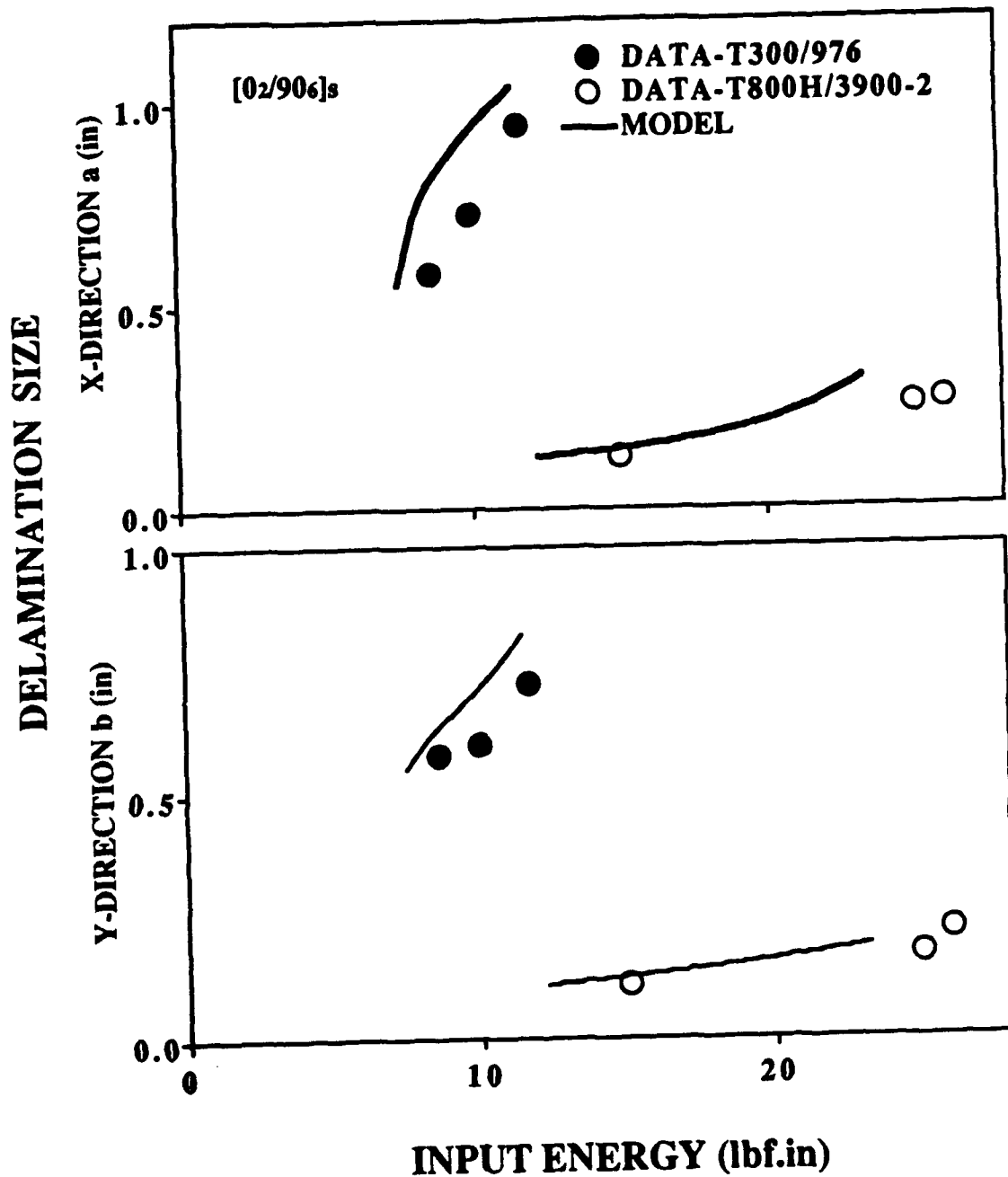


Figure 4.14 Comparison between the measured and predicted delamination sizes in $[0_6/90_2]_s$ composites made of T300/976 and T800H/3900-2 with respect to quasi-impact energy.

were given previously in Figure 4.13-a.

The mesh, deformation, and stress data generated from the finite element analysis were stored in standard post-processing files and transformed to the commercial code I - DEAS [69] (licensed by Structural Dynamics Research Corporation). Figure 4.15 shows a close-up view of a deformed cross-section ($X - Z$, $Y = 0$) of a $[0_6/90_2]_s$ composite at a load of 172 lbf. The local indentation due to the rigid indenter can be clearly observed in the figure. A relatively large sliding between the upper and lower surfaces of the delamination were also clearly shown in the figure.

A close-up side view of a deformed cross-section ($Y - Z$, $X = 0$) of a $[0_6/90_2]_s$ is shown in Figure 4.16. The bending crack was open due to the applied load, which closely resembles the cylindrical bending of a $[90_m/0_n]_s$ beam containing a surface crack. The local indentation due to the rigid indenter and relatively large sliding between the upper and lower surfaces of the delamination were also shown in the figure.

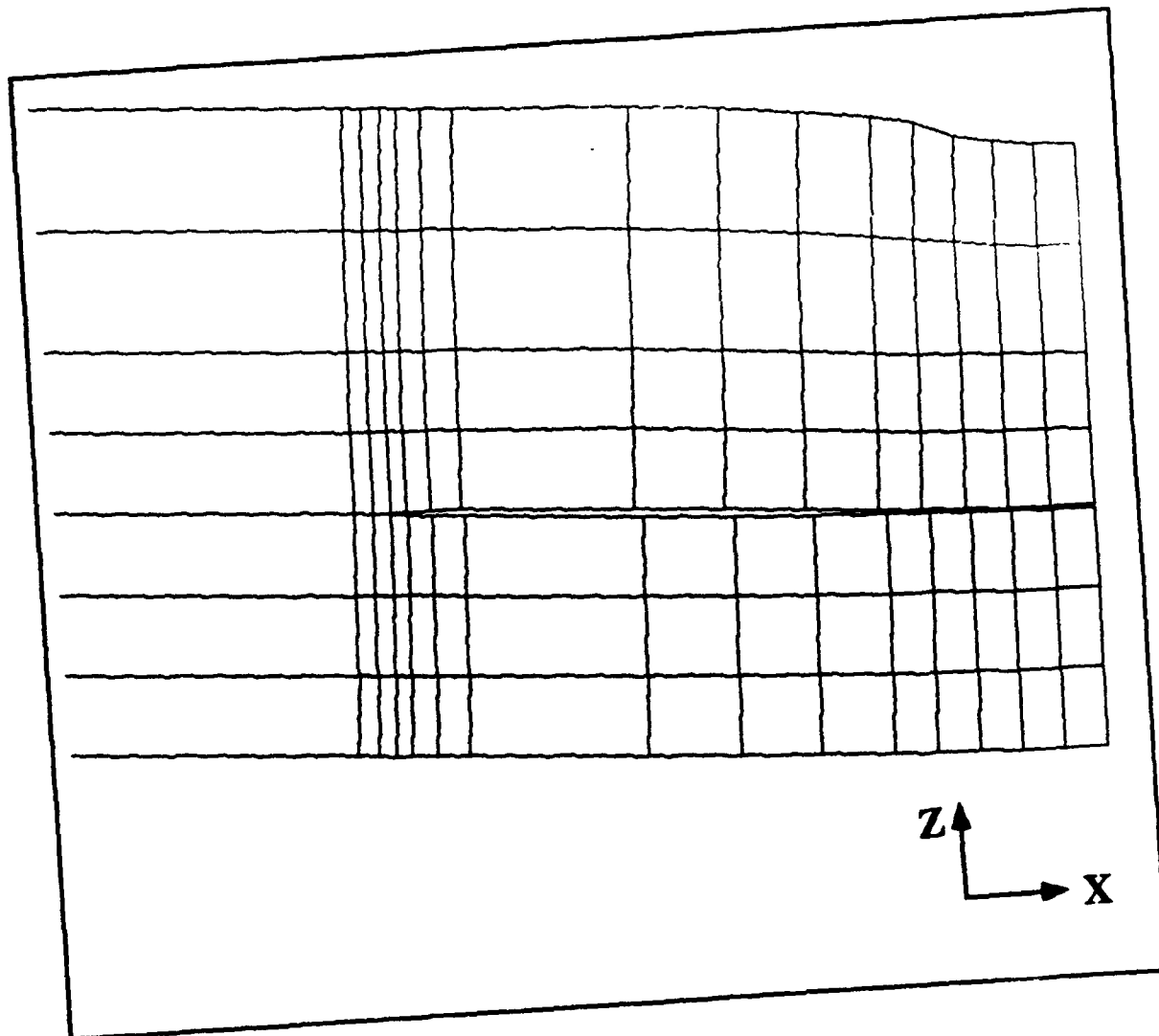


Figure 4.15 Deformation of a cross-section ($X-Z, Y = 0$) of a $[0_6/90_2]_s$ composite with a surface matrix crack.

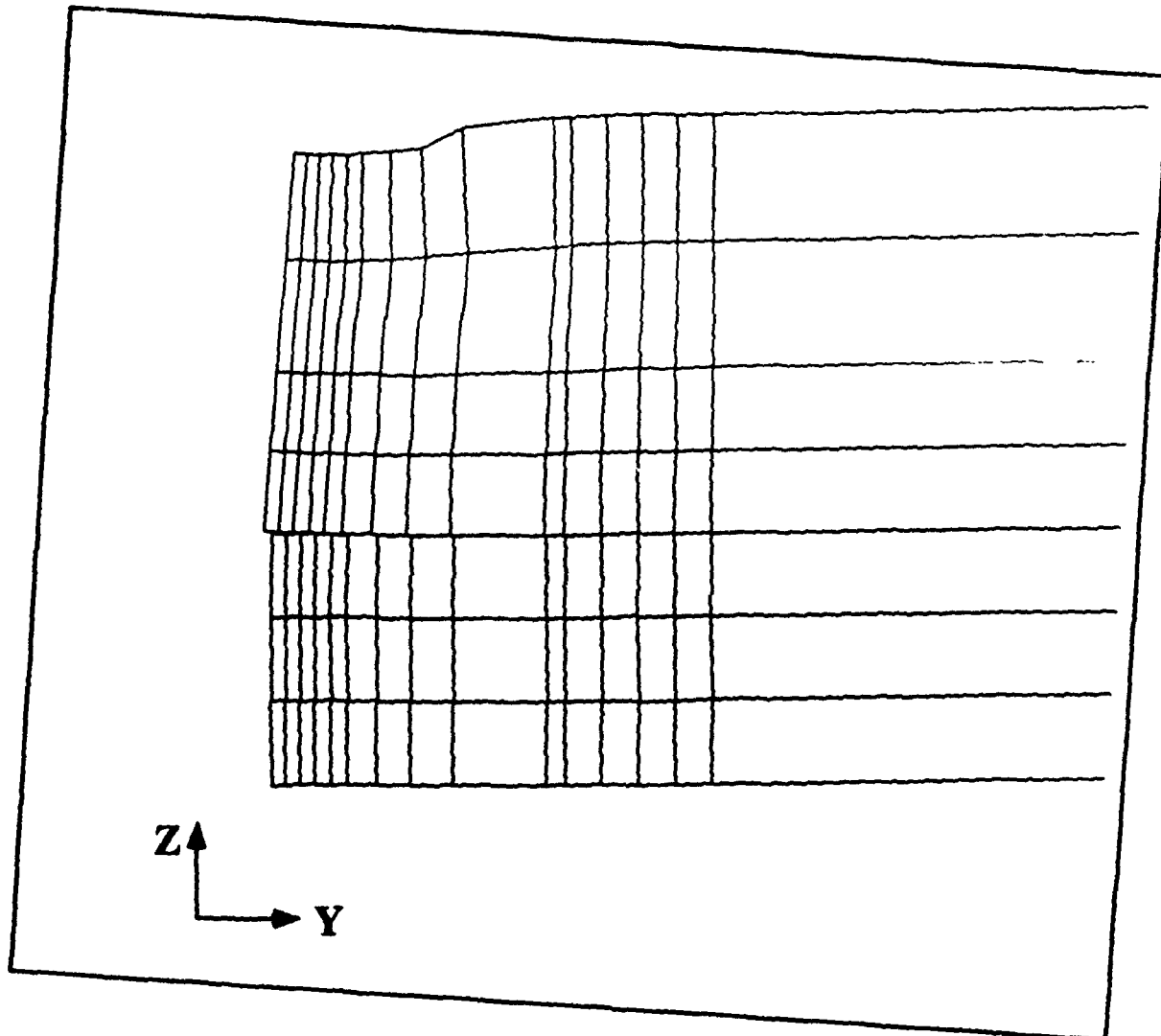


Figure 4.16 Deformation of a cross-section ($Y-Z, X=0$) of a $[0_6/90_2]_s$ composite with a surface matrix crack.

Figure 4.17 shows the comparison of the calculated total strain energy release rate G_T based on types 1 and 2 models for a laminate containing a small circular delamination with and without the surface matrix crack (bending crack). For the laminate containing the matrix crack, the value of G_T along the delamination front near the location of the the matrix crack increased significantly and reached a peak at the intersection between the matrix crack and delamination (at $\phi = 0^\circ$). The value of G_T , however, decreased rapidly as the delamination front, where the value of G_T was calculated, moved away from the location of the matrix crack (ϕ approaches to 90°).

A completely different distribution of the total strain energy release rate was obtained for the laminate containing no bending crack. Overall, the values of G_T obtained from the type 1 model were much smaller than those calculated by the type 2 model. Apparently, the laminate with the matrix crack could initiate the delamination growth at a much earlier loading stage than the one without. Once the delamination propagated, it would grow along the direction of matrix cracking.

Figure 4.18 shows the sequence of the delamination growth in the laminate without the matrix crack predicted by the type 1 model based on the crack growth criterion (Eq. (4.8)). The number shown in the bracket at the upper right corner of each sub-figure indicates the sequence. The sub-figures were generated by evaluating the strain energy release rate ratio E_d for various sizes of delaminations. First, the values of E_d were calculated for a small circular implanted delamination. If delamination growth was predicted ($E_d \geq 1$), then the delamination size was extended slightly along its major (X -direction, $\phi = 0^\circ$) or minor (Y -direction, $\phi = 90^\circ$) axis according to the predicted direction of delamination growth. In this analysis, the delamination was only allowed to grow into either a circular or an elliptical shape. Again, numerical calculations were re-performed to evaluate the strain en-

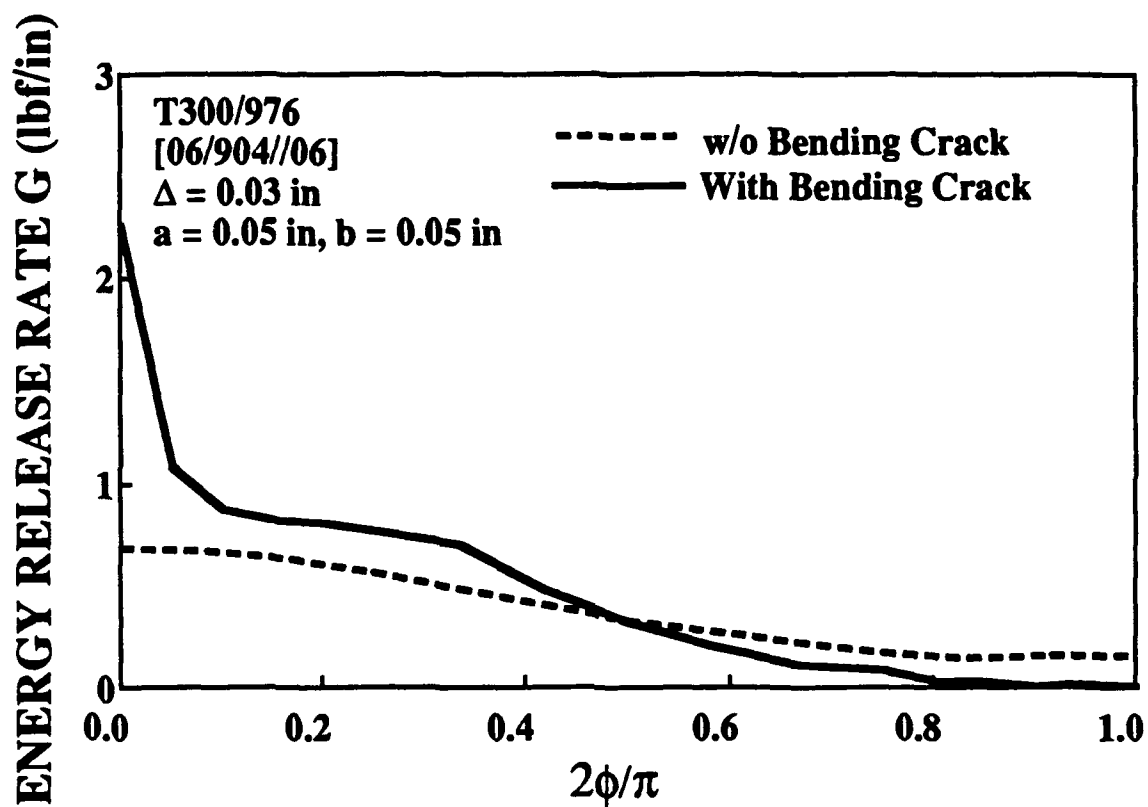


Figure 4.17 Comparison of the calculated total strain energy release rate along a delamination front in a $[0_6/90_2]_s$ composite with or without a surface matrix crack.

ergy release rates for the laminate with the new delamination. This procedure was repeated until the calculated strain energy release rate ratio was smaller than unity everywhere along the delamination front. The size of the final delamination was then considered to be the delamination shape corresponding to the given loading condition.

At 0.05 inches of indenter displacement, Figure 4.18-1 shows that delamination growth initiated at $\phi = 0^\circ$. As the delamination expanded along its major axis from Figure 4.18-1 to Figure 4.18-2, the strain energy release rate increased, indicating an unstable growth. It is noted that as the delamination continued to expand along its major axis, the peak of the strain energy release rate ratio gradually shifted more and more toward $\phi = 90^\circ$, indicating a much more uniform expansion of delamination. Figure 4.18-3 indicates delamination expansion along the minor axis due to high strain energy release rates near $\phi = 90^\circ$. The distribution of the strain energy release rate ratio along the delamination front for all the delaminations was relatively uniform compared to that of the laminate with the matrix crack. As a result, the delamination tended to grow into an elliptical shape with major and minor axis ratio about 2.

However, the delamination shape predicted by the type 1 model was significantly different from the shape observed in the experiment. First, the well-known peanut-like delamination could not be predicted. Second, the predicted shape was fairly large instead of slender and was very different from the observed delamination shape with major and minor axis ratio about 5. And third, the applied load (or displacement) which initiated the delamination growth was much higher than the experimental one. It was noted that something was missing in the type 1 model for simulating the delamination growth due to a spherical indenter loading. It seemed to show that the type 1 model could not predict accurately the damage growth in

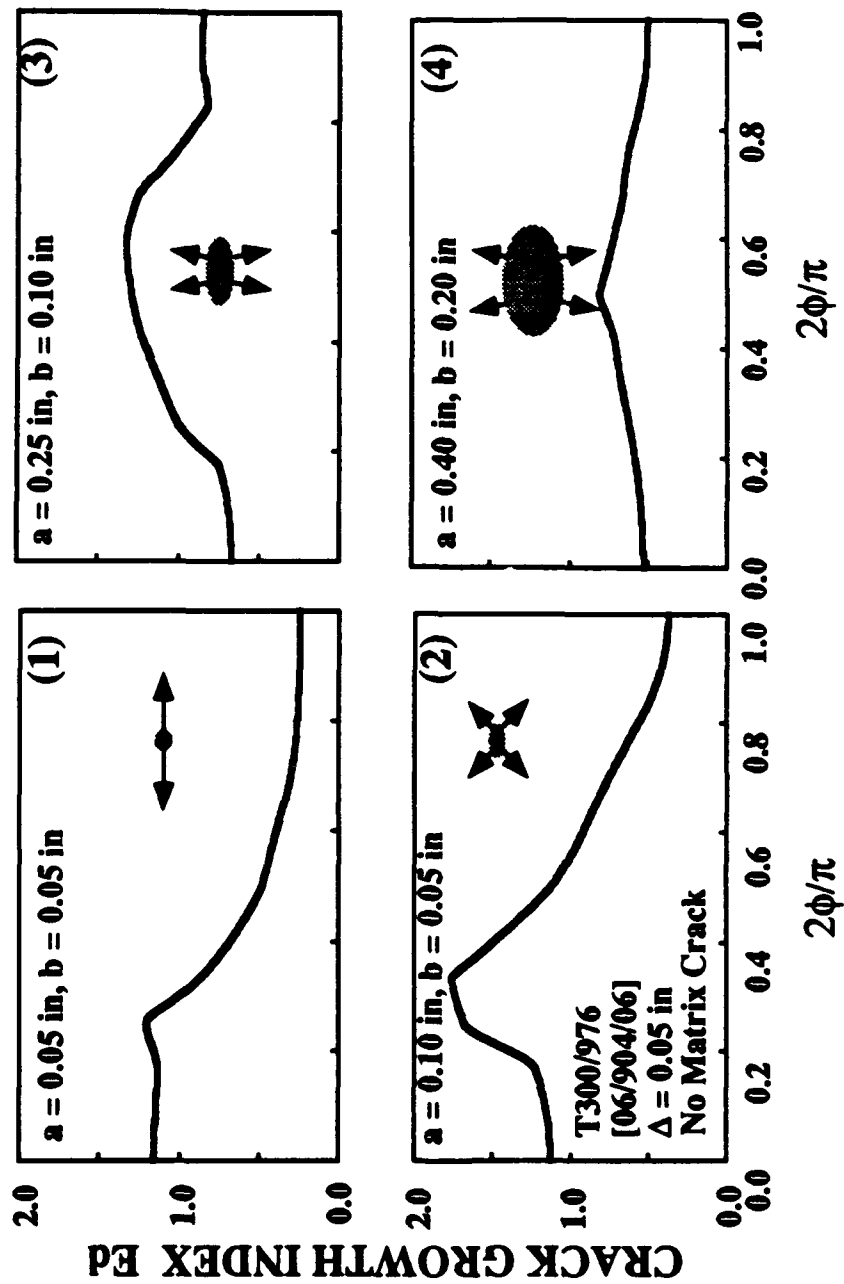


Figure 4.18 The predicted delamination growth sequence in a $[0_6/90_2]_s$ composite without a surface matrix crack.

this laminate due to a spherical indenter.

However, a completely different growth pattern was predicted by the type 2 model. First, at the same load, delamination growth was predicted to occur much earlier for the laminate containing the same small delamination given in Figure 4.19-1. Figure 4.19 shows the sequence of the delamination growth in the laminate with the matrix crack predicted by the type 2 model.

At a fixed indenter displacement, Figure 4.19-1 and Figure 4.19-2 show that the initial delamination grew from a small circular shape into a slender elliptical shape along the direction at $\phi = 0^\circ$ with its major axis parallel to the fiber direction of the bottom ply group. The delamination growth was unstable because the strain energy release rates actually increased as the delamination expanded. Figure 4.19-3 indicates that delamination continued to expand along its major axis, until the strain energy release rate ratio started to decrease along the delamination front near $\phi = 0^\circ$.

After a substantial growth of the delamination along its major axis, Figure 4.19-4 shows that the strain energy release rates started to increase near $\phi = 75^\circ$ away from the matrix crack, initiating the expansion of the delamination along the minor axis. However, a slight expansion of the delamination along its minor axis as shown in Figure 4.19-5 subsequently caused a significant increase of the strain energy release rates along the major axis. Hence, the delamination started to grow along the major axis again. Apparently, the growth of the delamination was predominantly controlled by the delamination front near the neighborhood where the matrix crack intersected with the delamination. It is worth noting that at $\phi = 90^\circ$, strain energy release rates remained at a minimum regardless of the shape of the delamination. This observation implies that no delamination would grow in this area, leading the delamination to a peanut shape which was frequently observed from the experiments

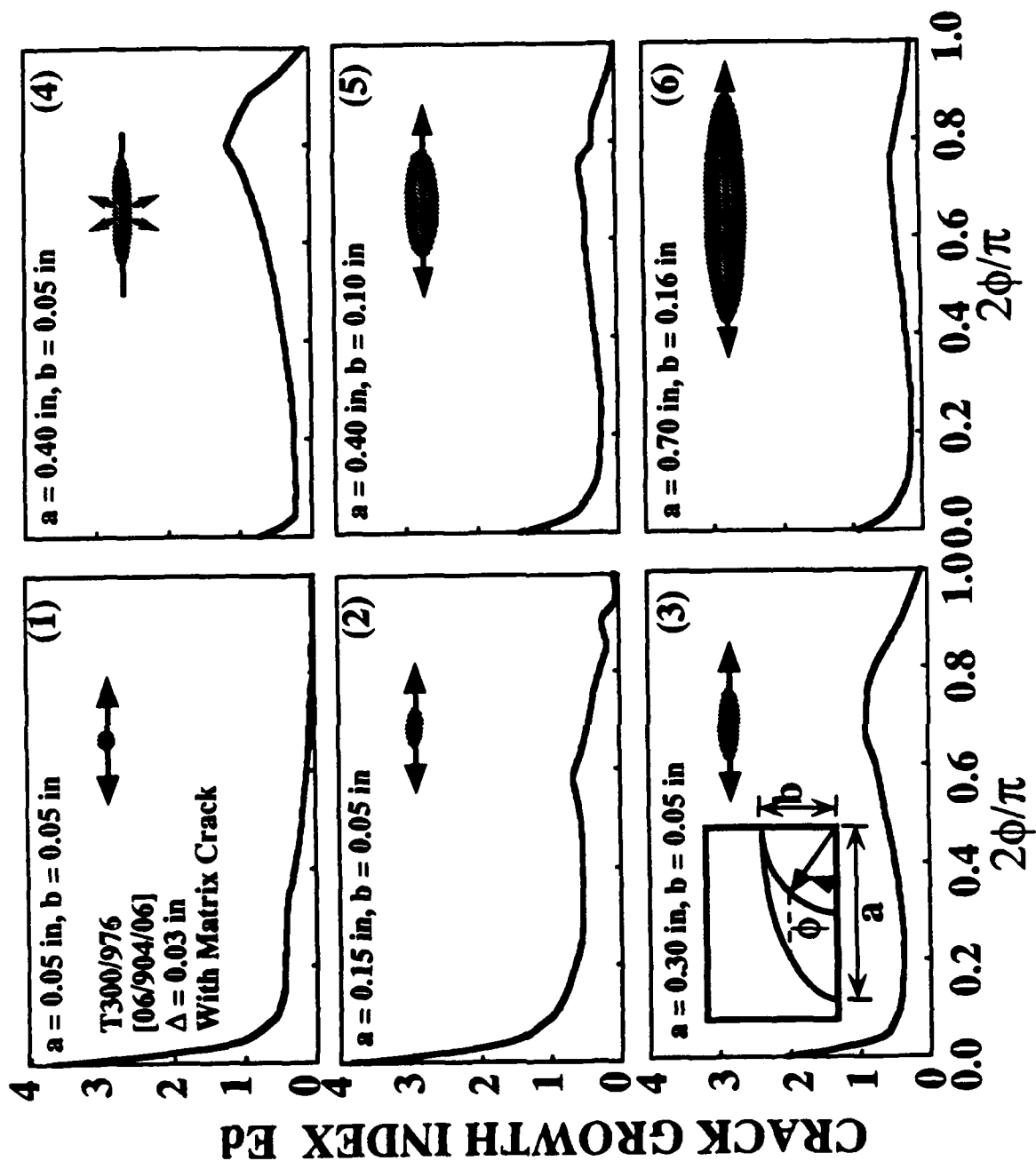


Figure 4.19 The predicted delamination growth sequence in a $[0_6/90_2]_s$ composite containing a surface matrix crack.

for this type of ply orientataion, such as the one given in Figure 4.13.

Figure 4.20 shows the comparisons between the estimated delamination sizes in the x and y directions and the sizes measured from the experiments. The correlation between the experiments and the predictions was very good. Figure 4.21 shows the calculated strain energy release rates of Modes I, II, and III for the laminate containing a small and a large delamination with a surface matrix crack. Clearly, for the laminate containing the initial surface matrix crack, G_I (Mode I fracture) dominated the total strain energy release rate along the delamination front near the neighborhood where the surface matrix crack intersected with the delamination ($\phi = 0^\circ$). This observation is also valid for a moderately large delamination, as shown in the same figure.

However, when the surface crack was ignored in the analysis, Modes II and III fractures dominated the total strain energy release rate along the delamination front for the laminate, as shown in Figure 4.22. Although the contribution of each mode to the growth of the delamination strongly depended upon the current shape of delamination, the presence of the matrix crack clearly played a very important role in the delamination growth. Therefore, it is very important that the initial matrix crack be considered in the analysis for understanding the damage mechanics and mechanism of laminated composites due to transverse loading.

T300/976 [0₂/90₆]_s Panels

Type 3 and 4 models were used to study the delamination growth behavior in [0₂/90₆]_s composites. The type 3 model simulates a delamination induced by a pair of shear cracks, while the type 4 model considers both a bending crack and shear cracks in conjunction with a delamination. Therefore, numerical calculations were generated for the laminate containing a delamination with various sizes and a shear crack in the middle 90° ply group with and without a surface bending crack

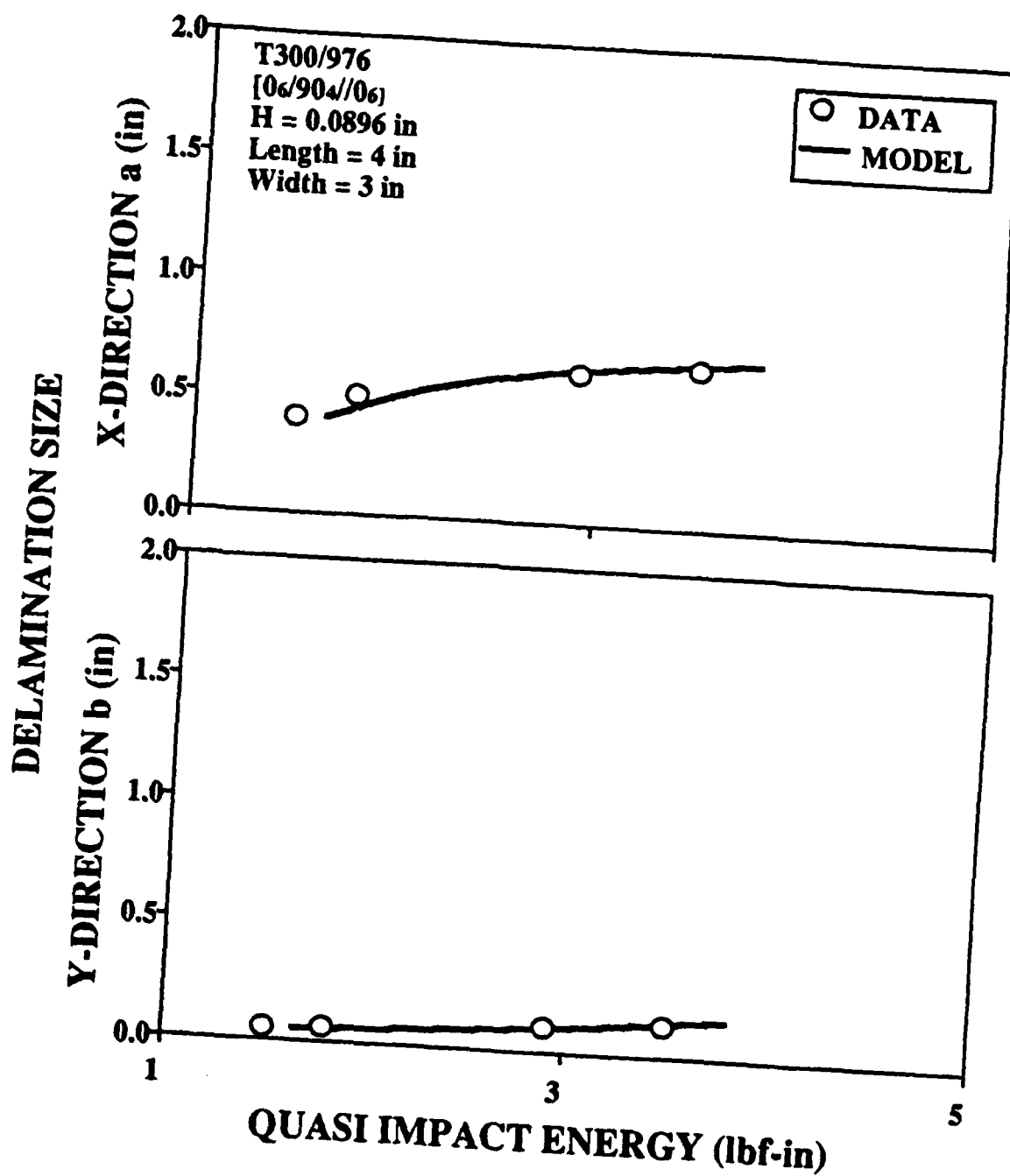


Figure 4.20 Comparison of delamination sizes predicted and measured in a $[0_6/90_2]_s$ composite with respect to quasi-impact energy.

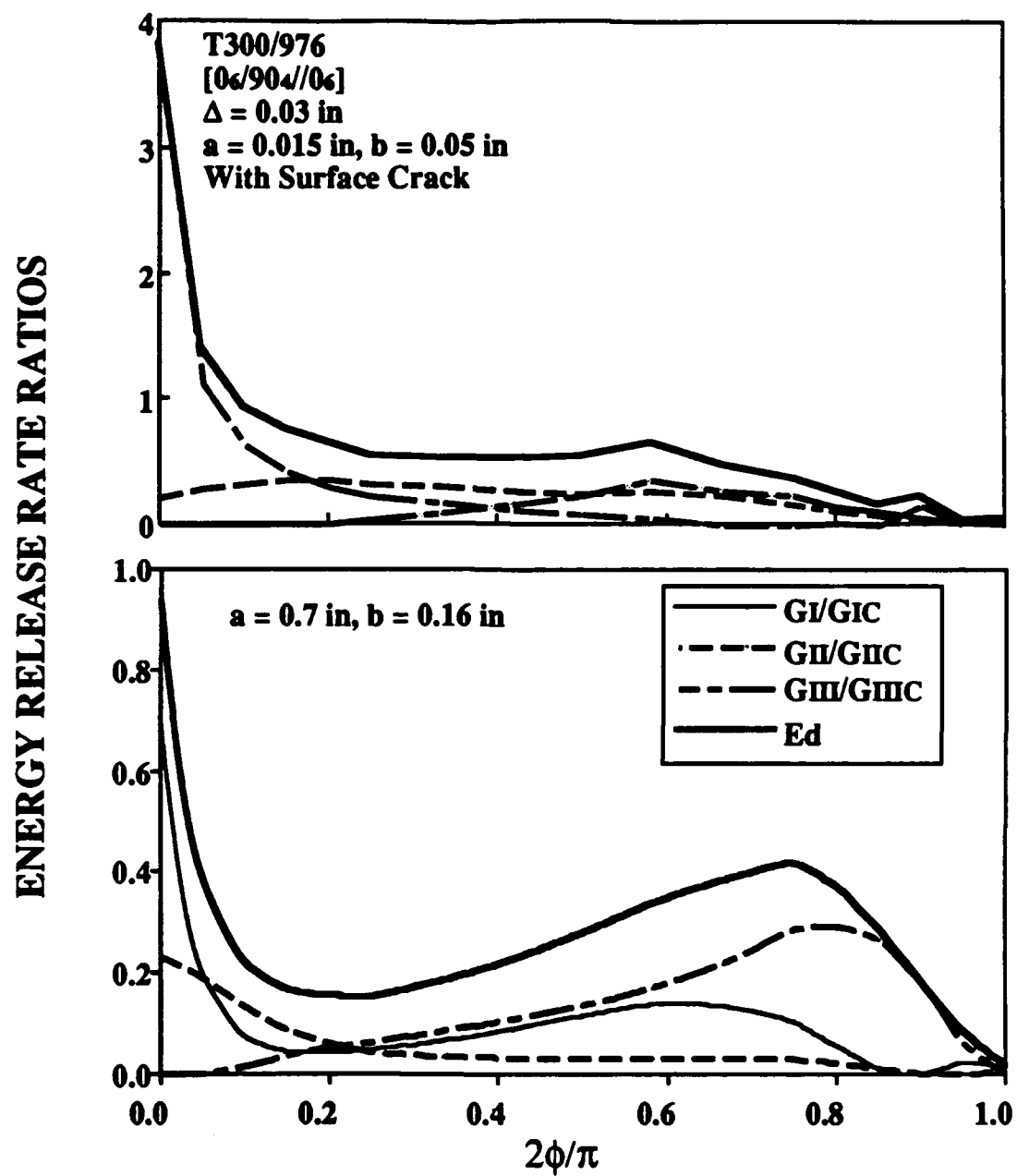


Figure 4.21 Comparison of the calculated strain energy release rates of Modes I, II, and III along a small and a large delamination front in a $[0_6/90_2]_s$ composite.

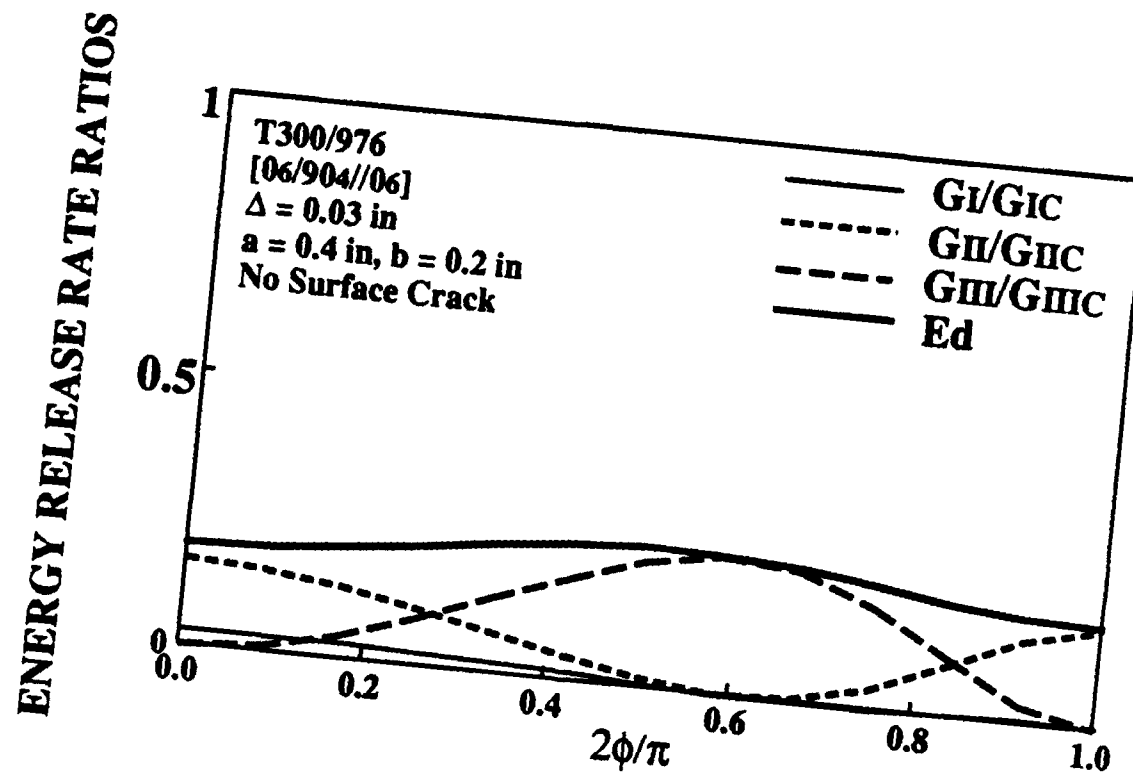


Figure 4.22 The calculated strain energy release rates of Modes I, II, and III along a delamination front in a $[0_6/90_2]_s$ composite without a surface matrix crack.

in the bottom 0° ply group. As suggested by the experimental observation, the lengths of the matrix cracks were assumed to be slightly larger than the delamination length and width in the x and y directions throughout the calculations. In the following figures, similar to the $[0_6/90_2]_s$ case, numerical results will be presented for delaminations from small to large sizes.

A close-up view of a deformed cross-section ($X - Z$, $Y = 0$) of a $[0_2/90_6]_s$ panel at a load of 327 lbf is shown in Figure 4.23. The local indentation due to the rigid indenter and relatively large sliding between the two surfaces of the delamination and internal crack are clearly shown in Figure 4.23.

Figure 4.24 shows the sequence of the delamination growth in the laminate containing a pair of shear cracks predicted by the type 3 model. At the fixed indenter displacement, Figure 4.24-1 and Figure 4.24-2 show that the initial delamination grew from a small elliptical shape into a wider elliptical shape along the direction at $\phi = 90^\circ$ with its minor axis perpendicular to the fiber direction of the bottom ply group. The delamination growth was unstable because the strain energy release rates increased as the delamination expanded. Figure 4.24-3 indicates that the delamination began to expand along its major axis, as the strain energy release rate ratio started to decrease along the delamination front near $\phi = 90^\circ$ and had the highest value at the delamination front near $\phi = 0^\circ$.

The expansion of the delamination along its major or minor axis ceased to increase when the growth index E_d along the delamination front was below unity, as in the case shown in Figure 4.24-6. The delamination shape shown in Figure 4.24-6 is approximately a circular one, which agreed with the delamination shape of $[0_2/90_6]_s$ panels observed from the experiments (see Figure 4.13-b). Figure 4.25 shows the comparisons between the estimated delamination sizes in the x and y directions and the sizes measured from the experiments. The correlation between

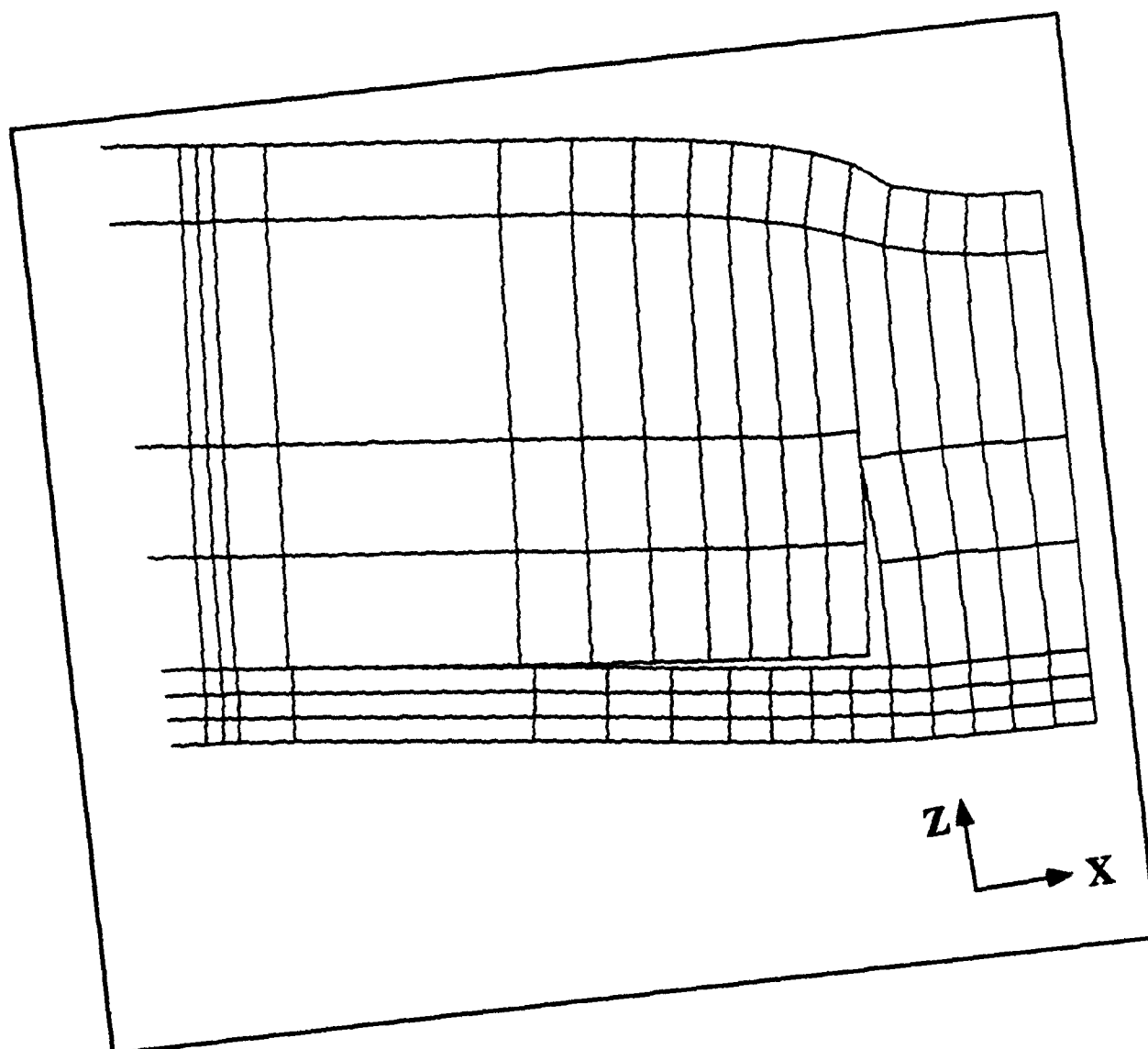


Figure 4.23 Deformation of a cross-section ($X-Z, Y=0$) of a $[0_2/90_6]_s$ composite with a surface matrix crack.

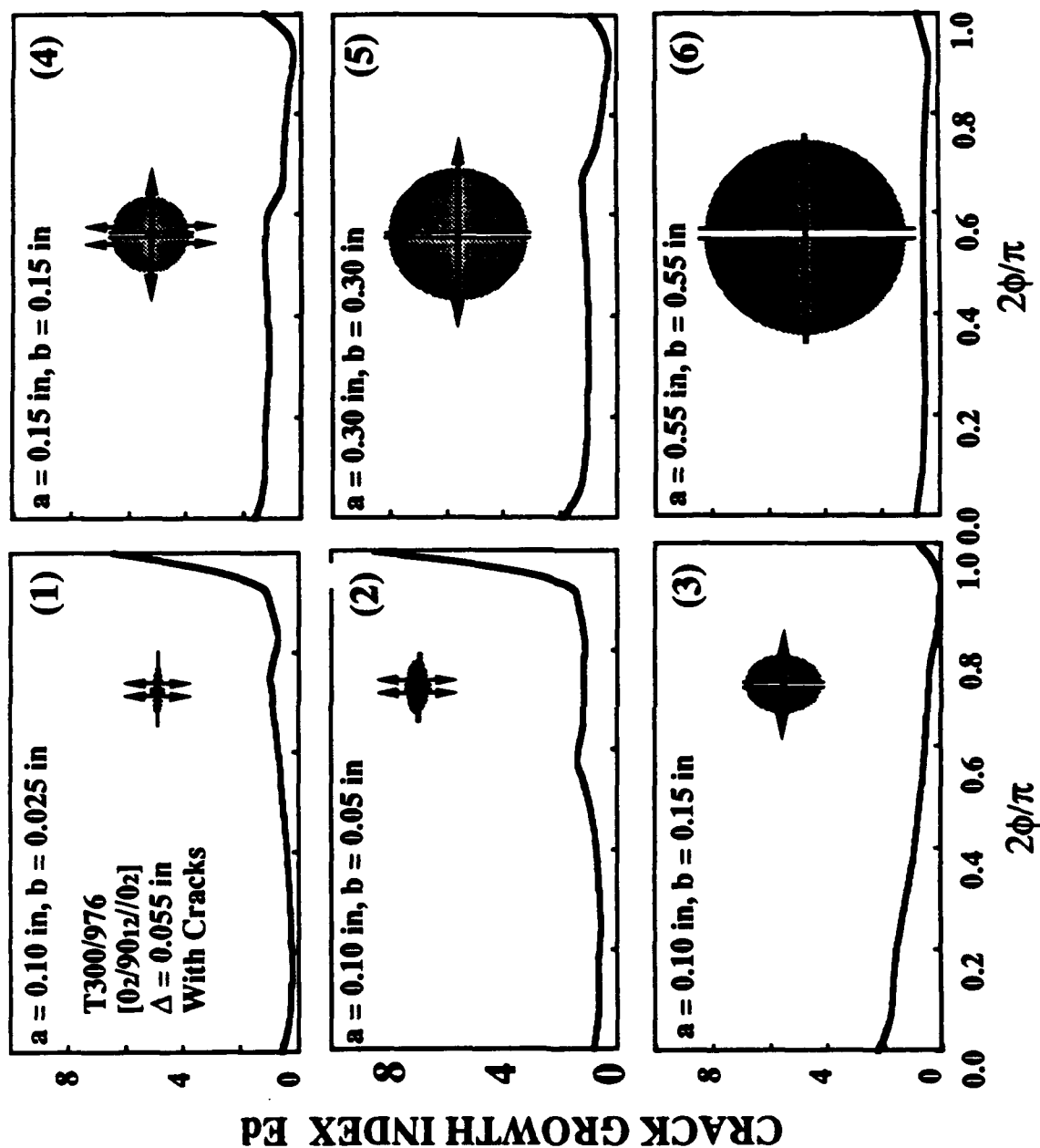


Figure 4.24 The predicted delamination growth sequence in a $[0_2/90_6]_s$ composite containing a surface matrix crack and an internal matrix crack.

the experiments and the predictions was good.

It was interesting to evaluate the contributing fracture modes for the delamination growth in $[0_2/90_6]_s$ panels. Figure 4.26 shows the calculated strain energy release rates of Modes I, II, and III for the laminate containing a small delamination with an internal shear crack and a surface bending crack. For the laminate with the initial bending crack, G_I (Mode I fracture) contributed significantly to the total strain energy release rate along the delamination front near the neighborhood where the matrix cracks intersected with the delamination ($\phi = 0^\circ$ and 90°), indicating that delamination initiation was in mixed modes.

Figure 4.27 shows the calculated strain energy release rates of Modes I, II, and III for the laminate containing a larger delamination with an internal crack and with or without a surface matrix crack. Clearly, Modes II and III fractures dominated the total strain energy release rate for the laminate with and without the surface matrix crack. And it is noted that the total strain energy release rate was only slightly affected by the introduction of the surface crack, indicating that delamination growth was dominated by the internal shear crack.

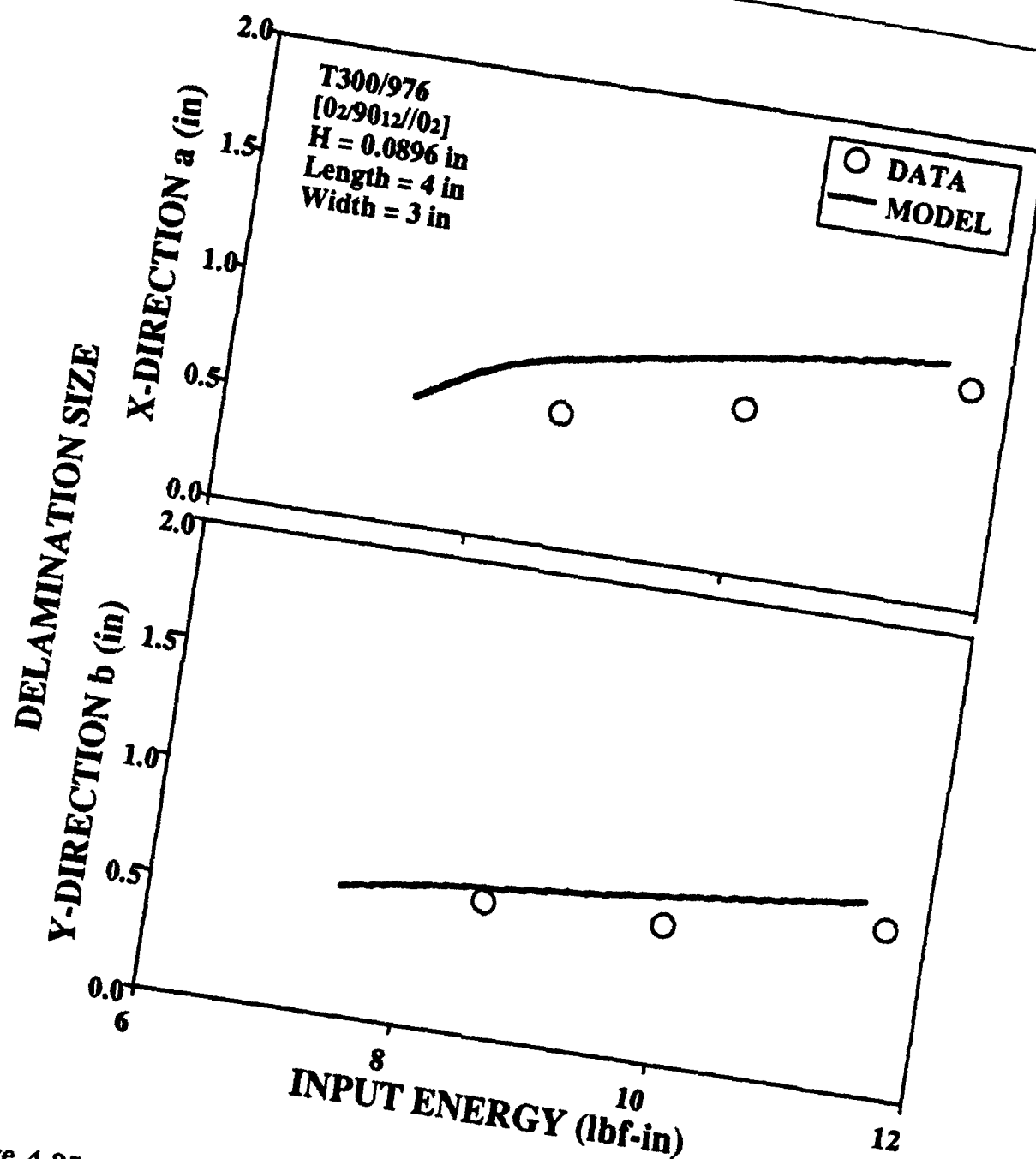


Figure 4.25 The comparison of delamination sizes predicted and measured in a [0₂/90₆]ₛ composite with respect to quasi-impact energy.

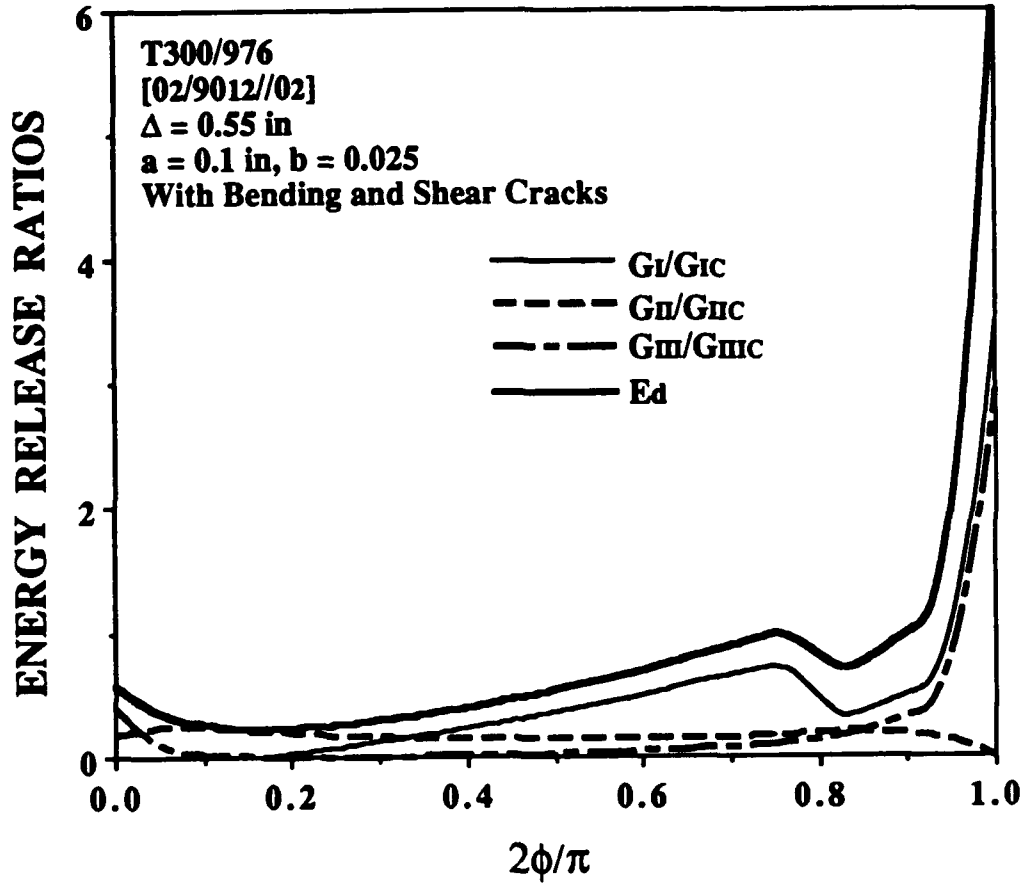


Figure 4.26 Comparison of the calculated strain energy release rates of Modes I, II, and III along a small delamination front in a $[0_2/90_6]_s$ composite containing an internal crack and a surface matrix crack.

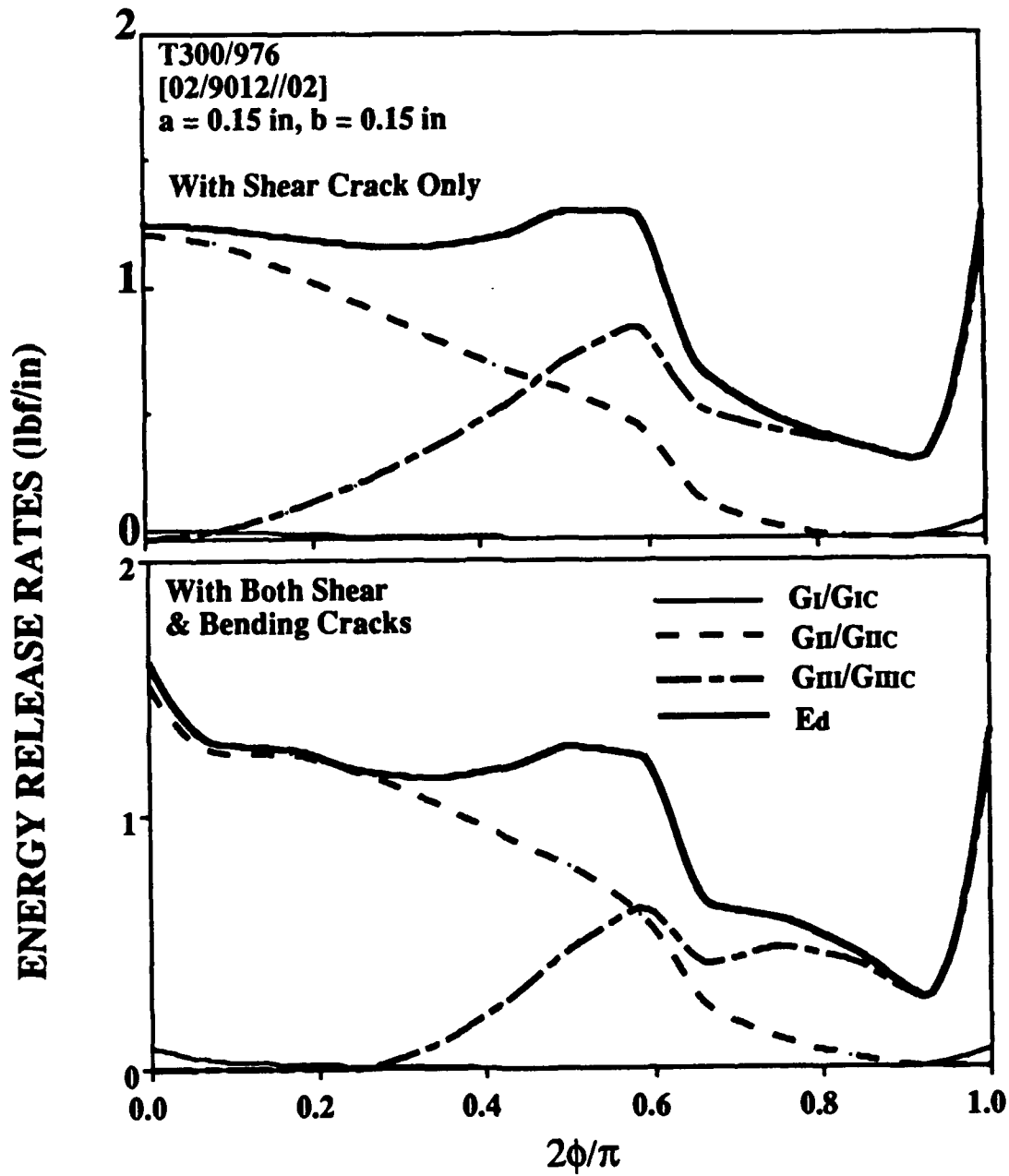


Figure 4.27 Comparison of the calculated strain energy release rates of Modes I, II, and III along a large delamination front in a $[0_2/90_6]_s$ composite containing an internal crack and with or without a surface matrix crack.

T300/976 [0₄/90₄]_s Panels

It has been shown that delamination growth in [0₆/90₂]_s panels was mainly dominated by Mode I fracture, while in [0₂/90₆]_s it was mainly dominated by shear (Mode II and III) fracture. In the following, delamination growth of a [0₄/90₄]_s panel was studied. Again, type 3 and 4 models were considered.

Figure 4.28 shows the sequence of the delamination growth in the laminate with the matrix cracks predicted by the type 3 model. At a fixed indenter displacement, Figure 4.28-1 and Figure 4.28-2 show that the initial delamination grew from a small elliptical shape into a larger elliptical shape along the direction at $\phi = 90^\circ$ with its minor axis perpendicular to the fiber direction of the bottom ply group. Figure 4.28-3 indicates the delamination would begin to expand along its major axis, as the strain energy release rate ratio started to decrease along the delamination front around $\phi = 90^\circ$, and had the highest values at the delamination front around $\phi = 0^\circ$.

Similarly, the delamination ceased to grow along its major or minor axis as the growth index E_d along the delamination front fell to below unity, such as the case shown in Figure 4.28-4. The delamination shape shown in Figure 4.28-4 was an elliptical shape, which agreed with the shape observed in the experiments (see Figure 4.13-c). Figure 4.29 shows the comparisons between the estimated delamination sizes in the x and y directions and the sizes measured from the experiments. The correlation matches reasonably well between the experiments and the predictions.

It was again interesting to investigate the contributing modes to the delamination growth. Figure 4.30 shows the comparisons of the calculated crack growth index E_d for the laminate containing a small elliptical delamination with an internal matrix crack and with or without the surface matrix crack. The upper figure was the case for a small delamination. For the laminate containing the surface matrix crack, the value of E_d along the delamination front near the location of both matrix

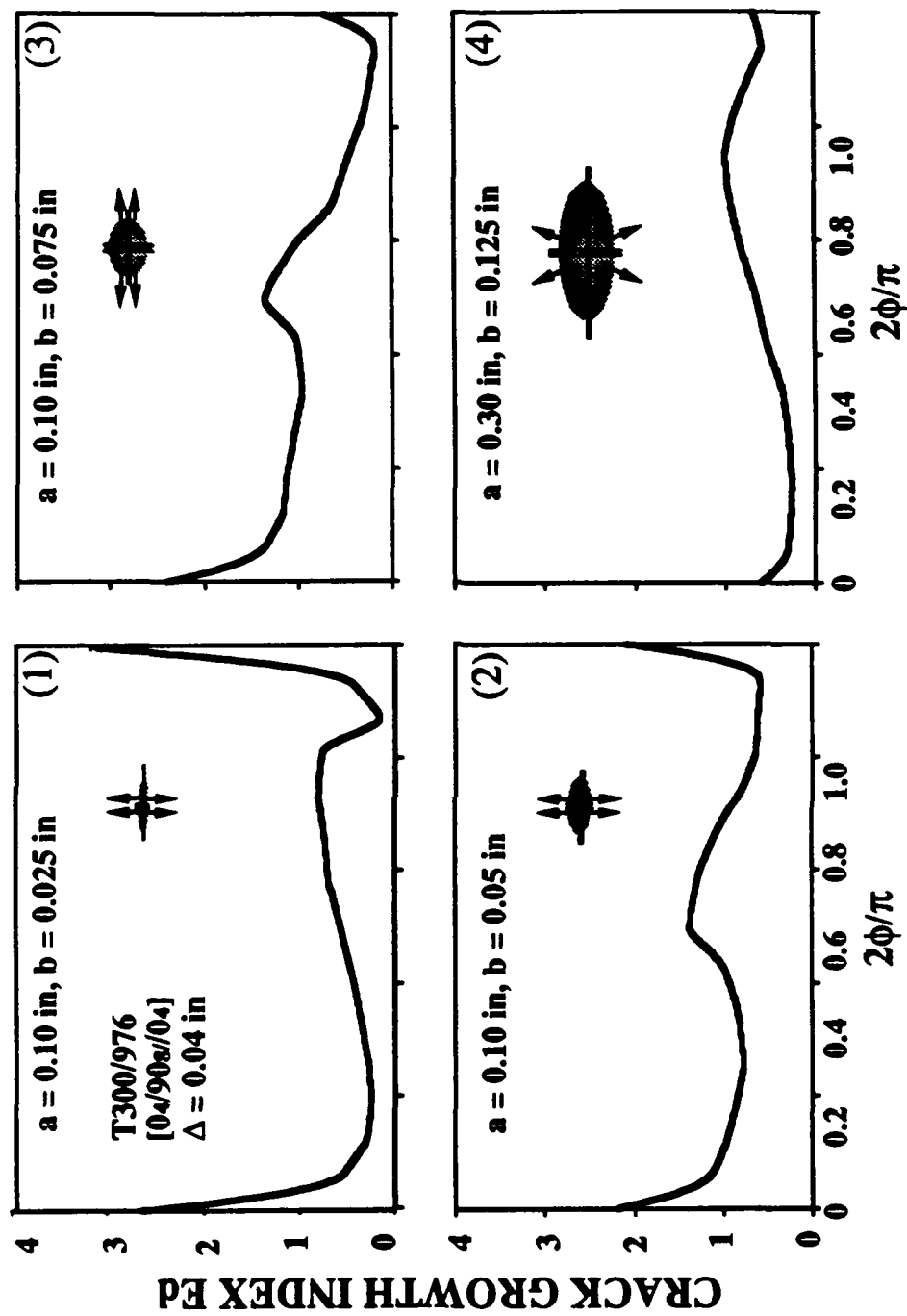


Figure 4.28 The predicted delamination growth sequence in a $[0_4/90_4]_s$ composite containing a surface matrix crack and an internal matrix crack.

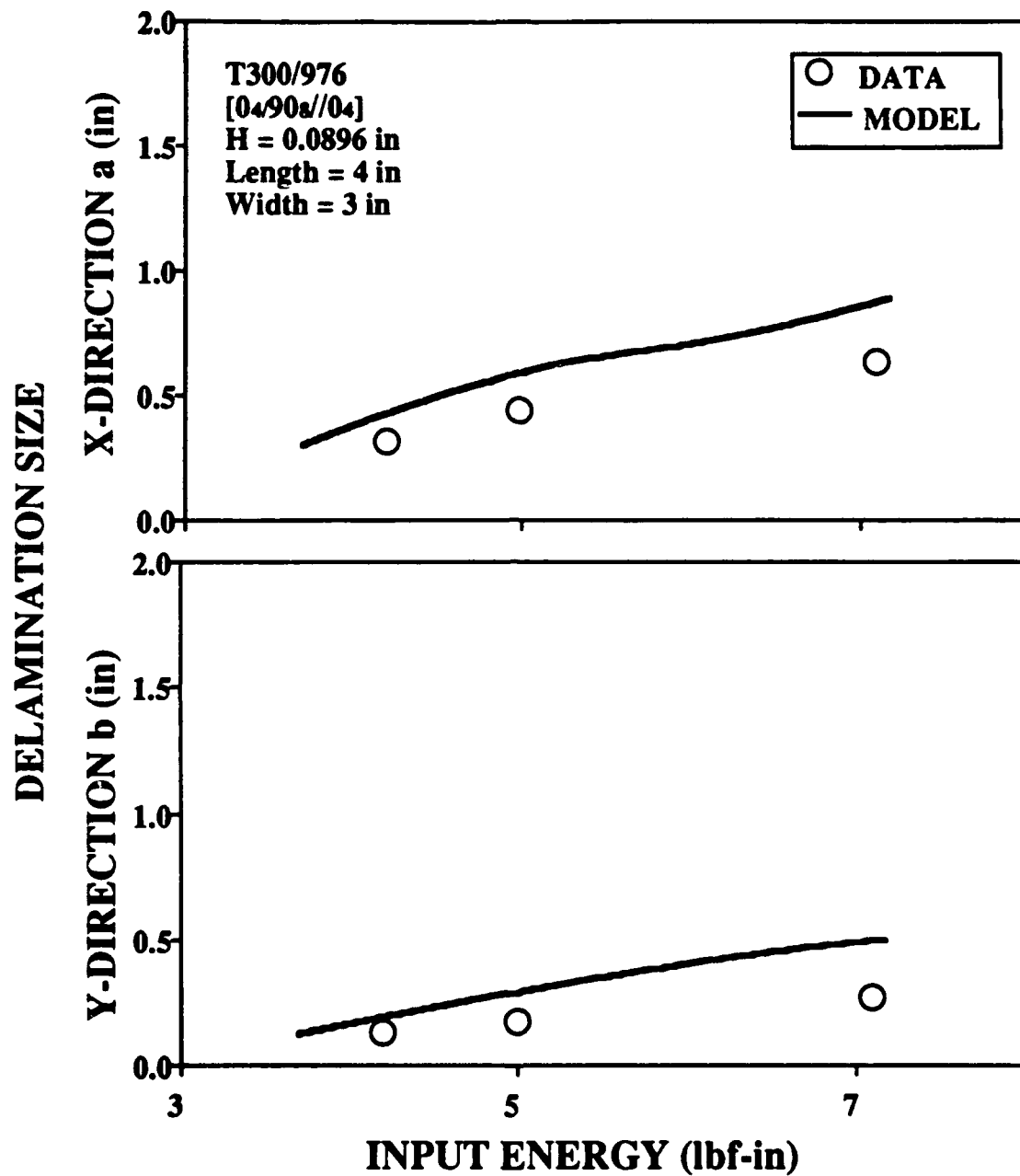


Figure 4.29 The comparison of delamination sizes between the predicted and the measured in a [0₄/90₄]_s composite under a spherical indenter.

cracks increased significantly and reached a peak at the intersections between the matrix cracks and delamination (at $\phi = 0^\circ$, and 90°). The value of E_d , however, decreased rapidly as the delamination front where the value of E_d was calculated moved farther away from the location of the matrix cracks (when ϕ is not around 0° and 90°). Therefore, for a small delamination, the coupling between the matrix cracks and delamination was significant.

A different distribution of the total strain energy release rate was obtained for the laminate containing no pre-introduced matrix crack. Overall, the values of E_d were much smaller than those calculated from the laminate containing the matrix crack. Apparently, the laminate with the surface matrix crack could initiate the delamination at a much earlier loading stage than the one without. Once the delamination propagated, it would grow along with the direction of internal matrix cracking.

However, for moderate and large delaminations such as the case shown in the lower figure of Figure 4.30, the surface crack had limited contribution to the delamination growth. The coupling between the surface matrix crack and the delamination only appeared locally at $\phi = 0^\circ$. Apparently, the effect of the surface matrix crack on the delamination growth decreased significantly as the delamination grew.

It was also interesting to examine the contributing fracture modes for delamination growth when the delamination is small or moderately sized. Figure 4.31 shows the calculated strain energy release rates of Modes I, II, and III for the laminate containing a small delamination with an internal crack and a surface matrix crack. Clearly, for the laminate with a small delamination, G_I (Mode I fracture) contributed significantly to the total strain energy release rate along the delamination front near the neighborhood where the surface matrix crack intersected with the delamination ($\phi = 0^\circ$ and 90°). Generally, the growth for a small delamination

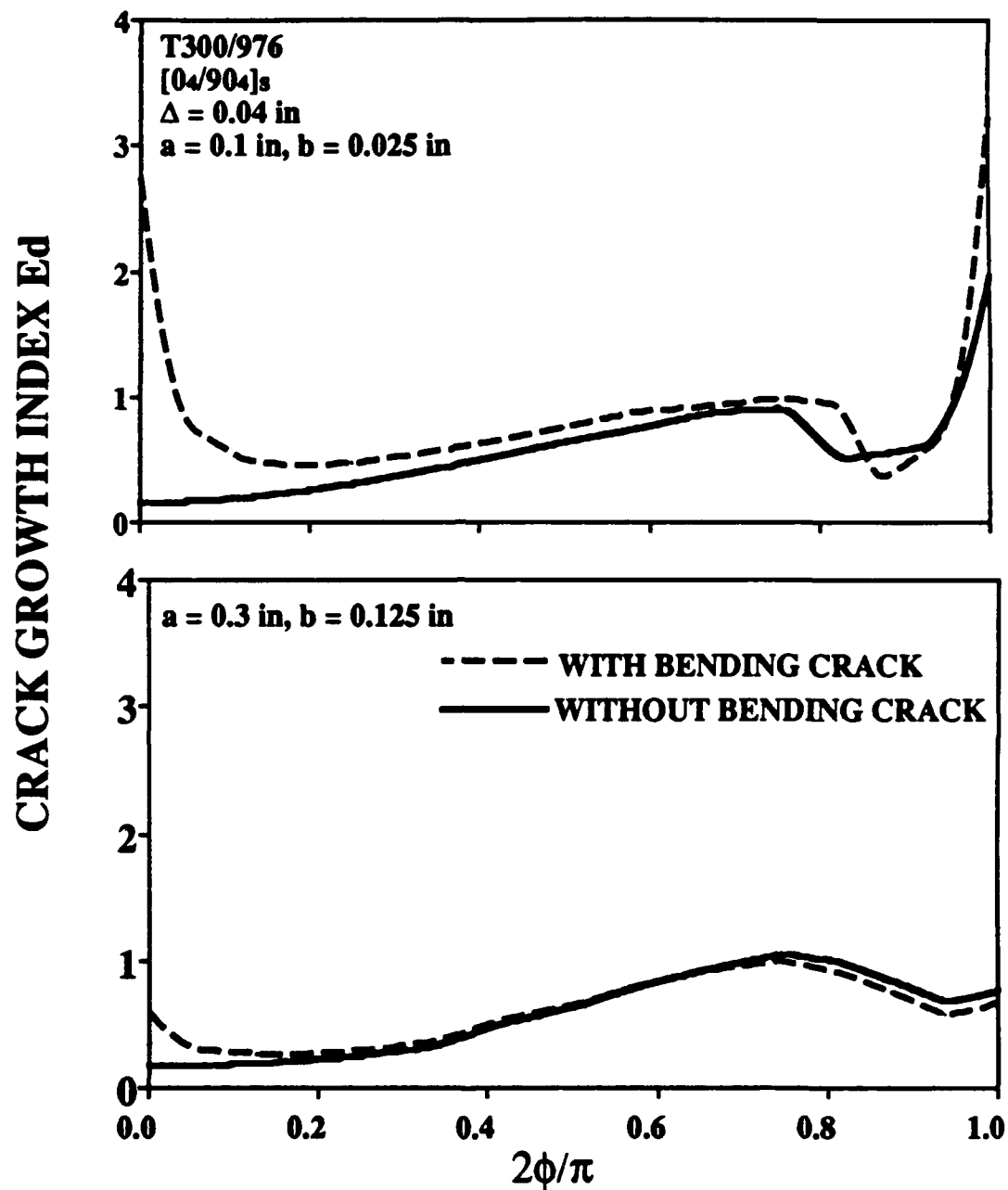


Figure 4.30 The effect of bending crack on the crack growth index E_d for a laminate containing a delamination and a bending and shear crack. Comparison of E_d values between a small and a large delamination in a $[0_4/90_4]_s$ composite.

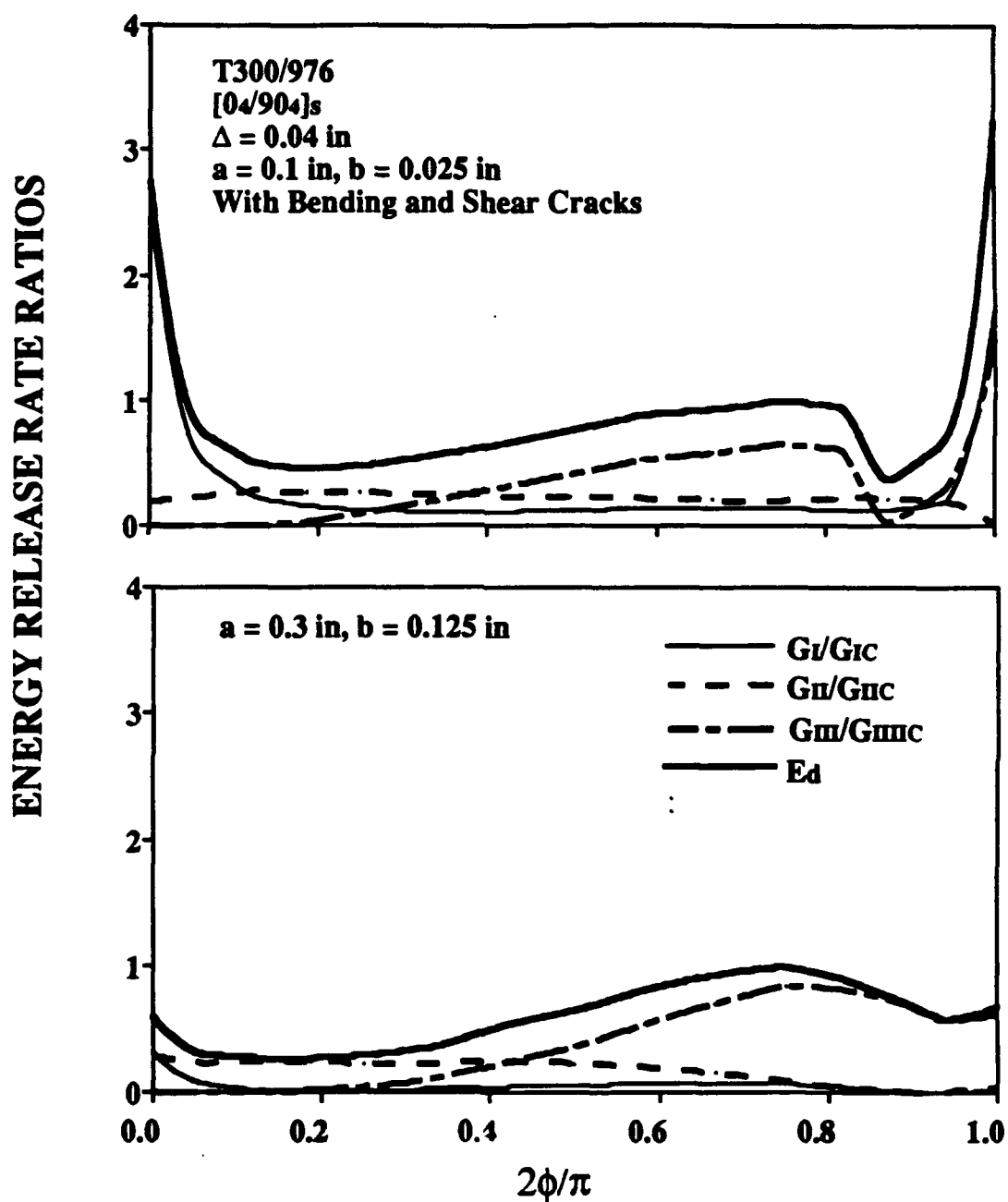


Figure 4.31 The calculated strain energy release rates between a small and a large delamination front in a [0₄/90₄]_s composite containing an internal crack and a surface matrix crack.

was in mixed modes. However, the lower part of Figure 4.31 showed that except in the neighborhood of $\phi = 0^\circ$, the strain energy release rates were only slightly affected by the surface crack. The shear mode fractures (Modes II and III) took the consideration of the largest greatest portion of the total energy release rate, indicating that the delamination growth was dominated by internal matrix cracking and the surface crack effect was minimum.

T800H/3900-2 [0₂/90₆]_s Panels

Numerical simulations were also performed on T800H/3500-2 composites to estimate delamination sizes corresponding to the applied load (energy). The results of the test data on [0₂/90₆]_s are shown in Figure 4.14. Only the type 4 model was used to correlate the predictions and the experiments. The estimated delamination sizes in the x and y directions are presented in Figure 4.14. The comparison between the estimated sizes and the measured sizes agree quite well.

For the purpose of comparison, the estimated results and experimental data for T300/976 panels are also shown in the same figure. It is shown clearly that the panels made of T800/976 have much smaller damage sizes than the panels made of T300/976. It was also observed that the damage shape was much more symmetric than the that in T300/976 panels, indicting the damage growth inside the toughened composites tend to have more stable growth. The reduced damage size is one of the main reasons that contribute to the reported high compressive strength after impact (CAI) for this new material system.

§4.6 Concluding Remarks

A finite element analysis was developed for analyzing cross-ply laminated composite plates subjected to transverse concentrated loading resulting from a spherical indenter. Based on the analysis, the following remarks can be made for the laminates studied:

1. The initial matrix cracking significantly affects the growth of delamination resulting from transverse loading.
2. Matrix cracks enhance delamination growth.
3. Mode I fracture is critical for surface crack-induced delamination growth.
4. Modes II and III shear fracture dominate internal crack induced delamination growth.
5. Matrix cracking must be considered for modeling delamination propagation due to transverse loading.
6. Delamination growth depends on ply orientation.

Additionally, it is noted that the proposed finite element analysis can be extended to study other ply orientations and other loading conditions, such as delamination-buckling.

Appendix A

A 2-D Finite Element Mesh Remodeling Procedure

Before a structure is analyzed or tested, there is no information about where the matrix cracks are to occur or what interfaces are to be delaminated. Here a simple but effective scheme is developed, which can be illustrated by two simple but typical meshes, shown in Figures A.1 and A.2. The first mesh, shown in Figure A.1, is mainly used for $[0_m/90_n]_s$ laminates, for which embedded crack-induced delaminations are the typical damage mode. The second mesh, shown in Figure A.2, is mainly used for $[90_m/0_n]_s$ laminates, for which surface bending crack-induced delamination is the typical damage pattern.

This technique uses the original two-dimensional finite element grid system. In the original mesh, double lines instead of one regular line are used on each interface between elements in the thickness direction or in the span-length direction. In other words, each node is assigned systematically four nodal numbers, instead of one, in the global nodal system. If no damage occurs, all four numbers at each node are assigned the same equation numbers. For example, the four nodes i, j, k, l in Figure A.1 have the same equation numbers if there is no damage introduced at that point. Once a crack is generated, nodes on different sides of the double lines are split and therefore have different equation numbers. For example, as shown in Figure A-1, nodes (E, G) and nodes (F, H) are separated due to the existence of the

vertical matrix crack, while two nodes E and G (same for F and H) are assigned the same equation numbers. For some corner points such as (A, B, C, D) , where the delamination and the matrix crack intersect, (A, B, D) are assigned the same equation number. C remains independent.

As the matrix cracks and delaminations may intersect, one needs to apply the contact condition to the intersection points (such as C and J) to prevent the overlapping of the matrix crack and the delamination surfaces. Therefore, five degrees of freedom need to be assigned to each node. The first three are for displacements in x_1 , x_2 , and x_3 directions. The fourth is used for a Lagrange multiplier for possible delaminations and the fifth is used for a Lagrange multiplier for possible matrix cracks.

By this technique, matrix cracking can be easily simulated wherever it occurs, as the interface only needs to be split between two elements and the crack is introduced without much difficulty. This is also true for delamination modeling.

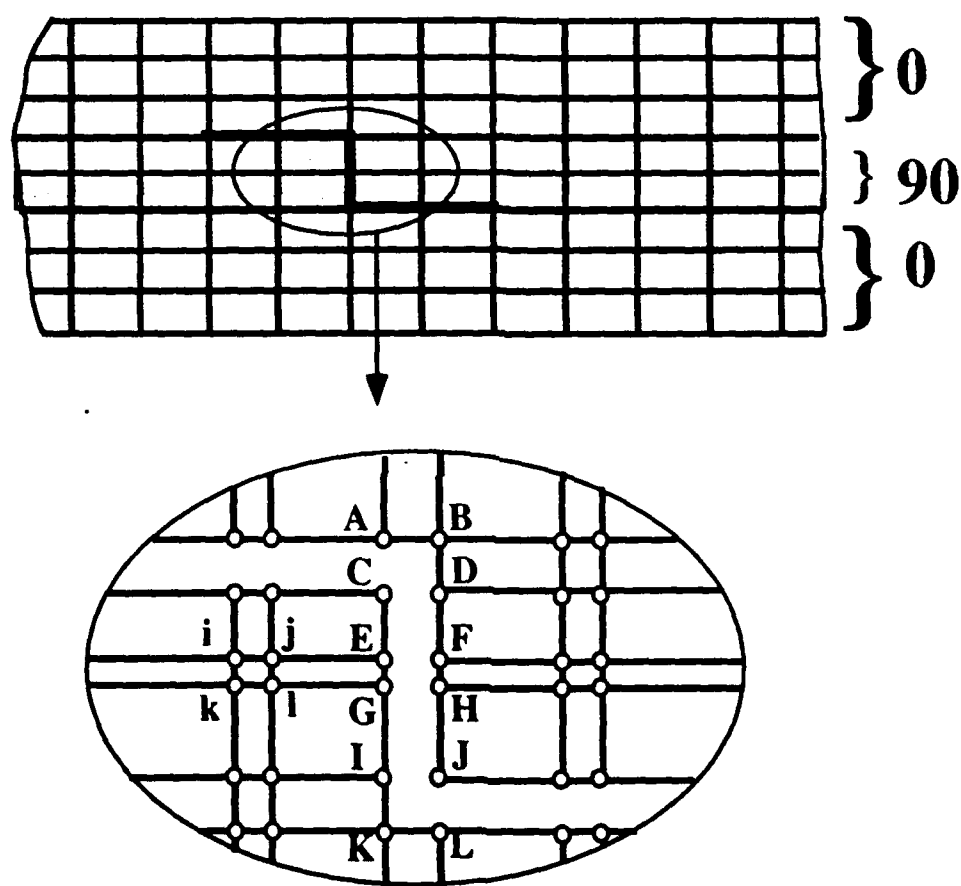


Figure A.1 A typical mesh used in the analysis for modeling shear matrix crack induced delaminations in two dimensions.

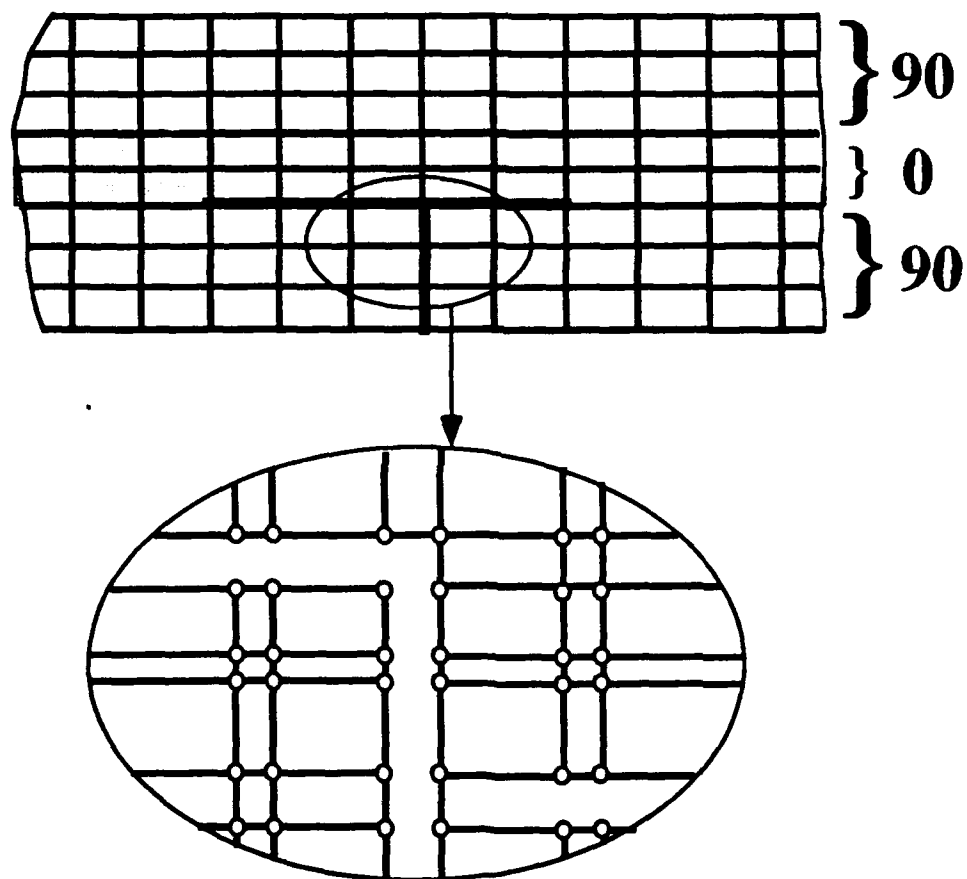


Figure A.2 A typical mesh used in the analysis for modeling bending matrix crack induced delamination in two dimensions.

Appendix B

Contact Residual and Stiffness of a 2-D Contact Element

In order to assure quadratic convergence of Newton's method, it is essential to derive a consistent tangent matrix in linearizing the nonlinear finite element equation. In the following, a contact element consisting of one slave node and two master nodes is derived. The derivation is in a vector and tensor form. In order to make the implementation easier, matrix expressions are derived for contact residual and consistent contact tangent stiffness matrix.

By referring to Figure B.1, the contact gap associated with a typical slave node s is given by a simple form

$$g = \mathbf{n} \cdot (\mathbf{x}_s - \mathbf{x}_1) \quad (B.1)$$

where \mathbf{n} is the normal of contact point c on master segment 1 – 2. It is worthwhile to note that the normal is unique for master segment 1 – 2. To obtain an explicit expression for the residual and contact stiffness in Eq. (4.20) and Eq. (3.36), the variation δg must be performed. In the fully nonlinear case, the change in the normal vector \mathbf{n} needs to be considered. As $\mathbf{n} = \mathbf{e}_2 \times \mathbf{e}_1$, the change in the vector \mathbf{e}_1 also needs to be considered. The tangent \mathbf{e}_1 is given by $\mathbf{e}_1 = (\mathbf{x}_2 - \mathbf{x}_1)/\|\mathbf{x}_2 - \mathbf{x}_1\|$.

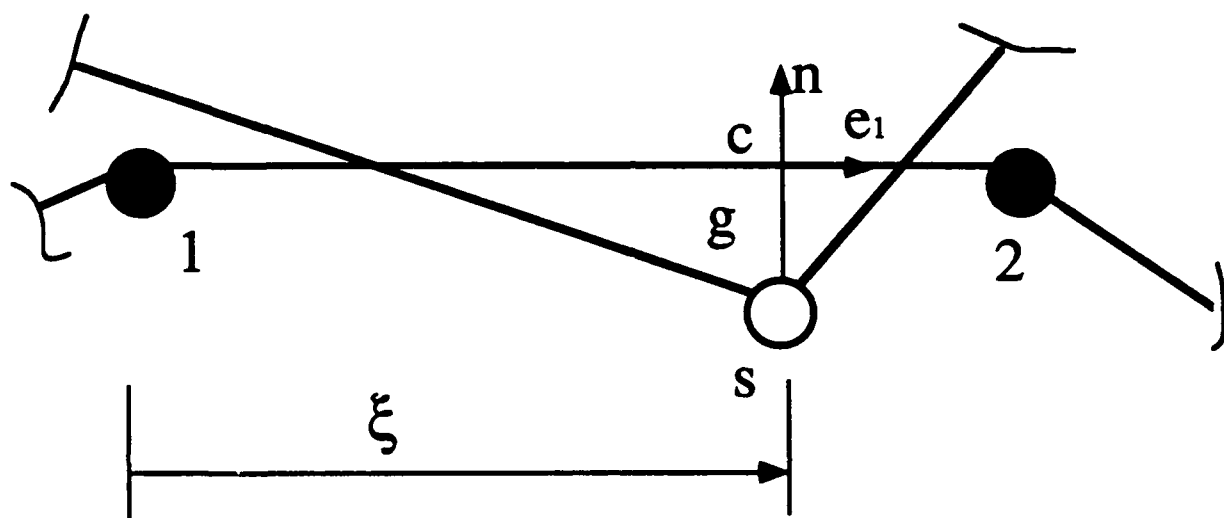


Figure B.1 Geometry of a slave node s with a master segment 1-2.

By using the chain rule, the variation of \mathbf{e}_1 is given as

$$\delta \mathbf{e}_1 = \frac{1}{\|\mathbf{x}_2 - \mathbf{x}_1\|^2} [(\delta \mathbf{x}_2 - \delta \mathbf{x}_1) \|\mathbf{x}_2 - \mathbf{x}_1\| - (\mathbf{x}_2 - \mathbf{x}_1) \delta \|\mathbf{x}_2 - \mathbf{x}_1\|] \quad (B.2)$$

Recalling $\|\mathbf{x}_2 - \mathbf{x}_1\| = [(\mathbf{x}_2 - \mathbf{x}_1) \cdot (\mathbf{x}_2 - \mathbf{x}_1)]^{1/2}$, the following is obtained:

$$\delta \|\mathbf{x}_2 - \mathbf{x}_1\| = \frac{(\mathbf{x}_2 - \mathbf{x}_1) \cdot (\delta \mathbf{x}_2 - \delta \mathbf{x}_1)}{\|\mathbf{x}_2 - \mathbf{x}_1\|} \quad (B.3)$$

Therefore

$$\delta \mathbf{e}_1 = \frac{1}{\|\mathbf{x}_2 - \mathbf{x}_1\|} [(\delta \mathbf{x}_2 - \delta \mathbf{x}_1) - (\mathbf{x}_2 - \mathbf{x}_1) \frac{(\mathbf{x}_2 - \mathbf{x}_1)}{\|\mathbf{x}_2 - \mathbf{x}_1\|^2} \cdot (\delta \mathbf{x}_2 - \delta \mathbf{x}_1)] \quad (B.4)$$

or

$$\delta \mathbf{e}_1 = \frac{1}{\|\mathbf{x}_2 - \mathbf{x}_1\|} [\mathbf{I} - \mathbf{e}_1 \mathbf{e}_1 \cdot (\delta \mathbf{x}_2 - \delta \mathbf{x}_1)] \quad (B.5)$$

or

$$\delta \mathbf{e}_1 = \frac{1}{\|\mathbf{x}_2 - \mathbf{x}_1\|} (\mathbf{I} - \mathbf{e}_1 \otimes \mathbf{e}_1) (\delta \mathbf{x}_2 - \delta \mathbf{x}_1) \quad (B.6)$$

or

$$\delta \mathbf{e}_1 = \frac{1}{\|\mathbf{x}_2 - \mathbf{x}_1\|} (\mathbf{n} \otimes \mathbf{n}) (\delta \mathbf{x}_2 - \delta \mathbf{x}_1) \quad (B.7)$$

where $\mathbf{n} \otimes \mathbf{n} + \mathbf{e}_1 \otimes \mathbf{e}_1 = \mathbf{I}$ is used. The symbol \otimes denotes tensor product. Also, the variation of \mathbf{n} gives the expression:

$$\delta \mathbf{n} = \delta \mathbf{e}_2 \times \mathbf{e}_1 + \mathbf{e}_2 \times \delta \mathbf{e}_1 = \mathbf{e}_2 \times \delta \mathbf{e}_1 \quad (B.8)$$

or

$$\delta \mathbf{n} = \mathbf{e}_2 \times \frac{1}{\|\mathbf{x}_2 - \mathbf{x}_1\|} (\mathbf{n} \otimes \mathbf{n}) (\delta \mathbf{x}_2 - \delta \mathbf{x}_1) \quad (B.9)$$

Recalling $\mathbf{e}_2 \times \mathbf{n} = -\mathbf{e}_1$, the following is obtained:

$$\delta \mathbf{n} = -\frac{1}{\|\mathbf{x}_2 - \mathbf{x}_1\|} (\mathbf{e}_1 \otimes \mathbf{n}) (\delta \mathbf{x}_2 - \delta \mathbf{x}_1) \quad (B.10)$$

The variation of the gap g therefore can be derived as follows:

$$\delta g = (\delta \mathbf{x}_s - \delta \mathbf{x}_1) \cdot \mathbf{n} + (\mathbf{x}_s - \mathbf{x}_1) \cdot \delta \mathbf{n} \quad (B.11)$$

or

$$\delta g = [(\delta \mathbf{x}_s - \delta \mathbf{x}_1) \cdot \mathbf{n} - \frac{(\mathbf{x}_s - \mathbf{x}_1)}{\|\mathbf{x}_2 - \mathbf{x}_1\|} (\mathbf{e}_1 \otimes \mathbf{n}) (\delta \mathbf{x}_2 - \delta \mathbf{x}_1)] \quad (B.12)$$

or

$$\delta g = [(\delta \mathbf{x}_s - \delta \mathbf{x}_1) \cdot \mathbf{n} - \frac{(\mathbf{x}_s - \mathbf{x}_1)}{\|\mathbf{x}_2 - \mathbf{x}_1\|} \cdot \mathbf{e}_1 \mathbf{n} \cdot (\delta \mathbf{x}_2 - \delta \mathbf{x}_1)] \quad (B.13)$$

It is observed that $(\mathbf{x}_s - \mathbf{x}_1)/\|\mathbf{x}_2 - \mathbf{x}_1\| \cdot \mathbf{e}_1$ appearing in Eq. (B.13) is exactly the line coordinate ξ , as can be seen from Figure B.1. The contact node is projected onto line 1-2 and interpolated in terms of \mathbf{x}_1 and \mathbf{x}_2 as $\mathbf{x}_c = (1 - \xi)\mathbf{x}_1 + \xi\mathbf{x}_2$. Therefore δg is rewritten as

$$\delta g = (\delta \mathbf{x}_s - (1 - \xi)\delta \mathbf{x}_1 - \xi\delta \mathbf{x}_2) \cdot \mathbf{n} \quad (B.14)$$

or

$$\delta g = \delta(\mathbf{x}_s - \mathbf{x}_c) \cdot \mathbf{n} \quad (B.15)$$

The total differential of δg can be written as

$$d(\delta g) = d[\delta(\mathbf{x}_s - \mathbf{x}_c)] \cdot \mathbf{n} + \delta(\mathbf{x}_s - \mathbf{x}_c) \cdot d\mathbf{n} \quad (B.16)$$

where the second term on the RHS side of the Eq. (B.16) is simple to find. The first term of the RHS side of the Eq. (B.16) is

$$d[\delta(\mathbf{x}_s - \mathbf{x}_c)] \cdot \mathbf{n} = -d(\mathbf{x}_c) \cdot \mathbf{n} = -(\delta \mathbf{x}_{c,\xi} d\xi) \cdot \mathbf{n} \quad (B.17)$$

By the definition of \mathbf{x}_c in terms of \mathbf{x}_1 and \mathbf{x}_2 (that is, $\mathbf{x}_c = (1 - \xi)\mathbf{x}_1 + \xi\mathbf{x}_2$), the following is obtained:

$$\delta \mathbf{x}_{c,\xi} = \delta \mathbf{x}_2 - \delta \mathbf{x}_1 \quad (B.18)$$

The differential of $\xi = (\mathbf{x}_s - \mathbf{x}_1)/\|\mathbf{x}_2 - \mathbf{x}_1\| \cdot \mathbf{e}_1$ is derived by chain rule as

$$d\xi = \frac{1}{\|\mathbf{x}_2 - \mathbf{x}_1\|^2} \left[g \mathbf{n} \cdot (d\mathbf{u}_2 - d\mathbf{u}_1) + d\mathbf{e}_1 \cdot (d\mathbf{u}_s - d\mathbf{u}_c) \right] \quad (B.19)$$

With all the information provided above, the total differential of δg can be derived as

$$d(\delta g) = - \frac{1}{\|\mathbf{x}_2 - \mathbf{x}_1\|} \left\{ \begin{aligned} & \delta(\mathbf{u}_s - \mathbf{u}_c) \cdot (\mathbf{e}_1 \otimes \mathbf{n})(d\mathbf{u}_2 - d\mathbf{u}_1) \\ & - \delta(\mathbf{u}_s - \mathbf{u}_c) \cdot (\mathbf{e}_1 \otimes \mathbf{n})(d\mathbf{u}_2 - d\mathbf{u}_1) \\ & + \frac{g}{\|\mathbf{x}_2 - \mathbf{x}_1\|} d(\mathbf{u}_2 - \mathbf{u}_1) \cdot (\mathbf{n} \otimes \mathbf{n})(\delta\mathbf{u}_s - \delta\mathbf{u}_c) \end{aligned} \right\} \quad (B.20)$$

The consistent contact stiffness then follows from the identity

$$d(\delta g) = d\mathbf{u}^M \frac{\partial^2 g}{\partial \mathbf{u}^M \partial \mathbf{u}^N} \delta \mathbf{u}^N \quad (B.21)$$

From the virtual work linearization, the contact stiffness can be written as

$$\mathbf{k}_c = \lambda \frac{\partial}{\partial \mathbf{u}^N} \left(\frac{\partial g}{\partial \mathbf{u}^M} \right) \quad (B.22)$$

And the contact residual force of the element is

$$\mathbf{f}_c = \lambda \frac{\partial g}{\partial \mathbf{u}^M} \quad (B.23)$$

In the following, explicit matrix expressions are derived for a single slave node in contact with the master segment. Based on these matrices, a standard assembly procedure can be used to add the contact contributions of each contact node to global tangent stiffness and residual. In this process, the change of the profile or bandwidth must be taken into account.

The following vectors are now introduced:

$$\left. \begin{aligned} \mathbf{N}^T &= \{-(1-\xi)\mathbf{n}, -\xi\mathbf{n}, \mathbf{n}\} \\ \mathbf{T}^T &= \{-(1-\xi)\mathbf{e}_1, -\xi\mathbf{e}_1, \mathbf{e}_1\} \\ \mathbf{U}^T &= \{-\mathbf{n}, \mathbf{n}, 0\} \\ d\mathbf{u} &= \{d\mathbf{u}_1, d\mathbf{u}_2, d\mathbf{u}_s\} \end{aligned} \right\} \quad (B.24)$$

where \mathbf{n} and \mathbf{e}_1 are shown in Figure B.1. The nodal values $d\mathbf{u}_1$, $d\mathbf{u}_2$, and $d\mathbf{u}_s$ of the displacement increments associated with the three nodes (1, 2, s) are involved in the contact of a single slave node with a master segment. With the definition of these vectors, the contact residual and stiffness are given respectively as

$$\mathbf{f}_c = \lambda \mathbf{N} \quad (B.25)$$

and

$$\mathbf{k}_c = -\frac{\lambda}{\|\mathbf{x}_2 - \mathbf{x}_1\|} (\mathbf{U}\mathbf{T}^T + \mathbf{T}\mathbf{U}^T) \quad (B.26)$$

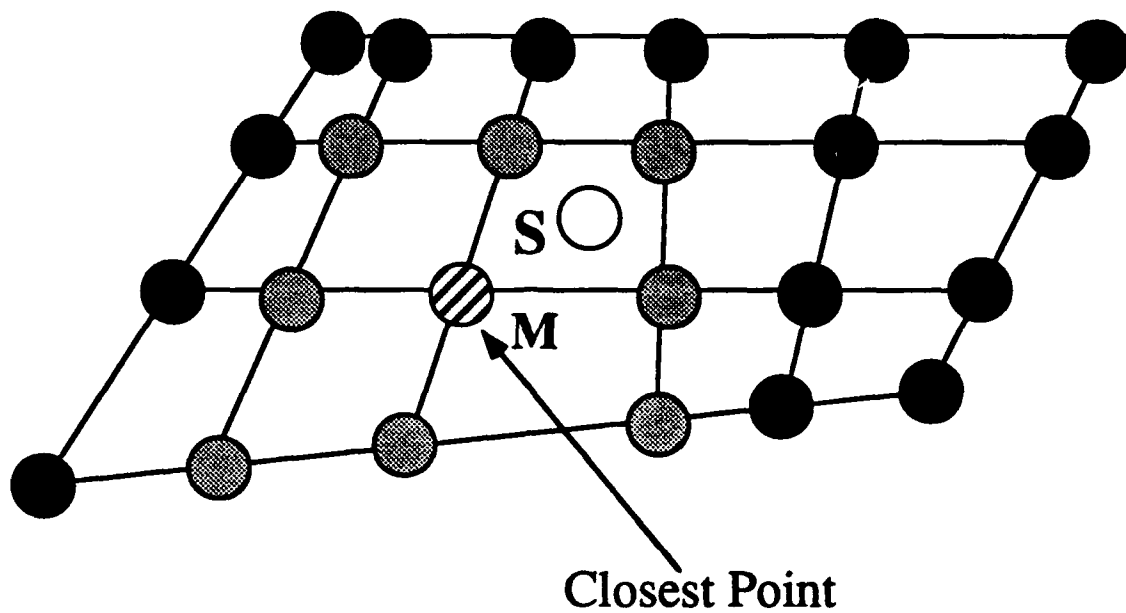
Appendix C

Symmetry Treatment and Contact Node Search Strategy

In a finite element setting, given the slave node, the contact search problem is to search for the closest projection onto the master surface. There are three steps to take for the search. The first step is to determine which master node is closest to the slave node. In computer science, this first step is often referred to as the “nearest neighbor problem”[64]. The second step is to determine which of the master segments, having the master node as one of their vertices, is closest to the slave node. The third step is to determine the closest point of the master segment to the slave node in the biunit domain.

The most obvious but most expensive method for the nearest neighbor problem is the global search, which is to simply check the distance between a given slave node and each master node, and choose the master node with the minimum. However, a simple local search method developed by Benson and Hallquist was adopted here [64]. The idea was to take advantage of the elemental connectivity associated with the finite element method. This is briefly outlined in Figure C.1.

Assume that at time t^n the closest master node M to the given slave node S is known. It is easy to find a short list of potential new master nodes for the next load step in the immediate neighborhood of M by simply checking the elemental connectivity. The list of candidate nodes is generated by considering all of the nodes



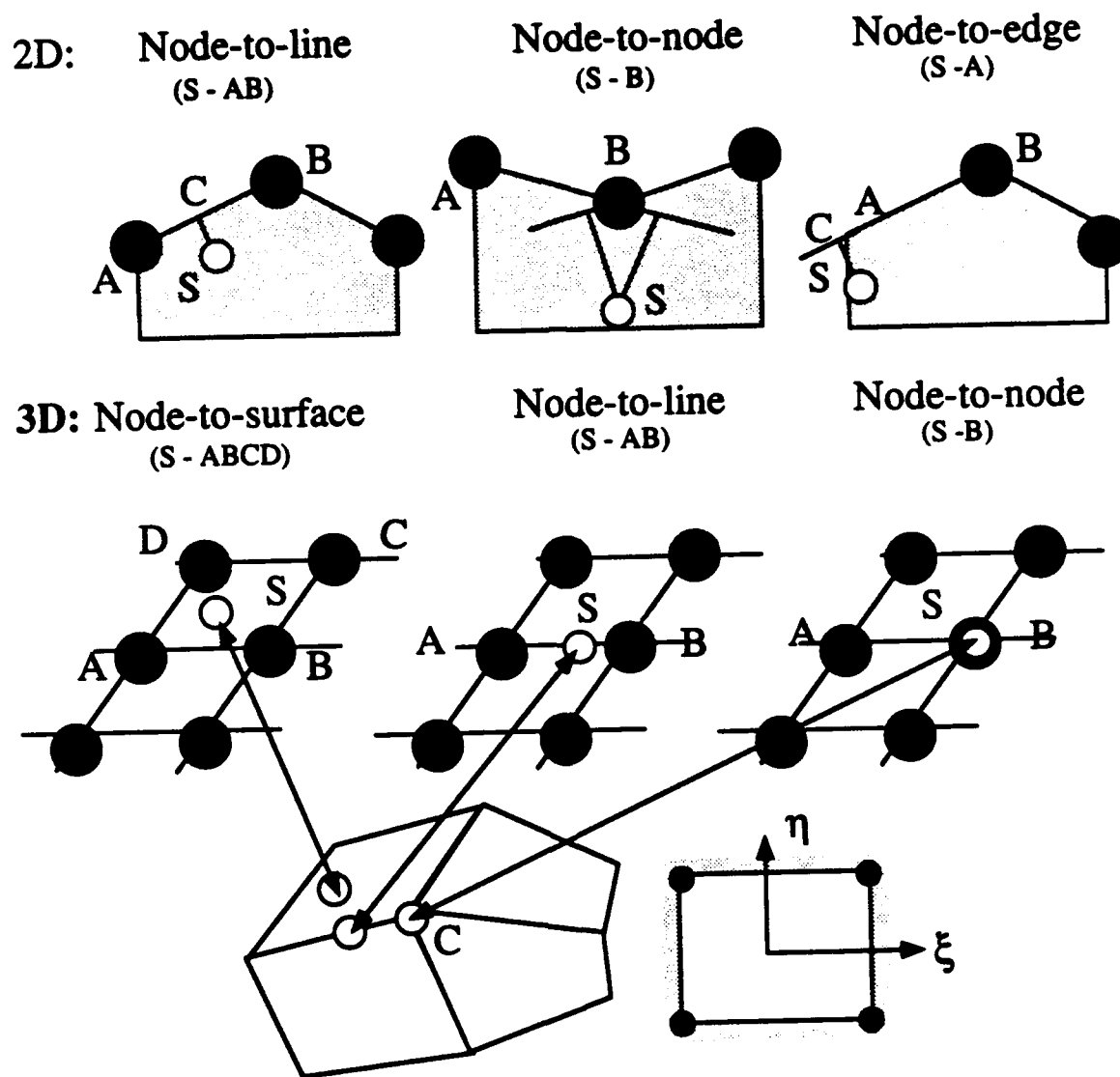
- : Regular master nodes
- ⊗ : Potential closest points for next step
- ▨ : Current closest point corresponding to slave node S
- : The slave node

Figure C.1 Description of a local search technique.

defining the vertices of all of the master segments having M as a vertex. The assumption behind this idea is that during each time step, the relative sliding between the slave node and the neighborhood is not more than some accountable size, such as the element size. The new neighbor search is updated in a new time step. The search always needs to find the closest node to the slave node in its neighborhood. Searching a small neighborhood is computationally much cheaper than searching all the nodes. Generally, at the initial time step, a global search is performed for the initial nearest neighbor. The search neighborhood is updated appropriately as the slave node moves over the master surface since the neighborhood is defined in terms of the last nearest neighbor. The strategy works well in most situations.

After determining the nearest neighbor, the exact segment onto which the slave node is projected needs to be determined. This step is called local search, which is very expensive as it is generally associated with nonlinear iterations. In general, there are several surface segments attached to the nearest neighbor corresponding to the slave node. As there may exist corners, edges, and complicated curvatures at the nearest neighbor, the following strategy is considered.

For all the potential segments attached to the nearest neighbor on the master surface, first calculate the parent domain parameters (ξ_c, η_c) for all the segments. Then, determine one segment with the minimum (ξ_c, η_c) , therefore with the minimum gap g . However, it is not guaranteed that (ξ_c, η_c) will fall into the biunit domain. Depending on where the nearest neighbor is located, and depending on the local curvature, the potential contact element types can be one of the following three: node-to-surface contact element, node-to-line contact element, or node-to-node contact element (see Figure C.2). In the following, the problem is discussed in terms of the geometric location of the nearest neighbor and the location of the projected node in terms of parent domain.

**Figure C.2** Description of contact element types.

In general, the contact region for each delamination is unknown before solving the equilibrium equation. Therefore, an assumption must be made for the contact region of each delamination. The best approximation is to assume that the contact region will remain the same before and after deformation. This means that the contact region, which is known at the previous iteration, is going to be the same for the current iteration. This assumption allows us to solve the equilibrium equation for the displacement. Following each solution, the validity of the assumption for the contact region must be checked. Some portions of the delamination may no longer be in contact, or the portions that were not in contact may now be in contact.

The first step in the determination of the contact region is to find the position of each slave node with respect to its master element in the parent domain, which is essential for both gap calculations and for judging what type of contact is established between the slave node and the master segment.

In order to calculate the gap, the coordinates (ξ_c, η_c) of the point c on some master segment must be calculated. There are several elements attached to the nearest neighbor. Therefore (ξ_c, η_c) must be calculated for each of these elements. The contact point is defined on the master segment as the point closest to the slave node and is calculated by strictly solving a minimization problem. The inequality constraints that bound the isoparametric coordinates between -1 and +1 are not explicitly imposed. If the solution of the unconstrained problem lies outside the permissible range, the node is usually considered not in contact with the segment. The function to be minimized is denoted J , the location of the slave node is \mathbf{x}_c , and the vector to the isoparametric slave segment is \mathbf{x}_s . The problem is stated as

$$\left. \begin{aligned} \text{Min : } J &= \frac{1}{2}(\mathbf{x}_s - \mathbf{x}_c)(\mathbf{x}_s - \mathbf{x}_c), \\ J_{,\xi} &= \mathbf{e}_1 \cdot (\mathbf{x}_s - \mathbf{x}_c) = 0, \\ J_{,\eta} &= \mathbf{e}_2 \cdot (\mathbf{x}_s - \mathbf{x}_c) = 0 \end{aligned} \right\} \quad (C.1)$$

An explicit solution of these equations is very cumbersome and therefore they are solved numerically using Newton's method. Numerical tests suggest that in cases where elements are not distorted, two iterations are sufficient to obtain an engineering accuracy, as a good guess always exists from the previous solution step. However, the method diverges with distorted elements unless the initial guess is accurate. A fast, robust and reasonably accurate approximate contact point calculation [64] was used because of the instability of the Newton-Raphson method. An exact contact point calculation is critical in the delamination contact problem to prevent the solution from oscillating divergence when locating the contact point. Two to three iterations with a least-squares projection were used to generate an initial guess [64].

After finding the (ξ_c, η_c) , the following tests need to be applied:

1. The Contact Gap Test:

The slave node s may stay away from its master element (Figure C.4.a) if

$$g \geq \epsilon_g \quad (C.2)$$

is satisfied, where ϵ_g is the extending tolerance that is used to overcome numerical errors in the calculation of the gap g and to extend the parent domain to overcome the discontinuous slope between elements. In this case, the slave node s is not in contact with its master element. If the slave node s were in contact with its master element previously, then the contact would be released without applying the contact force test. In this case, the value of the contact force for the master element of that slave node is set to zero. If two delamination surfaces are not in contact, there are no surface tractions on the delamination surface.

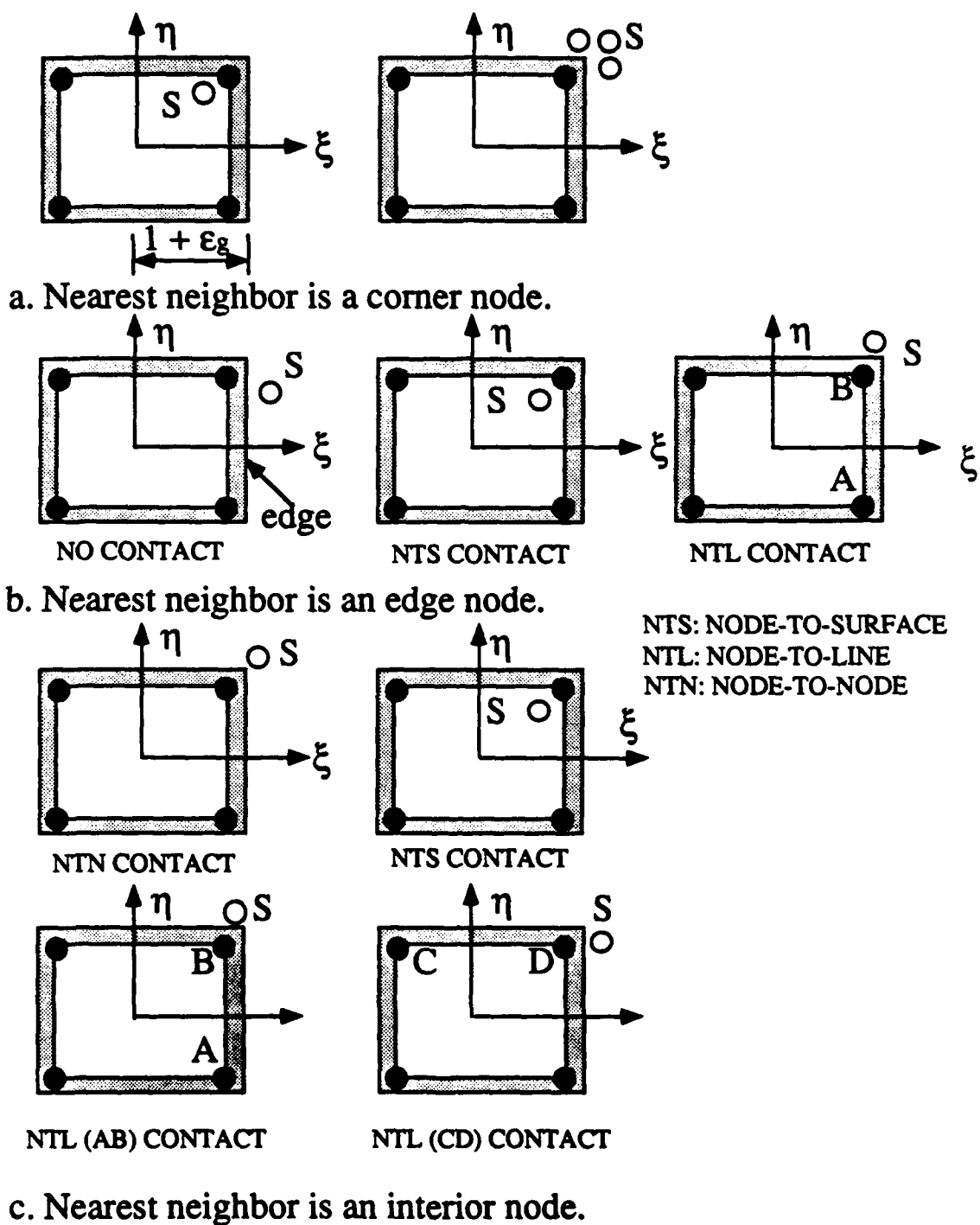


Figure C.3 All the possible locations of a slave node with respect to a master element in the contact search.

The slave node s may penetrate into its master element (Figure C.4.b) if

$$g \leq 0 \quad (C.3)$$

is satisfied. If the slave node s penetrates into its master element, contact is established without applying the contact force test.

2. The Contact Force Test:

The contact force test is applied if

$$0 < |g| < \epsilon_g \quad (C.4)$$

If two delamination surfaces are in contact, then the contact forces must be compressive. If the nodal contact force at slave node number s is found to be tensile, then the slave node must no longer be in contact and it is released. In this case, the value of the Lagrange multiplier for the master element of that slave node is set to zero.

3. The Geometric Contact Check to Determine Potential Contact Element Type:

If there is overlapping, the following checks must be made to evaluate what type of contact element is required:

(a). Nearest neighbor is a corner node on the master surface (Figure C.3.a).

The slave node s may project onto the master element (Figure C.3.a) if

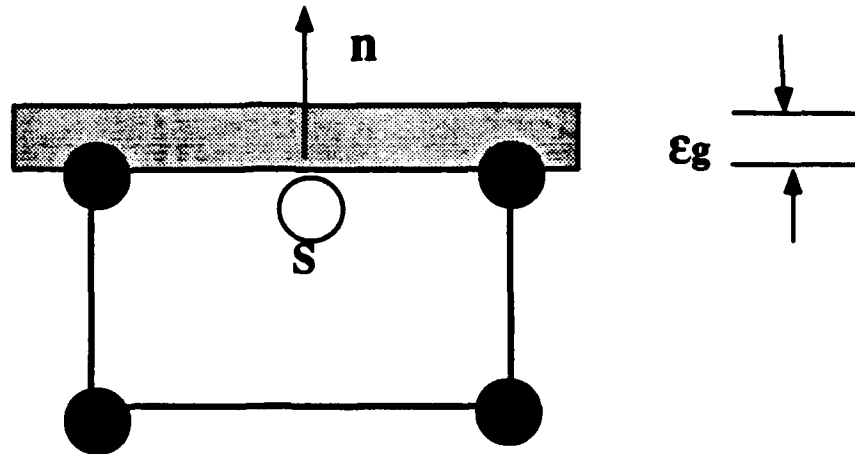
$$|\xi_c| \leq 1 + \epsilon_g, |\eta_c| \leq 1 + \epsilon_g \quad (C.5)$$

Otherwise, no contact occurs for the slave node.

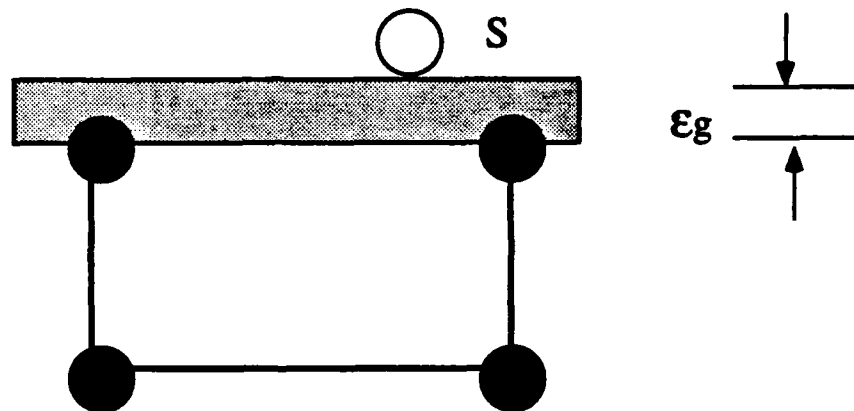
(b). Nearest neighbor is an edge node on the master surface (Figure C.3.b).

Depending on the local coordinates of the master element, there are several cases to be considered. For the coordinates shown in the figure, if

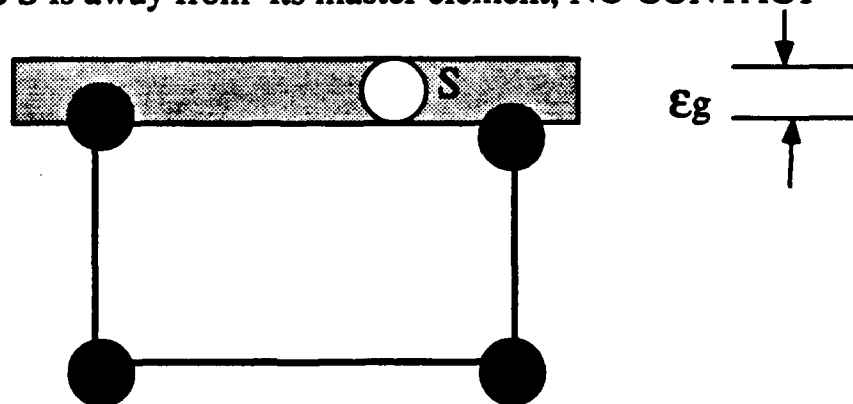
$$|\xi_c| \geq 1 + \epsilon_g \quad (C.6)$$



a. Slave node S is penetrating into its master element; CONTACT



b. Slave node S is away from its master element; NO CONTACT



c. Slave node S is in CONTACT with its master element if contact force is compressive

Figure C.4 Determination of contact according to the position of the slave node with respect to its master element.

no contact occurs. If

$$|\xi_c| \leq 1 + \epsilon_g, |\eta_c| \leq 1 + \epsilon_g \quad (C.7)$$

a node-to-surface contact element may be assumed, depending on the further contact check. If

$$|\xi_c| \leq 1 + \epsilon_g, |\eta_c| > 1 + \epsilon_g \quad (C.8)$$

a node-to-line contact element may be assumed, depending on the further contact check, with line AB .

If the local coordinates reverse in ξ and η , Eq. (C.8) only needs to reverse ξ_c and η_c .

(c). Nearest neighbor is an interior node on the master surface (Figure C.3.c). There are four checks typical for this case, which may result in three different contact elements. If

$$|\xi_c| \leq 1 + \epsilon_g, |\eta_c| \leq 1 + \epsilon_g \quad (C.9)$$

a node-to-surface contact may be assumed. It may result in three different contact elements. If

$$|\xi_c| > 1 + \epsilon_g, |\eta_c| > 1 + \epsilon_g \quad (C.10)$$

a node-to-node contact is assumed, with the closest projection point being the nearest neighbor node. If

$$|\xi_c| > 1 + \epsilon_g, |\eta_c| \leq 1 + \epsilon_g \quad (C.11)$$

a node-to-line contact may be assumed, depending on the further contact check, as some point on line AB is the closest point projection. If

$$|\xi_c| \leq 1 + \epsilon_g, |\eta_c| > 1 + \epsilon_g \quad (C.12)$$

a node-to-line contact may be assumed, depending on the further contact check, as some point on line CD is the closest point projection.

After determining the master segment, the gap g for those node-to-line and node-to-node contact elements must be redefined. The gap and the contact force should also be rechecked.

The implementation of the above treatment is fairly complicated. There is another optional approach to avoid the complicated treatment, though it may fail in some cases. That is, by slightly increasing ϵ_g (i.e., to extend the parent domain), node-to-surface contact elements may be used alone. In most cases, the numerical results differ very slightly from those obtained by the complicated logic. Both options were used alternatively in the simulations.

Appendix D

Contact Residual and Stiffness of a 3-D Contact Element

In this section, attention is restricted to one contact element, realizing that the total contact contribution is merely an assembly of all such active contact elements. The objective is to derive expressions for contact residual \mathbf{f}_c and consistent contact stiffness \mathbf{k}_c . The contact element is defined such that it contains the master nodes of the segment and the active slave node, as shown in Figure D.1. In this figure, the current position of a slave node is given as \mathbf{x}_s , and the master element surface is the element containing its projection \mathbf{x}_c on the master surface. As indicated in the figure, it is assumed that \mathbf{x}_c lies in the continuous interior of the master element surface, as indicated in the figure. The case where \mathbf{x}_c lies on a discontinuous portion of the master surface can occasionally be troublesome. In practice, steps may be taken to avoid this situation by either extending element parameterizations outside the normal domain (i.e., by allowing (ξ, η) to lie slightly outside the biunit square), or by altering the contact element types near corners, edges, and vertices with complicated curvatures such that the closest point projection may be best approximated. In the numerical verification the two approaches were used alternatively, with the former and less costly approach being preferred.

First consider a four node quadrilateral segment of arbitrary shape. From this the three node triangular version can be easily derived. If defining standard

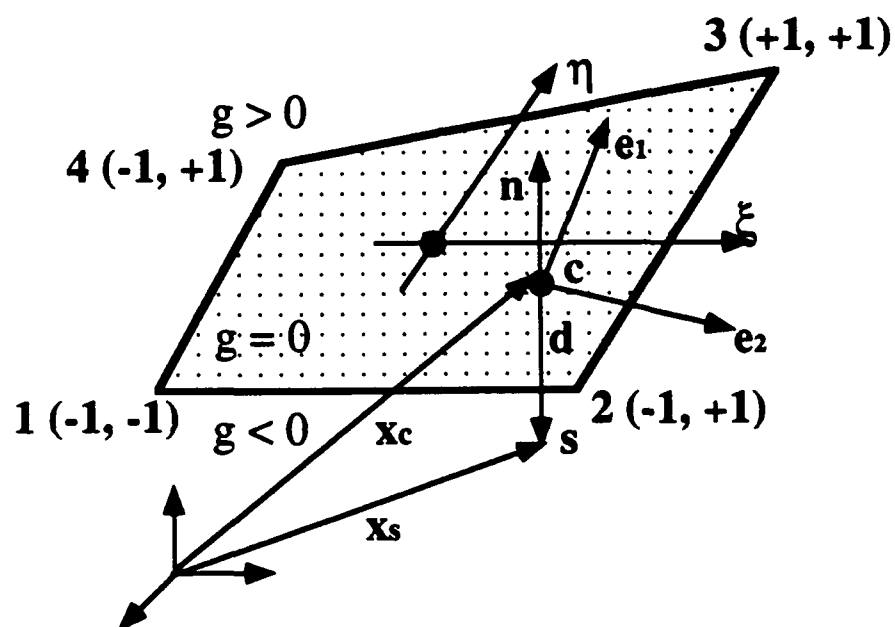


Figure D.1 Projection of slave point x_c onto the discrete master surface.

isoparametric shape functions on the biunit square (for 3-D problem), the following isoparametric interpolation of the geometry of the master segment can be assumed as

$$\mathbf{x} = \sum_{a=1}^{n_{en}} \psi_a \mathbf{x}^a = \psi_a \mathbf{x}^a \quad (D.1)$$

where \mathbf{x}^a denotes the position vector of a master node and ψ_a ($a = 1 - 4$) are the familiar bi-linear interpolation functions defined as follows

$$\psi_a = \frac{1}{4} (1 + \xi \xi_a) (1 + \eta \eta_a) \quad (D.2)$$

where $a = 1 - 4$ and there is no summation on a .

Given an element surface, the tangents to ξ and η are given here in terms of the isoparametric mapping:

$$\left. \begin{aligned} \mathbf{e}_1 = \mathbf{x}_{,\xi} &= \psi_{a,\xi} \mathbf{x}^a = \frac{1}{4} \xi_a (1 + \eta \eta_a) \mathbf{x}^a \\ \mathbf{e}_2 = \mathbf{x}_{,\eta} &= \psi_{a,\eta} \mathbf{x}^a = \frac{1}{4} \eta_a (1 + \xi \xi_a) \mathbf{x}^a \end{aligned} \right\} \quad (D.3)$$

The normality conditions of the gap are as follows:

$$\left. \begin{aligned} \mathbf{e}_1 \cdot (\mathbf{x}_s - \mathbf{x}_c) &= 0, \\ \mathbf{e}_2 \cdot (\mathbf{x}_s - \mathbf{x}_c) &= 0 \end{aligned} \right\} \quad (D.4)$$

Consider now the total differentials of the two equations in Eq. (D.4):

$$d\mathbf{e}_1 \cdot (\mathbf{x}_s - \mathbf{x}_c) + \mathbf{e}_1 \cdot (d\mathbf{x}_s - d\mathbf{x}_c) = 0 \quad (D.5)$$

$$d\mathbf{e}_2 \cdot (\mathbf{x}_s - \mathbf{x}_c) + \mathbf{e}_2 \cdot (d\mathbf{x}_s - d\mathbf{x}_c) = 0 \quad (D.6)$$

From Eq. (D.3), one obtains the differentials of the tangents

$$d\mathbf{e}_1 = \mathbf{x}^* d\eta + d\mathbf{x}_{c,\xi} \quad (D.7)$$

$$d\mathbf{e}_2 = \mathbf{x}^* d\xi + d\mathbf{x}_{c,\eta} \quad (D.8)$$

where the vector \mathbf{x}^* is

$$\mathbf{x}^* = \frac{1}{4}(\xi\eta)_N \mathbf{x}^N = \frac{1}{4}(\mathbf{x}^1 - \mathbf{x}^2 + \mathbf{x}^3 - \mathbf{x}^4) \quad (D.9)$$

which is interpreted as an indicator of shape of the element. It is easy to verify that for a plane element of parallelogram shape $\mathbf{x}^* = 0$. For the second term of Eq. (D.5) and Eq. (D.6) one obtains the following

$$d\mathbf{x}_s - d\mathbf{x}_c = d\mathbf{u}_s - d\mathbf{u}_c - \mathbf{e}_1 d\xi - \mathbf{e}_2 d\eta \quad (D.10)$$

Finally, introducing the four equations (Eq. (D.7), Eq. (D.8), Eq. (D.9), and Eq. (D.10)) into Eq. (D.5) and Eq. (D.6) and solving for the increments of the surface coordinates results in

$$d\xi = \frac{1}{h} \{g(m_{22}\mathbf{n} \cdot d\mathbf{u}_{c,\xi} - \bar{m}_{12}\mathbf{n} \cdot d\mathbf{u}_{c,\eta}) + (m_{22}\mathbf{e}_1 - \bar{m}_{12}\mathbf{e}_2) \cdot (d\mathbf{u}_s - d\mathbf{u}_c)\} \quad (D.11)$$

$$d\eta = \frac{1}{h} \{g(m_{11}\mathbf{n} \cdot d\mathbf{u}_{c,\eta} - \bar{m}_{12}\mathbf{n} \cdot d\mathbf{u}_{c,\xi}) + (m_{11}\mathbf{e}_2 - \bar{m}_{12}\mathbf{e}_1) \cdot (d\mathbf{u}_s - d\mathbf{u}_c)\} \quad (D.12)$$

with the abbreviations

$$\bar{m}_{12} = m_{12} - \mathbf{x}^* \cdot \mathbf{d} \quad (D.13)$$

and

$$h = m_{11}m_{22} - \bar{m}_{12}^2 \quad (D.14)$$

where the normal \mathbf{n} is given as follows

$$\mathbf{n} = \frac{\mathbf{e}_1 \times \mathbf{e}_2}{\|\mathbf{e}_1 \times \mathbf{e}_2\|} \quad (D.15)$$

Having defined the kinematical expressions, the expressions of first and second variations of the gap g must be derived, which involves much algebraic manipulation.

For simplicity, attention is limited to the main equations.

As was shown before, the weak form of the equilibrium equation requires the first variation of the gap g (Eq. (3.9)) with respect to the node variables. Taking the first variation of g results in

$$\delta g = \mathbf{n} \cdot (\delta \mathbf{u}_s - \delta \mathbf{u}_c) + \delta \mathbf{n} \cdot (\mathbf{x}_s - \mathbf{x}_c) \quad (D.16)$$

As $\delta \mathbf{n}$ is perpendicular to \mathbf{n} , the second term of δg vanishes. The second variation of the gap is then

$$d(\delta g) = d\mathbf{n} \cdot (\delta \mathbf{u}_s - \delta \mathbf{u}_c) + \mathbf{n} \cdot d(\delta \mathbf{u}_s - \delta \mathbf{u}_c) \quad (D.17)$$

Some algebraic manipulations show that the variation of \mathbf{n} results in

$$d\mathbf{n} = \frac{1}{\Omega} (\mathbf{I} - \mathbf{n} \otimes \mathbf{n}) d(\mathbf{e}_1 \times \mathbf{e}_2) \quad (D.18)$$

\mathbf{I} is the identity matrix and \otimes denotes tensor product. Ω is the surface element area and is defined as

$$\Omega = \|\mathbf{e}_1 \times \mathbf{e}_2\| \quad (D.19)$$

It is obvious that we need to derive $d(\mathbf{e}_1 \times \mathbf{e}_2)$. By using Eq. (D.7) and Eq. (D.8), one obtains

$$d(\mathbf{e}_1 \times \mathbf{e}_2) = (\mathbf{x}^* \times \mathbf{e}_2) d\eta - (\mathbf{x}^* \times \mathbf{e}_1) d\xi + (d\mathbf{u}_{c,\xi} \times \mathbf{e}_2) - (d\mathbf{u}_{c,\eta} \times \mathbf{e}_1) \quad (D.20)$$

where $d\eta$ and $d\xi$ can be eliminated by applying equations Eq. (D.11) and Eq. (D.12).

After some algebraic manipulations the variation of \mathbf{n} becomes

$$d\mathbf{n} = \frac{1}{\Omega}(\mathbf{I} - \mathbf{n} \otimes \mathbf{n}) \left\{ \begin{aligned} & (d\mathbf{u}_{c,\xi} \times \mathbf{e}_2 + \mathbf{e}_1 \times d\mathbf{u}_{c,\eta}) \\ & + \frac{1}{h}[(\mathbf{e}_1 \times \mathbf{x}^*) \otimes (m_{22}\mathbf{e}_1 - \bar{m}_{12}\mathbf{e}_2)(d\mathbf{u}_s - d\mathbf{u}_c) \\ & + (\mathbf{x}^* \times \mathbf{e}_2) \otimes (m_{11}\mathbf{e}_2 - \bar{m}_{12}\mathbf{e}_1)(d\mathbf{u}_s - d\mathbf{u}_c)] \\ & + \frac{g}{h}[(\mathbf{e}_1 \times \mathbf{x}^*) \otimes \mathbf{n}(m_{22}d\mathbf{u}_{c,\xi} - \bar{m}_{12}d\mathbf{u}_{c,\eta}) \\ & + (\mathbf{x}^* \times \mathbf{e}_2) \otimes \mathbf{n}(m_{11}d\mathbf{u}_{c,\eta} - \bar{m}_{12}d\mathbf{u}_{c,\xi})] \end{aligned} \right\} \quad (D.21)$$

It remains to evaluate the second term of Eq. (D.16), which is simply given by

$$d(\delta\mathbf{u}_s - \delta\mathbf{u}_c) = -(\delta\mathbf{u}_{c,\xi}d\xi + \delta\mathbf{u}_{c,\eta}d\eta) \quad (D.22)$$

By applying Eq. (D.11) and Eq. (D.12) to eliminate $d\xi$ and $d\eta$, one obtains

$$\mathbf{n} \cdot d(\delta\mathbf{u}_s - \delta\mathbf{u}_c) = -\frac{1}{h} \left\{ \begin{aligned} & [\delta\mathbf{u}_{c,\xi}(m_{22}(\mathbf{n} \otimes \mathbf{e}_1) - \bar{m}_{12}(\mathbf{n} \otimes \mathbf{e}_2))(d\mathbf{u}_s - d\mathbf{u}_c) \\ & + \delta\mathbf{u}_{c,\eta}(m_{11}(\mathbf{n} \otimes \mathbf{e}_2) - \bar{m}_{12}(\mathbf{n} \otimes \mathbf{e}_1))(d\mathbf{u}_s - d\mathbf{u}_c)] \\ & - \frac{g}{h}[\delta\mathbf{u}_{c,\xi}(\mathbf{n} \otimes \mathbf{n})(m_{11}d\mathbf{u}_{c,\xi} - \bar{m}_{12}d\mathbf{u}_{c,\eta}) \\ & + \delta\mathbf{u}_{c,\eta}(\mathbf{n} \otimes \mathbf{n})(m_{11}d\mathbf{u}_{c,\eta} - \bar{m}_{12}d\mathbf{u}_{c,\xi})] \end{aligned} \right\} \quad (D.23)$$

The matrix for contact contribution is expected to be symmetric. However, only the last part of Eq. (D.23) shows symmetry *a priori*. To obtain the symmetric expressions requires additional algebraic operations, summarized in the following. First the contribution due to warping must be separated from the other parts by considering \mathbf{x}^* with respect to the local tangential system $\mathbf{e}_1, \mathbf{e}_2$, and \mathbf{n} according to

$$\mathbf{x}^* = x^1\mathbf{e}_1 + x^2\mathbf{e}_2 + x^3\mathbf{n} \quad (D.24)$$

Then it is necessary to evaluate the cross products which give the corresponding contravariant base vectors. In each case, a set of dual basis vectors may be computed

such that $\mathbf{e}^i \cdot \mathbf{e}_j = \delta_j^i$ ($i, j=1-2$). A dual basis at the contact point \mathbf{x}_c may be similarly defined as

$$\mathbf{e}_\alpha \cdot \mathbf{e}_\beta = \delta_\alpha^\beta \quad (D.25)$$

A merit tensor may also be expressed as

$$m_{\alpha\beta} = \mathbf{e}_\alpha \cdot \mathbf{e}_\beta \quad (D.26)$$

The contravariant tangents may be defined as

$$\mathbf{e}^\alpha = (m_{\alpha\beta})^{-1} \mathbf{e}_\beta \quad (D.27)$$

After rearranging the terms in a convenient manner, the final equation is

$$d(\delta g) = \left(\begin{aligned} & \left(\frac{x^3 g}{h} \bar{m}_{12} - 1 \right) [d\mathbf{u}_{c,\xi}(\mathbf{n} \otimes \mathbf{e}^1) + d\mathbf{u}_{c,\eta}(\mathbf{n} \otimes \mathbf{e}^2)](\delta \mathbf{u}_s - \delta \mathbf{u}_c) \\ & + \left(\frac{x^3 g}{h} \bar{m}_{12} - 1 \right) [\delta \mathbf{u}_{c,\xi}(\mathbf{n} \otimes \mathbf{e}^1) + \delta \mathbf{u}_{c,\eta}(\mathbf{n} \otimes \mathbf{e}^2)](d\mathbf{u}_s - d\mathbf{u}_c) \\ & - \frac{g}{h} [m_{22} d\mathbf{u}_{c,\xi}(\mathbf{n} \otimes \mathbf{n}) \delta \mathbf{u}_{c,\xi} + m_{11} d\mathbf{u}_{c,\eta}(\mathbf{n} \otimes \mathbf{n}) \delta \mathbf{u}_{c,\eta}] \\ & - \bar{m}_{12} (\delta \mathbf{u}_{c,\xi}(\mathbf{n} \otimes \mathbf{n}) d\mathbf{u}_{c,\eta} + \delta \mathbf{u}_{c,\eta}(\mathbf{n} \otimes \mathbf{n}) d\mathbf{u}_{c,\xi}) \\ & - \frac{x^3}{h} (d\mathbf{u}_s - d\mathbf{u}_c) [(m_{11} m_{22} - \bar{m}_{12} m_{12}) ((\mathbf{e}^1 \otimes \mathbf{e}^2) + (\mathbf{e}^2 \otimes \mathbf{e}^1)) \\ & + x^3 g (m_{22} (\mathbf{e}^2 \otimes \mathbf{e}^2) + m_{11} (\mathbf{e}^1 \otimes \mathbf{e}^1))] (\delta \mathbf{u}_s - \delta \mathbf{u}_c) \\ & - \frac{x^3 g}{h} [m_{22} d\mathbf{u}_{c,\xi}(\mathbf{n} \otimes \mathbf{e}^2) + m_{11} d\mathbf{u}_{c,\eta}(\mathbf{n} \otimes \mathbf{e}^1)] (\delta \mathbf{u}_s - \delta \mathbf{u}_c) \\ & - \frac{x^3 g}{h} [m_{22} \delta \mathbf{u}_{c,\xi}(\mathbf{n} \otimes \mathbf{e}^2) + m_{11} \delta \mathbf{u}_{c,\eta}(\mathbf{n} \otimes \mathbf{e}^1)] (d\mathbf{u}_s - d\mathbf{u}_c) \end{aligned} \right) \quad (D.28)$$

which proves the symmetry. It is desired to replace the displacement vectors by introducing the displacement interpolation according to Eq. (D.1). The second order part of the contact stiffness then follows from the identity

$$d(\delta g) = d\mathbf{u}^M \frac{\partial^2 g}{\partial \mathbf{u}^M \partial \mathbf{u}^N} \delta \mathbf{u}^N \quad (D.29)$$

From the virtual work linearization, the contact stiffness can be written as

$$\mathbf{k}_c = \epsilon \frac{\partial g}{\partial \mathbf{u}^N} \frac{\partial g}{\partial \mathbf{u}^M} + t \frac{\partial}{\partial \mathbf{u}^N} \left(\frac{\partial g}{\partial \mathbf{u}^M} \right) \quad (D.30)$$

And the contact residual force of the element is

$$\mathbf{f}_c = t \frac{\partial g}{\partial \mathbf{u}^M} \quad (D.31)$$

For computational purposes it is advantageous to rewrite the result in matrix notation. To achieve this, it is first necessary to make the following definitions for vectors such that the slave node is represented as the last node:

$$\left. \begin{aligned} \mathbf{N}^T &= \{-\mathbf{n}\psi_1, -\mathbf{n}\psi_2, \dots, \mathbf{n}\} \\ \mathbf{V}_1^T &= \{-\mathbf{e}^1\psi_1, -\mathbf{e}^1\psi_2, \dots, \mathbf{e}^1\} \\ \mathbf{V}_2^T &= \{-\mathbf{e}^2\psi_1, -\mathbf{e}^2\psi_2, \dots, \mathbf{e}^2\} \\ \mathbf{U}_1^T &= \{\mathbf{n}\psi_{1,\xi}, \mathbf{n}\psi_{2,\xi}, \dots, 0, 0, 0\} \\ \mathbf{U}_2^T &= \{\mathbf{n}\psi_{1,\eta}, \mathbf{n}\psi_{2,\eta}, \dots, 0, 0, 0\} \\ d\mathbf{u} &= \{d\mathbf{u}_1, d\mathbf{u}_2, \dots, d\mathbf{u}_s\} \end{aligned} \right\} \quad (D.32)$$

It is noted that all the vectors are based on the interpolation functions evaluated for the surface coordinates of point c . Using these vectors, the contact reaction forces (contact residual forces) on the contact element with an active slave node are then

$$\mathbf{f}_c = t\mathbf{N} \quad (D.33)$$

The corresponding consistent tangent stiffness matrix takes the form

$$\mathbf{k}_c = \epsilon \mathbf{N} \mathbf{N}^T + t \left\{ \begin{aligned} & \left(\frac{x^3 g}{h} \bar{m}_{12} - 1 \right) [\mathbf{U}_1 \mathbf{V}_1^T + \mathbf{U}_2 \mathbf{V}_2^T + \mathbf{V}_1 \mathbf{U}_1^T + \mathbf{V}_2 \mathbf{U}_2^T] \\ & - \frac{g}{h} [m_{22} \mathbf{U}_1 \mathbf{U}_1^T + m_{11} \mathbf{U}_2 \mathbf{U}_2^T - \bar{m}_{12} (\mathbf{U}_1 \mathbf{U}_2^T + \mathbf{U}_2 \mathbf{U}_1^T)] \\ & - \frac{x^3}{h} [(m_{11} m_{22} - \bar{m}_{12} m_{12}) (\mathbf{V}_1 \mathbf{V}_2^T + \mathbf{V}_2 \mathbf{V}_1^T) + x^3 g (m_{11} \mathbf{V}_1 \mathbf{V}_1^T + m_{22} \mathbf{V}_2 \mathbf{V}_2^T)] \\ & - \frac{x^3 g}{h} [m_{22} (\mathbf{U}_1 \mathbf{V}_2^T + \mathbf{V}_2 \mathbf{U}_1^T) + m_{11} (\mathbf{U}_2 \mathbf{V}_1^T + \mathbf{V}_1 \mathbf{U}_2^T)] \end{aligned} \right\} \quad (D.34)$$

where the $t = \epsilon g$ for the penalty method, and $t = \lambda + \epsilon g$ for augmented Lagrangian treatment. It must be emphasized that, except for the linear term $\mathbf{N} \mathbf{N}^T$, all terms are due to the second variation of the gap and therefore account for its nonlinear kinematics. It is seen that the contribution due to warping represented by those parts containing x^3 is well separated from the others. Obviously, for linear kinematics, warping does not enter into consideration.

As a special case, the residual and stiffness matrix for a three node triangular contact segment can be extracted by simply letting $x^3 = 0$ in Eq. (D.34). Another simplification is due to the fact that the physical point of contact can be explicitly calculated since the normal \mathbf{n} is constant. Expressions for node-to-line element and node-to-node element in 3-D space can be similarly derived. Expressions for planar and axisymmetric problems can be readily derived using an approach similar to the one used above.

For the case where one body is deformable and the other is rigid, and the motion of the rigid body (master surface) is prescribed, it is assumed that the surface can be represented either by a set of element edges defining the surface or in a globally continuous fashion. The effect of this assumption is simply to eliminate the master degrees of freedom from the problem, leaving only the slave degrees of freedom as unknowns.

Appendix E

Input Data Files for Computer Codes

§E.1 Interface for 2CRACK

The model described in Chapter 3, was implemented into a nonlinear finite element program designated as "2CRACK". An user-friendly interface to 2CRACK was written to enable users unfamiliar with finite element procedures to analyze laminated composite panels either with or without pre-existing matrix cracks and delaminations.

A typical terminal session using 2CRACK is listed below. The problem solved is a flat panel subjected to a line load as described in Chapter 3.

STARSDUAL [DURAND] INPUT. INT: 1 20-AUG-1992 09:24 Page 2

delamination propagation in laminated composites subjected to quasi-static transversely concentrated loading, "AFOSR Progress Report for the Period Between October 1, 1989 - September 31, 1990 Under Grant No. AFOSR 89-0554

***** TO CONTINUE PRESS "RETURN" *****

The program can calculate:

1. The deformation of the panel from initial loading, through initial damage, induced delamination growth, to final collapse
2. Initial damage in terms of load and type of damage
3. Strain energy release rates
4. Length of the delaminations
5. Collapse load

***** TO CONTINUE PRESS "RETURN" *****

User-friendly Interface

The user-friendly interface to PCRACK is used to create a new "input data set". The "input data set" is created in the sections:

1. Control parameters
2. Loading
3. Geometry of the panel
4. Boundary conditions
5. Material properties
6. Laminate layup
7. Finite element mesh
8. For cracked specimens, the location of the cracks
9. Output information

Introductions and instructions provided at the beginning of each section

***** TO CONTINUE PRESS "RETURN" *****

***** PHYSICAL UNITS *****

CAUTION:

The units for all the parameters must be consistent

***** CONTROL PARAMETERS *****

MESH: Panel is flat or cylindrical ?

FOR flat panel ENTER "fl";

FOR cylindrical panel ENTER "cy";

fl

PCRACK: Panel is pre-cracked or delaminated ?

FOR YES ENTER 1;

FOR NO ENTER 0;

STARSDUAL [DURAND] INPUT. INT: 1 20-AUG-1992 09:24 Page 1

22222222 CCCCC RRRRRR AA CCCCC KK KK

22 CC RR AA AA CC KK KK

22 CC RR AA AA CC KK KK

22222222 CCCCC RRRRRR AAAAAA CC KKKK

22 CC RR AA AA CC KK KK

22 CC RR RR AA AA CC KK KK

22222222 CCCCC RR RR AA CCCCC KK KK

A PROGRAM TO CALCULATE THE TRANSVERSE RESPONSE OF LAMINATED COMPOSITE PANELS CONTAINING 0 AND 90 PLY GROUPS.

This program is a research tool in the development stage and is supplied "as is" for the purpose of scientific collaboration.

***** TO CONTINUE PRESS "RETURN" *****

SHENG LIU, ZAFER S. KUTLU, AND FU-KUO CHANG

DEPARTMENT OF AERONAUTICS AND ASTRONAUTICS

STANFORD UNIVERSITY

STANFORD, CA 94305

(415) 723-3466

MAY 1991

(c) COPYRIGHT, S. LIU, Z. S. KUTLU, AND F. K. CHANG

***** TO CONTINUE PRESS "RETURN" *****

Do you want to read an introduction to this program? (y/n)

y

This program was developed to calculate the transverse response of laminated composite panels containing 0 degree and 90 degree ply groups. The panels can be either flat or cylindrical. The panels may be pre-cracked/pre-delaminated, or initially perfect. The pre-cracked specimens include FRB(double cantilever beam), CNF(central notched flexure), surface notched 90/90 specimen, etc. Two types of matrix cracks are defined. One is a surface (bending) crack. And another is internal (shear) crack. The code can simulate the formation of these two types of matrix crack and their induced delamination(s). Delaminations are assumed to be uniform through the width of the panel. It is assumed that there is no friction between the two delamination surfaces.

Further information regarding this program can be found in:

1. Liu, S., Kutlu, Z., and Chang, F. K., "Matrix cracking and

[illegible]

```

STARSDUAL: [DURAND] INPUT INT: 1      20-AUG-1992 09:24      Page 6

icrit: Failure criterion for initial damage
Enter: 1-Tsal-Mu; 2-Hasilin; 3-Gosse; 4-Chang-Choi
2

Enter the longitudinal tensile strength, X_t, in Pa or psi
220000

Enter the longitudinal compressive strength, X_c, in Pa or in psi
231000

Enter the transverse compressive strength, Y_c, in Pa or in psi
167000

Enter the transverse tensile strength of a unidirectional laminate, Y_o.t, in Pa
14500

Enter the statistical constant A
if assume constant property, enter 0
1.3

Enter the statistical constant B
if assume constant property, enter 0
0.7

Enter the shear strength, S_cp, measured from a cross ply laminate in Pa in psi
55000

Enter the statistical constant C
if assume constant property, enter 0
2

Enter the statistical constant D
if assume constant property, enter 0
1

The nonlinear stress-strain relationship is assumed to be in the form:

Eps_xy = [Sigma_xy / G_xy] + Alpha [Sigma_xy]^3

Enter the in-plane shear nonlinearity constant, Alpha, in 1/Pa^3 or in 1/psi^3
if assume linear, enter 0
0

Enter the critical strain energy release rate for Mode I, G_Ic, in J/m^2 or in
0.5

Enter the critical strain energy release rate for Mode II, G_IIc, in J/m^2 or in
1.8

*****
*                               *
*               LAMINATE LAYUP   *
*                               *
*                               *
*****

Would you like to read some information about the laminate
layup data input? (y/n)
y

```

STAR\$JUAL: [DURAND] INPUT: INT: 1 20 AUG 1992 09:24 Page 8

ALYG(j): Enter the orientation of the plies in this stack

Enter the information about stack number 2

ALYG(j): Enter the number of elements in this stack

ALYG(j): Enter the orientation of the plies in this stack

Enter the information about stack number 3

ALYG(j): Enter the number of elements in this stack

ALYG(j): Enter the orientation of the plies in this stack

0

LAMINATE LAYUP

| Stack No. | No. of elements | Orientation (degrees) |
|-----------|-----------------|-----------------------|
| 1 | 3 | 0.00000E+00 |
| 2 | 3 | 0.90000E+02 |
| 3 | 3 | 0.00000E+00 |

***** FINITE ELEMENT MESH *****

Would you like to read some information about user-specified mesh generation? (Y/N)

"Y"

The user is allowed to select the number of elements through the thickness and the number of elements along the length (or circumference for cylindrical panels). The restrictions in choosing the number of elements are:

1. The aspect ratio of the elements (length/thickness) must be less than 3 for numerical accuracy
2. If the failure model is used, then the thickness of an element must be equal to the thickness of a ply
3. One element must contain plies of the same ply orientation

***** TO CONTINUE PRESS "RETURN" *****

NAPLY: Enter the number of actual plies through the thickness

18

NELARC: Enter the number of elements along the span-direction of half model:

60

NINCR: Enter increments interval you want your mesh output for deformation plotting for display

Enter an integer which is greater than 0:

2

STAR\$JUAL: [DURAND] INPUT: INT: 1 20 AUG 1992 09:24 Page 7

Thickness

STACK 2

STACK 1

LENGTH

x y

The laminate layup is entered by the orientation of the plies in the stacks. A "stack" is a group of plies with the same orientation. Stack numbering starts with the inside stack. For cylindrical panels, a 0 degree stack is the stack which consists of plies with fibers in the circumferential direction. However, one ply defined here is actually is one finite element through the thickness direction.

***** TO CONTINUE PRESS "RETURN" *****

Example:

Consider 10_2/90_21_s layup. The layup data is :

Total number of stacks : 3

Stack number 1

Number of plies : 2

Orientation : 0

Stack number 2

Number of plies : 4

Orientation : 90

Stack number 3

Number of plies : 2

Orientation : 0

***** TO CONTINUE PRESS "RETURN" *****

The above layup input can be changed for finite element analysis (to reduce the cost) as follows:

10_1/90_11_s layup. So we put two actual plies into one element in the thickness direction. The layup data is :

Total number of stacks : 3

Stack number 1

Number of elements : 1

Orientation : 0

Stack number 2

Number of elements : 2

Orientation : 90

Stack number 3

Number of elements : 1

Orientation : 0

We need to key in the actual number of plies later in order to use in-situ strength data

***** TO CONTINUE PRESS "RETURN" *****

NAPLY: Enter the total number of stacks

1

Enter the information about stack number 1

ALYG(1) Enter the number of elements in this stack

1

Enter the name of load-displacement file
You may enter loadis.dat;
loadis.dat

Enter the name of the plotting data file
for delamination #1, energy release rate will be in
actual values. You may enter drive1.dat:
drive1.dat

Enter the name of the plotting data file
for delamination #2, energy release rate will be in
actual values. You may enter drive2.dat:
drive2.dat

Enter the name of the plotting data file
for delamination #1, energy release rate will be in
ratios of actual values to the fracture toughness
you may enter stnl.dat:
stnl.dat

Enter the name of the plotting data file
for delamination #2, energy release rate will be in
ratios of actual values to the fracture toughness
You may enter stn2.dat:
stn2.dat

Enter the name of the file for deformed shapes
You may enter mesh.dat:
mesh.dat

Enter the name of the file for initial
damage initial information. You may enter fail.dat:
fail.dat

"input.dat" file is used by "PCrack" main program. You may save the new data to "input.dat" or to another file name you choose. Saving new data will ERASE the data in the existing files.

Enter the name of the file, it can be input.dat
input.dat

DISTRIBUTION OF DELAMINATIONS
AND MATRIX CRACKS

Do you want to go beyond the initial damage?

If yes, enter 1:
If no, enter 0:

| Thickness | Length | Y | X |
|------------------|--------|---|---|
| STACK 3 (0)6 | | | |
| STACK 2 (90)6 | | | |
| STACK 1 (0)6 | | | |

Enter the location of possible matrix crack whose length we assume equal to the thickness of 90 degree ply group. For example, [0 6/90 6/0 6], the matrix crack is assumed in the vertical direction and located from 7th row to 12th row in terms of FEM mesh as NIKKAL1=7, NIKKAL2=12 here

Enter N3KHALI.

Einzel N)KRA12:

.....
OUTPUT INFORMATION

The following output data files can be created:

- 1 Summary of the problem and input data
- 2 Load displacement data
- 3 Data for plotting for lower interface delamination
This file contains load, displacement, delamination lengths, strains, strain energy release rates
- 4 This file contains data for upper interface delamination
This file contains load, displacement, delamination lengths, strains, strain energy release rates
- 5 Data for plotting for lower interface delamination
This file contains load, displacement, delamination lengths, strains, strain energy release rate ratios
- 6 Data for plotting for upper interface delamination
This file contains load, displacement, delamination lengths, strains, strain energy release rate ratios
- 7 reformed shape of the panel at different load steps
This file contains the coordinates of the nodal points at different load levels. This file can be very large at different output file.
- 8 Failure message file

[illegible]

```

STARSDUAL: [DURAND] INPUT.DAT;1          20-AUG-1992 09:24          Page 1

fl      mesh: flat: "fl", cylindrical: "cy"
0      ncrack: 1-originally cracked; 0-originally perfect
-0.40000E-02 du: displacement increment
0.15000E+04 xload: maximum load
150     itter: load step number limit
0.15200E+01 arc: arch-arc angle; plate-model length
0.00000E+00 rin: inner radius; plate: 0.0
0.89600E-01 hi: plate thickness
0.10000E+00 h0: plate thickness with strain gage attached
3      ibound: CC.R:3; MSS.R:9; CC.RN:10, SS.RN:11, etc
1      nlp: SS point location for IBOUND=9
0.17600E+08 E_xx
0.14100E+07 E_yy
0.14100E+07 E_zz
0.81000E+06 G_xy for linear case; G^o_xy for nonlinear case
0.50360E+06 G_yz
0.81000E+06 G_xz
0.29000E+00 Nu_xy
0.40000E+00 Nu_yz
0.29000E+00 Nu_xz
0      In-situ strength? 1:yes; 0:no
2      icrit: 1-Tsai; 2-Hashin; 3-Gosse; 4-Chang-Choi
0.22000E+06 X_t
0.23100E+06 X_c
0.64500E+04 Y_t for constant; Y^o_t for in-situ
0.13000E+01 A an empirical constant for in-situ Y_t
0.70000E+00 B an empirical constant for in-situ Y_t
0.36700E+05 Y_c
0.15500E+05 Shear strength
0.20000E+01 C an empirical constant for in-situ S_c
0.10000E+01 D an empirical constant for in-situ S_c
0.00000E+00 Alpha
0.50000E+00 Strain energy release rate for mode I, G_Ic
0.18000E+01 Strain energy release rate for mode II, G_IIc
3      Total number of stacks
3      Number of plies in stack no. 1
0.00000E+00 Orientation of stack no. 1
3      Number of plies in stack no. 2
0.90000E+02 Orientation of stack no. 2
3      Number of plies in stack no. 3
0.00000E+00 Orientation of stack no. 3
18     naply: Total number of actual plies
60     nelarc: number of elements on the length (or circumference)
2      nmdat: number of increments interval you want your output
1      igrow: 1:initial damage growth; 0:no growth
4      n3kral1: location of matrix crack (lower)
6      n3kral2: location of matrix crack (upper)
loaddis.dat output LOAD-DISPLACEMENT FILE e.g. loaddis.dat
drivel.dat plotting data file name FOR #1 DELAMINATION, e.g. driv1.dat
drive2.dat plotting data file name FOR #2 DELAMINATION, e.g. drive2.dat
stn1.dat plotting data file name FOR #1 DELAMINATION, e.g. stn1.dat
stn2.dat plotting data file name FOR #2 DELAMINATION, e.g. stn2.dat
mesh.dat deformed shape data file name, e.g. mesh.dat
fail.dat FAILURE data file name, e.g. fail.dat

```

§E.2 Input Data for 3CRACK

The model described in Chapter 4, was implemented into a nonlinear finite element program designated as "3CRACK". An input data and the User Manual to 3CRACK were written to enable users unfamiliar with finite element procedures to analyze laminated composite panels either with or without pre-existing matrix cracks and delaminations.

A typical input data file using 3CRACK is listed below. The problem solved is a flat panel containing an existing surface crack, an internal shear crack and an elliptical delamination subjected to a spherical indenter as described in Chapter 4.

SAMPLE INPUT.DAT DELAMINATION WITH BOTH TYPES OF CRACKS

```

STAR$DUAL:[DURAND]INPUT.DAT;2          20-AUG-1992 09:35          Page 1
0   igrad: consider updating stiffness 1: yes 0: no
0   liucd: consider material degradation 1: yes 0: no
-2  load: load type 0: POINT; 1:LINE; 2:CONTACT 3:Beam Comp; -2: Hertz cont
-0.005 du: DISPLACEMENT INCREMENT
0.25 rimpact: indenter radius
250. xload: MAXIMUM LOAD desired
3   IGEO: Geometry type 1:CYLINDER; 2:ARC; 3:BEAM
9   IGEOs:plate type 1:solid; 2:DCB; 3: plate with ec del;4: del+shear cr
1   MOPTN:1: 1/4 model (1/2 for DCB); 2:1/2 model (full for DCB)
2.0,1.5,0.104 xleng,yleng,zleng: sizes of the plate
0.0 Rin: inner radius for the curved plate. zero for flat panels
+18 IBOUND:1:CC.FF 2:CC.SYM 3:CORNER.CC.SYM 7:BE.CC.SYM 18:CC+bc+sc 19: 20:
9   nxsegt: total # of segments in x direction
1.1,1.1,1.1,1.2,1.1 nxseg(1-nxsegt): # of elements in each segment.
0.03,0.06,0.02,0.01,0.01,0.01,1.19,0.2,0.47 xseg(1-nxsegt):segments sizes
4   nssegt: total # of segments in theta(s) direction
1.1,1.1 nsseg(1-nxsegt): # of elements in each segment.
22.5,22.5,22.5,22.5 sseg(1-nxsegt):segments in degrees
4   nzsegt: total # of segments in thickness direction
2.1,1.1 nzseg(1-nxsegt): # of elements in each segment.
0.013,0.039,0.039,0.013 zseg(1-nzsegt): segments sizes
1   NDEL: number of delaminations. limited to 1, or 0 for undelaminated panels
5.1 nxsegc,nzsegc: delamination location # of segments in x and z
0.10,0.15,0.0899 ra,rb,rc:size of del.long/short ax,rc<min(ra,rb)-nxseg(nxsegc)
0.013 dzlc: delamination location in thickness direction
2.0,0.375,0.013 icshape(1),rx(1),rz(1):bend crack. type, x and z sizes
0.151 ryc(1): shear crack length (in y)
1.0,0.03 nbshcr,shcr: location in segment # and size of shear crack in x
0.0131,0.0905 shzcl,shzc2: location of shear crack in z
23.2e+06 , 1.3284e+06 , 1.3284e+06 ex,ey,ez: young's modului in x,y,and z
0.9086e+06 , 0.9086e+06 , 0.9086e+06 gxy,gyz,gxz: shear mogului
.28 , .28 , .28 vxy,vyz,vxz: poisson's ratios
412930.,190840. XX, XXC: tensile and compressive strength in x
6410.,24346. YY, YYC: tensile and compressive strength in y
5877. SS0: in-plane shear for
0.0 ALPHA: SHEAR NONLINEARITY FACTOR
0.,0. AXX, AYY:thermal expansion coefficients in x and y
75. TR: Stress free temperature
75. T0: Room temperature
2   icrit: type of criterion for initial damage: 1:Tsai 2:Hashin 3:Gosse
1.5 ,18.0,18.0 Gmaxn,gmaxs,gmaxt: fracture toughnss in Mode I,II,and III
4   NPLYG:# OF PLY GROUPS, refer to nzsegt, counting from the bottom
2   # OF LAYERS IN #1 GROUP
0.   PLY ORIENTATION OF #1 GROUP
1   # of layers in group #2
90.0 ply orientation of ply group #2
1   # of layers in group #3
90. ply orientation of ply group #3
1   # of layers in group #4
0.   ply orientation of ply group #4
1.1,2,1,1,1,1,10000. 1,icontac,islt,npas,isech,ictype,naug,penp
2,1,2,2,1,1,1,10000. 2,icontac,islt,npas,isech,ictype,naug,penp
0.
0.

```

SUMMARY

This manual describes the input data used by 3CRACK. For convenience, the input data is read from one file: `input.dat`. The input data is arranged in the following sequence:

- 1) Global parameters and control data.
- 2) Loading.
- 3) Geometry of the panel.
- 4) Boundary conditions.
- 5) Finite element mesh.
- 6) For cracked specimens, the location of the cracks.
- 7) Material properties.
- 8) Lay-up.
- 9) For contact, specify contact stiffness and solution algorithm.

The data is read in format free input; hence, comments can be inserted in the input files between the data lines and following the last item in a data line. Here, a data line is defined as a sequence of input values that follow continuously, usually on one line.

INPUT.DAT-a manual**1. Control Parameters**

igrad: updated stiffness index

1: the material stiffness coefficients c_{ij} are updated. In general, the convergence can be improved;

0: $c_{ij} = C_{ij}$ is assumed. It can save computing time in calculating the c_{ij} due to the deformation.

liucd: material degradation index

1: Material degradation model is activated;

0: No material degradation is considered. It is suggested not to consider material degradation for the time being.

2. Loading Parameters

load: load type index.

0: a point load applied at the center of the plate;

1: a line load uniformly applied in the center line of width direction;

2: contact load applied by in-situ contact;

3: axial compression applied;

-2: Hertzian contact applied.

du: displacement load increment for each step.

ndcb: line load type index. Not used for other types of load.

2: a line load applied on upper and lower center line of the specimen such as in DCB I loading ;

1: a line load applied on upper center line of the specimen such as in DCB II, I+II, or cylindrical line loading ;

-1: a line load applied on the lower center line of the specimen.

rimpact: indenter/impact radius. Enter only for contact loads (Load=2, or -2).

zload: the maximum load desired.

3-Geometry Parameters

igeo: geometry type.

1: for a full cylinder;

2: for a arch ;

3: for a beam or plate.

igeos: plate type.

1: for a solid beam or plate;

2: for a DCB beam (with one through-the-width crack);

3: for a plate with an elliptical delamination (with or without a bending crack);

9: for a plate with an elliptical delamination offset by an internal shear crack (with or without a bending crack).

moptn: symmetry index for analysis.

1: 1/4 model for regular plate, 1/2 for a DCB or a cantilever plate;

2: 1/2 model for a regular plate, full model for a DCB or a cantilever plate. In most cases, half or 1/4 model is used.

xleng, yleng, zleng: beam or plate dimensions in the length, width, and thickness directions.

arc: arch angle in terms of degrees (enter only for arc and cylinders.)

rin: for arc, enter the inner radius; for plate enter 0.

4-Boundary Conditions (support conditions)

ibound: boundary conditions type (including matrix cracks conditions)

1: left side-full clamped, other three sides-free (typical for cantilever beam of DCB);

- 2: back and front sides - free, left side - full clamp, right side-symmetry roller support;
- 3: back and front sides - free, left side - upper and lower edges compressive clamp (allowing the axial movement), right side - symmetry roller support;
- 7: back and front sides - free, left side - full compressive clamp (allowing axial movement), right side - symmetry roller support;
- 16: back and front sides - free, left side - full clamp, right side - symmetry roller support, bending crack in the x-z plane (simulating splitting the outermost 0 degree layers);
- 18: back and front sides - free, left side - full clamp, right side - symmetry roller support, bending crack in the x-z plane (simulating splitting the outermost 0 degree layers). In addition, a shear crack at a distance from the indenter is simulated;
- 19: 1/4 model for a four sided simply supported plate. Back -SS, front - symmetry roller, left side - SS, right side - symmetry roller support;
- 20: 1/4 model for a four sided simply supported plate but constrained to have $w = 0$ on the bottom of the plate.

5-Mesh Generation

First enter the information needed for x direction:

nxsegt: number of the segments in x direction for mesh generation.

(nxseg(i), i=1, nxsegt): number of the elements in each segment.

(xseg(i), i=1, nxsegt): size of each segment.

(It is noted that a non-uniform mesh can be formed, which is helpful for areas such as concentrated loading zone and the crack front, where a very fine mesh is desired. There are several checks to be done to make sure the mesh is right. The key checks are the length of the beam (*xleng*), the critical shear crack location, the

delamination size. For example, the sum of $xseg(1$ to $nxseg)$ has to be the length of the plate. More will be discussed in the following.)

Then enter the information needed for y or theta direction:

For $igeos \geq 3$ and $igeos \leq 9$, enter information for panels containing elliptical delaminations. In this case, the $sseg(i)$ has to input the angles in terms of degrees.

$nsseg$: number of the segments in angle direction for mesh generation.

$(nsseg(i), i=1, nsseg)$: number of the elements in each segment.

$(sseg(i), i=1, nsseg)$: size of each segment, the sum of them must be 90 degrees.

Otherwise, enter information for panels without delamination.

$nyseg$: number of the segments in y direction for mesh generation.

$(nyseg(i), i=1, nyseg)$: number of the elements in each segment.

$(yseg(i), i=1, nyseg)$: size of each segment.

6-Delamination and Matrix Cracks

$ndel$: input delamination index.

0: no delamination;

1: one delamination;

If there is a delamination ($ndel \neq 0$), determine the location of the delamination:

$nzsegc, nzsegc$: delamination location index.

$nzsegc$: Number of segments in the span length before the delamination front in terms of $nzseg$ and $nzseg(i)$;

$nzsegc$: Number of segments in the thickness direction before the delamination front in terms of $nzseg$ and $nzseg(i)$.

ra, rb, rc : delamination size index.

ra : elliptical size in x axis;

rb : elliptical size in y axis;

rc: a number used for modified elliptical transformation in generating the mesh.

And it should be a number smaller than either *ra* or *rb* such that the one or two row elements in the delamination front is allowed. The estimated formula is given as: $rc \leq \min(ra, rb) - xseg(nxsegc)$.

dzlc: delamination location in thickness direction

If there is any bending crack ($ibound \geq 14$ and $ibound \leq 18$), the location, shape, and size of the bending crack need to be determined.

icshape(1), rzc(1), rzc(1): bending crack location, shape, and size.

icshape(1): bending crack shap: 2-rectangular; 1-elliptical. 2 is recommended.

rzc(1): bending crack length in x direction.

rzc(1): bending crack depth in thickness direction.

If there is any shear crack ($ibound = 9$), the location, shape, and size of the shear crack needs to be determined.

ryc(1): shear crack length in y direction

nbshcr, shcr: shear crack location in x direction

nbshcr: number of segment in terms of *nxseg(i)*.

shcr: location in terms of size in x, which is the distance from the indenter or the center line of the plate.

shzc1, shzc2: shear crack location in z direction.

shzc1: the location of the lower tip of the shear crack.

shzc2: the location of the upper tip of the shear crack.

The key check here is that the mentioned quantities are generally associated with the 0/90 or 90/0 interface heights.

7-Material Properties

EX, EY, EZ: enter Young's moduli EX, EY, EZ.

GXY, GYZ, GXZ: enter the shear moduli GXY, GYZ, GXZ.

VXY, VYZ, VXZ: enter the Poission's ratios: VXY, VYZ, VXZ.

XX, XXC: enter the strength in longitudinal direction XX, XXC.

YY,YYC: enter the strength In transverse direction *YY,YYC*.

SS0: enter the shear Strength *SS*.

ALPHA: enter the nonlinear shear parameter : *ALPHA*.

AXX,AYY: enter the thermal coefficients (*AXX,AYY*)

TR: enter the stress free temperature.

T0: enter the room temperature.

ICRIT: enter failure criteria options. 1: TSAI 2: HASHIN 3: GOSSE.

GMAXN, GMAXS, GMAXT: enter the fracture toughness in Mode I, II, and III.

8 - LAY-UPS

NPLYG: enter the number of ply group.

The following is for each layer counting from the bottom ply.

NLYG(I): enter the number of plies for ply group *I*

ALYG(I): enter the ply orientation for ply group *I*

9 - contact algorithm input

i, icontac(i), islt(i), npas(i), isech(i), ictype(i), naug(i), penp(i): contact interface data

i: the *i*-th contact surface. In general, two contact surfaces are considered. One is the contact between the indenter and the plate. The other is the delamination contact.

icontac(i): 1: activating the contact algorithm; 0: no contact considered.

islt(i): 1: penalty method; 2: augmented Lagrangian method.

npas(i): 1: one-pass algorithm; 2: two-pass algorithm.

isech(i): 1: the type-1 simple search algorithm; 2: more rigorous search algorithm.

ictype(i): contact element type. 0: node-to-node; 1: node-surface; 2: adaptive.

naug(i): enter 1 please.

penp(i): penalty parameter.

References

- [1] Finn, S. R., and G. S. Springer, "Composite Plates Impact Damage: An Atlas," Technomic Publishing Co., Inc., Lancaster, USA, (1991).
- [2] Finn, S. R., "Delaminations in Composite Plates under Transverse Static or Impact Loads," Ph.D. Thesis, Department of Aeronautics and Astronautics, Stanford University, (1991).
- [3] Sjöblom, P.O., J.T. Hartness, and T.M. Cordell, "On Low-Velocity Impact Testing of Composite Materials," *J. of Composite Materials*, Vol. 22, (1988), pp. 30-52.
- [4] Wu, H.T., and G.S. Springer, "Measurements of Matrix Cracking and Delamination Caused by Impact on Composite Plates," *J. of Composite Materials*, Vol. 22, (1988), pp. 518-532.
- [5] Gosse, J.H., and P.B.Y. Mori, "Impact Damage Characterization of Graphite/Epoxy Laminates," Proceedings of the Third Technical Conference of the American Society for Composites, Seattle, WA, (1988), pp. 334-353.
- [6] Joshi, S.P., "Impact-Induced Damage Initiation Analysis: An Experimental Study," Proceedings of the Third Technical Conference of the American Society for Composites, Seattle, WA, (1988), pp. 325-333.
- [7] Joshi, S.P., and C.T. Sun, "Impact-Induced Fracture in Quasi-Isotropic Laminate," *J. of Composite Technology and Research*, Vol. 19, (1986), pp. 40-46.
- [8] Choi, H.Y., R.J. Downs, and F.K. Chang, "A New Approach Toward Understanding Damage Mechanisms and Mechanics of Laminated Composites Due

- to Low-Velocity Impact, Part I - Experiments," *J. of Composite Materials*, Vol. 25, No. 8, (1991), pp. 992-1011.
- [9] Poe, Jr., C.C., "Simulated Impact Damage in a Thick Graphite/Epoxy Laminate Using Spherical Indenters," NASA TM-100539, January, (1988).
- [10] Sun, C.T., and S.H. Yang, "Contact Law and Impact Responses of Laminated Composites," NASA CR-159884, NASA, Washington D.C., (1980).
- [11] Tan, T.M., and C.T. Sun, "Use of Statical Indentation Laws in the Impact Analysis of Laminated Composite Plates," *J. of Applied Mechanics*, Vol. 52, March, (1985), pp. 6-12.
- [12] Lal, K.M., "Low Velocity Transverse Impact Behavior of 8-ply Graphite/Epoxy Laminates," *J. of Reinforced Plastics and Composites*, Vol. 2, October, (1983), pp. 216-225.
- [13] Greszczuk, L.B., "Foreign Objects Damage to Composites," *ASTM STP 568*, (1973).
- [14] Chamis, C.C., and J.H. Sinclair, "Impact Resistance of Fiber Composites: Energy-Absorbing Mechanisms and Environmental Effects," *Recent Advances in Composites in the United States and Japan*, ASTM STP 864, (Vinson and Taya, eds.), (1983), pp. 326-345.
- [15] Chamis, C.C., M.P. Hanson, and T.T. Serafini, "Designing for Impact Resistance with Unidirectional Fiber Composites," NASA TND-6463, NASA, Washington D.C., (1971).
- [16] Wu, H.T., and G.S. Springer, "Impact Induced Stresses, Strains and Delaminations in Composite Plates," *J. of Composite Materials*, Vol. 22, (1988), pp. 533-560.
- [17] Sun, C.T., and S. Rechak, "Effect of Adhesive Layers on Impact Damage in Composite Laminates," *Composite Materials: Testing and Design (Eighth Con-*

- ference), *ASTM STP 972* (J.D. Whitcomb, ed.), American Society for Testing and Materials, Philadelphia, PA, (1988), pp. 97-123.
- [18] Clark, G., "Modelling of Impact Damage in Composite Laminates," *Composites, Vol. 19*, (1988), pp. 209-214.
- [19] Reed, P.E., and S. Turner, "Flexed Plate Impact, Part 7. Low Energy and Excess Energy Impacts on Carbon Fiber-Reinforced Polymer Composites," *Composites, Vol. 19*, (1988), pp. 193-203.
- [20] Liu, D., and L.E. Malvern, "Matrix Cracking in Impacted Glass/Epoxy Plates," *J. of Computers and Structures, Vol. 21*, (1987), pp. 594-609.
- [21] Gu, Z.L., and C.T. Sun, "Prediction of Impact Damage Region in SMC Composites," *Composite Structures, Vol. 7*, (1987), pp. 179-190.
- [22] Sun, C.T., and S. Chattopadhyay, "Dynamic Response of Anisotropic Laminated Plates Under Initial Stress to Impact of a Mass," *J. of Applied Mechanics, Vol. 42*, (1975), pp. 693-698.
- [23] Chen, J.K., and C.T. Sun, "Analysis of Impact Response of Buckled Composite Laminates," *Composite Structures, Vol. 3*, (1985), pp. 97-118.
- [24] Chen, J.K., and C.T. Sun, "On the Impact of Initially Stressed Composite Laminates," *J. of Composite Materials, Vol. 19*, November, (1985), pp. 490-504.
- [25] Stori, A.A., and E. Magnus, "An Evaluation of the Impact Properties of Carbon Fiber Reinforced Composites with Various Matrix Materials," *J. of Composite Structures, Vol. 2*, (1983), pp. 332-348.
- [26] Malvern, L.E., R.L. Sierakowski, L.A. Ross, and N. Cristescu, "Impact Failure Mechanisms in Fiber-Reinforced Composite Plates," *High Velocity Deformation of Solids* (Kawata and Shiori, eds.), Springer-Verlag, Berlin, (1978), pp. 120-130.

- [27] Jones, S., J. Paul, T.E. Tay, and J.F. Williams, "Assessment of the Effect of Impact Damage in Composites: Some Problems and Answers," *Composite Structures*, Vol. 10, (1988), pp. 51-73.
- [28] Sun, C.T., and J.E. Grady, "Dynamic Delamination Fracture Toughness of a Graphite/Epoxy Laminate Under Impact," *Composite Science and Technology*, Vol. 31, (1988), pp. 55-72.
- [29] Guynn, E.G., and T.K. O'Brien, "The Influence of Lay-up and Thickness on Composite Impact Damage and Compression Strength," Proceedings of AIAA/ASME/ASCE/AHS, 26th Structure, Structural Dynamics and Materials Conference, Orlando, FL, (1985), pp. 187-196.
- [30] Elber, W., "Failure Mechanics in Low-Velocity Impacts on Thin Composite Plates," *NASA Technical Paper TP 2152*, NASA-Langley Research Center, Hampton, VA, (1983).
- [31] Cantwell, W.J., and J. Morton, "Geometrical Effects in the Low Velocity Impact Response of CFRP," *Composite Structures*, Vol. 12, (1989), pp. 39-59.
- [32] Choi, H.T., H.Y.T. Wu, and F.K. Chang, "A New Approach Toward Understanding Damage Mechanisms and Mechanics of Laminated Composites Due to Low-Velocity Impact, Part II - Analysis," *J. of Composite Materials*, Vol. 25, No. 8, (1991), pp. 1012-1038.
- [33] Choi, H.Y., H.S. Wang, and F.K. Chang, "Effect of Laminate Configuration and Impactor's Mass on the Initial Impact Damage of Composite Plates Due to Line-Loading Impact," *J. of Composite Materials*, (to appear).
- [34] Choi, H.Y., "Effect of Transversely Low-Velocity Impact on Graphite/Epoxy Laminated Composites," Ph.D. Thesis, Department of Mechanical Engineering, Stanford University, (1991).
- [35] Wang, H.S. and F.K. Chang, "Curvature Effect on Impact Damage in Lami-

- nated Composites Subjected to Low-Velocity Impact," The Proceedings of the Eighth International Conference on Composite Materials, Honolulu, HI, July 1991, section 22-29, pp. 28-K-1 to -11.
- [36] Abrate, S., "Impact of Laminated Composite Materials – a Review," *Composites*, Vol. 22, (1991), pp. 347-362.
- [37] Cantwell, W. J., and J. Morton, "The Impact Resistance of Composite Materials," *Applied Mechanics Review*, Vol. 44, (1991), pp. 155-190.
- [38] Bostaph, G. M., and W. Elber, "A Fracture Mechanics Analysis for Delamination Growth During Impact on Composite Plates," *1989 Advances in Aerospace Structures, Materials, and Dynamics*, American Society of Mechanical Engineers, (1983), pp. 133-138.
- [39] Grady, J. E., and C.T. Sun, "Dynamic Delamination Crack Propagation in a Graphite/Epoxy Laminate," *Composite Materials: Fatigue and Fracture*, ASTM STP 864, (H.T. Hahn, ed.) American Society for Testing and Materials, Philadelphia, PA, (1986), pp. 5-31.
- [40] Kutlu, Z. and F.K. Chang, "Modeling Compression Failure of Laminated Composites Containing Multiple Through-the-Width Delaminations," *J. of Composite Materials*, (to appear in February 1992 issue).
- [41] Chang, F.K., and Z. Kutlu, "Collapse Analysis of Composite Panels Containing Multiple Delaminations," the AIAA/ASME/ASCE/AHS 30th Structures, Structural Dynamics and Materials Conference, April, (1989), Mobile, AL.
- [42] Kutlu, Z., "Compression Response of Laminated Composite Panels Containing Multiple Delaminations," Ph.D. thesis, Department of Mechanical Engineering, Stanford University, (1991).
- [43] Maikuma, H., J.W. Gillespie, Jr., and J.M. Whitney, "Analysis and Experimental Characterization of the Center Notch Flexural Test Specimen for Mode

- II Interlaminar Fracture," *J. of Composite Materials*, Vol. 23, August, (1989), pp. 756-786.
- [44] Chang, F.K. and G.S. Springer, "The Strengths of Fiber Reinforced Composite Bends," *J. of Composite Materials*, Vol. 20, No. 1, January, (1986), pp. 30-45.
- [45] Williams, J.G., "On the Calculations of Energy Release Rates for Cracked Laminates," *International J. of Fracture*, Vol. 36, (1988), pp. 101-119.
- [46] Sun, C.T., and M.G. Manoharan, "Growth of Delamination Cracks Due to Bending in a $[90_5/0_5/90_5]$ Laminate," *Composite Science and Technology*, Vol. 34, (1989), pp. 365-377.
- [47] Martin, R.H., and W.C. Jackson, "Damage Prediction in Cross-Ply Curved Composite laminates," NASA Technical Memorandum 104089, July (1991).
- [48] Salpekar, S.A., "Analysis of Delamination in Cross Ply Laminates Initiating From Impact Induced Matrix Cracking," NASA Contract Report 187594, November (1991).
- [49] Liu, S., Z. Kutlu, and F.K. Chang, "Matrix Cracking and Delamination in Laminated Polymeric Composites Resulting from Transversely Concentrated Loadings," *Proceedings of the 1st International Conferences on Deformation and Fracture of Composites*, , Manchester, England, March 25-27 (1991), pp. 30/1-30/7.
- [50] Liu, S., Z. Kutlu, and F.K. Chang, "Matrix Cracking-Induced Stable and Unstable Delamination Propagation in Graphite/Epoxy Laminated Composites due to Quasi-Static Transverse Concentrated Load," *Composite Materials: Fatigue and Fracture (4th Symposium)*, (1991).
- [51] Liu, S., Z. Kutlu, and F.K. Chang, "Matrix Cracking and Delamination Propagation in Laminated Composites Subjected to Transversely Concentrated Loading," *Journal of Composite Materials*, , (submitted) (1991).

- [52] Rybicki, E.F., and M.F. Konninen, "A Finite Element Calculation of Stress Intensity Factors by a Modified Crack Closure Integral," *Engineering Fracture Mechanics*, Vol. 9, (1977), pp. 931-938.
- [53] Hahn, H.T., "A Mixed-Mode Fracture Criterion for Composite Materials," *Composite Technology Review*, 5, (1983), pp. 26-29.
- [54] Grag, A.C., "Delamination: A Damage Mode in Composite Structures," *Engineering Fracture Mechanics*, Vol. 29, No. 5, (1988), pp. 557-584.
- [55] Lu, X. and D. Liu, "Strain Energy Release Rates at Delamination Front," Proceedings of the American Society of Composites, Fourth Technical Conference, Oct., (1989), pp. 277-286.
- [56] Luenberger, D.G., "Linear and Nonlinear Programming," Addison-Wesley, Reading, Massachusetts, (1984).
- [57] Hestenes, M.R., "Multiplier and Gradient Methods," *Journal of Optimization, Theory and Applications*, Vol. 4, (1969), pp. 303-320.
- [58] Powell, M.J.D., "A Method for Nonlinear Constraints in Minimization Problems," in *Optimization*, R. Fletcher, editor, Academic Press, New York.
- [59] Rockafellar, R.T., "Augmented Lagrange Multiplier Functions and Duality in Nonconvex Programming," *SIAM Journal of Control*, Vol. 12, (1969), pp. 268-285.
- [60] Glowinsky, R., and P. LeTallec, "Finite Element Analysis in Nonlinear Incompressible Elasticity," in *Finite Elements, Vol. V: Special Problems in Solid Mechanics*, J.T. Oden & G.F. Carey eds., Prentice-Hall, Englewood Cliffs, N.J., (1984).
- [61] Wriggers, P. and J.C. Simo, "A Note on Tangent Stiffness for Fully Nonlinear Contact Problems," *Communications in Applied Numerical Methods*, Vol. 1, (1985), 199-203.

- [62] Kikuchi, N. and J.T. Oden, Contact Problems in Elasticity: A Study of Variational Inequalities and Finite Element Methods," SIAM, Philadelphia, (1988).
- [63] Bathe, K.J. and A. Chaudhary, "A Solution Method for Planar and Axisymmetric Contact Problems," *International J. for Numerical Methods in Engineering*, 21, (1985), pp. 65-88.
- [64] Benson, D.J. and J.O. Hallquist, "A Single Surface Contact Algorithm for the Post-buckling Analysis of Shell Structures," *Computer Methods in Applied Mechanics and Engineering*, 78, (1990), pp. 141-163.
- [65] Parisch, H., "A Consistent Tangent Stiffness Matrix for Three-dimensional Non-linear Contact Analysis," *International J. for Numerical Methods in Engineering*, 28, (1989), pp. 803-1812.
- [66] Simo, J.C. and T.A. Laursen, "An Augmented Lagrangian Treatment of Contact Problems Involving Friction," *Computers and Structures*, Vol.42, No.1, (1992), pp. 97-116.
- [67] Chai, H., "Mixed-Mode Fracture Behavior of Delaminated Films," Proceedings of the American Society for Composites, Fourth Technical Conference, Oct., (1989), pp. 815-825.
- [68] Whitcomb, J.D., "Instability-Related Delamination Growth of Embedded and Edge Delaminations," NASA Technical Memorandum 100655, August (1988).
- [69] 69
- [70] Fung, Y.C., *Foundations of Solid Mechanics*, Prentice-Hall, Inc., New Jersey, 1965.
- [71] Bathe, K.J., *Finite Element Procedures in Engineering Analysis*, Prentice-Hall, Inc., New Jersey, (1982).
- [72] Gurtin, M.E., *An Introduction to Continuum Mechanics*, Academic Press, Inc., New York, (1981).

- [73] Atkin, R.J., and N. Fox, *An Introduction to the Theory of Elasticity*, Longman Group Limited, (1980).
- [74] Marsden, J.E., and T.J.R. Hughes, *Mathematical Foundations of Elasticity*, Academic Press, Inc., New York, (1981).
- [75] Kanninen, M.F., and c.H. Popelar, *Advanced Fracture Mechanics*, Oxford Engineering Science Series, Oxford University Press, (1985).
- [76] Ramkumar, R.L., and J.D. Whitcomb, "Characterization of Mode I and Mixed Mode Delamination Growth in T300/5208 Graphite/Epoxy," *Delamination and Debonding of Materials, ASTM STP 876*, W.S. Johnson, Ed., American Society for Testing and Materials, Philadelphia, (1985), pp. 315-335.
- [77] Johnson, W.S., and P.D. Mangalgiri, "Influence of the Resin on Interlaminar Mixed-Mode Fracture," *Toughened Composites, ASTM STP 997*, N.J. Johnston, Ed., American Society for Testing and Materials, Philadelphia, (1987), pp. 295-315.
- [78] Jones, R., J. Paul, T.E. Tay, and J.F. Williams, "Assessment of the Effect of Impact Damage in Composites: Some Problems and Answers," *Theoretical and Applied Fracture Mechanics*, Vol. 9, (1988), pp. 83-95.
- [79] Timoshenko, S.P., and J.N. Goodier, *Theory of Elasticity*, McGraw-Hill, (1934).
- [80] Timoshenko, S.P., and S. Woinowski-Krieger, *Theory of Plates and Shells*, McGraw-Hill, (1959).
- [81] Davidson, B.D., "An Analytical Investigation of Delamination Front Curvature in Double Cantilever Beam Specimens," *Journal of Composite Materials*, Vol. 24, (1990), pp. 1124-1137.
- [82] Crews, J.H., K.N. Shivakumar, and I.S. Raju, "Strain Energy Release Rate Distribution for Double Cantilever Beam Specimen," *AIAA-Journal*, Vol. 10, (1991), pp. 1686-1691.

- [83] Nilsson, K.F., "On Combined Buckling and Interface Crack Growth," Ph.D. Thesis, Department of Solid Mechanics, Royal Institute of Technology, Sweden, Stockholm, (1992).
- [84] Odagiri, N., Kishi, H., and Nakae, T., "T800H/3900-2 Toughened Epoxy Prepreg System: Toughening Concepts and Mechanism," *34th International SAMPE Symposium*, (1989), pp. 43-52.
- [85] Lekhnitskii, S.G., *Theory of Elasticity of an Anisotropic Body*, Mir Publishers, Moscow, (1981).
- [86] Vinson, J.R., *The Behavior of Structures Composed of Composite Materials*, Martinus Nijhoff Publishers, Netherlands, (1986).
- [87] Jones, R.M., *Mechanics of Composite Materials*, McGraw-Hill, New York, (1975).
- [88] Tsai, S.W., and Hahn, H.T., *Introduction to Composite Materials*, Technomic Publishing, (1975).
- [89] Tsai, S.W., *Composites Design*, Think Composites, (1987).